

Investigations of $\text{Al}_{1-x}\text{Ga}_x\text{FeO}_3$ family of oxides

A thesis submitted in partial fulfillment

for the degree of

Master of Science

as a part of the

Integrated Ph. D. programme

(Materials Science)

by

Rana Saha



Chemistry and Physics of Materials Unit
Jawaharlal Nehru Centre for Advanced Scientific Research
(*A Deemed University*)
Bangalore, India.
March 2011

Dedicated to my parents

DECLARATION

I hereby declare that the matter embodied in this M.S. thesis entitled “**Investigations of $\text{Al}_{1-x}\text{Ga}_x\text{FeO}_3$ family of oxides**” is the result of investigations carried out by me under the supervision of Prof. C. N. R. Rao, FRS and Prof. A. Sundaresan at the Chemistry and Physics of Materials Unit, Jawaharlal Nehru Centre for Advanced Scientific Research, Bangalore, India and that it has not been submitted elsewhere for the award of any degree or diploma.

In keeping with the general practice in reporting scientific observations, due acknowledgement has been made whenever the work described is based on the findings of other investigators.

Bangalore
31/03/2011


Rana Saha

CERTIFICATE

We hereby certify that the matter embodied in this M.S. thesis entitled “**Investigations of $\text{Al}_{1-x}\text{Ga}_x\text{FeO}_3$ family of oxides**” has been carried out by Mr. Rana Saha at the Chemistry and Physics of Materials Unit, Jawaharlal Nehru Centre for Advanced Scientific Research, Bangalore, India under our supervision and it has not been submitted elsewhere for the award of any degree or diploma.

Bangalore
31/03/2011



Prof. C. N. R. Rao & Prof. A. Sundaresan
(Research Supervisors)

Acknowledgements

I am extremely thankful to Prof. C. N. R. Rao, FRS and I take this opportunity to express my immense gratitude to him. He not only introduced me to the field of Material Science but also has helped me with his invaluable guidance and fascinating constant encouragement. He is a person of immense enthusiasm and wisdom. It is a rich and fulfilling experience to work under his guidance. He has taught me the various facts of science, the way of understanding the problem and how to maintain levelheaded approach when problems do not work.

My sincere thanks to Prof. A. Sundaresan for having useful scientific discussions and helping me in various ways. His friendly attitude made him a very approachable person for any kind of problem. It has been a great pleasure for me to work under his guidance. He has taught me about time management which is one of the most important and crucial part of our life and that made me successful in my research.

I thank Dr. A. Govindaraj for helping me in getting many chemicals.

I would like thank to my collaborators, Prof. U. V. Waghmare and Ms. Sharmila N. Shirodkar of Theoretical Science Unit, JNCASR and Dr. S. M. Yusuf and Mr. A. K. Bera of Solid State Physics Division, BARC.

I would like to thank, specially Ms. Ajmala Shireen, Dr. Y. Sundarayya and Dr. Nandakumar Kalarikkal for working with me in different research problems.

I would like to thank Mr. Nitesh Kumar and Mr. Pranab Mandal for helping me in magnetic and dielectric measurement in various ways.

I would like to thank all my lab mates, Nitesh, Pranab, Kalyan, Ajmala, Bharat, Shipra, Urmimala, Anupama, Sandeep, Krishna, Moses, Leela, Neenu, Gopal, Barun, Dr. Y.

Sundarayya, Dr. V. P. Bhat, Dr. C. R. Serrao, Dr. Prashant Kumar for helping in various occasions.

Also my heartfelt thanks to my all Int. Ph. D. batch mates of 2008, Varun, Pandeewar, Dileep, Sharma, Chidambar, Arpan, Gayatri and Sudeshna and all the seniors for helping me in all ways possible.

I would like to thank the past and present Int. Ph. D. conveners, Prof. S. Balasubramanian and Dr. T. K. Maji.

I am thankful to the present chairman of our department Prof. G. U. Kulkarni for providing and maintaining various facilities to all the students.

I am grateful to the administration of JNCASR.

I would like to express my gratitude to the various faculty members of the Chemistry and Physics of Materials Unit for the courses they offered and the wonderful classes.

My sincere thanks to the technical staffs of JNCASR for their help with the various characterization techniques.

I express my deep gratitude to all the Professors of Chemistry Department of Ramakrishna Mission Vivekananda Centenary College, Rahara, 24 parganas (N), West Bengal, for their guidance and encouragements towards research.

My deepest thanks to Mrs. Indumati Rao and Mr. Sanjay Rao for their love, affection and hospitality extended to all of us during the course of my association with them.

I thank all my friends from the core my heart, specially Barun, Partha, Sabyasachi, Debabrata, Sudip, Prakash, Prakash Parida, Sudipta, Pralok, Bivas, Saumik, Ritesh, Pawan, Amritroop, Anindita, Dibyajyoti, Darshana, Prashant, Rajdeep, Ram, Kaushik,

Chandan, Chandan Kumar, Sisir, Anirban, Ankush, Parikshit (IISc), Soumalya (School).

Above all, I would like to thank my parents for all the love, affection and support they gave. They stood by me whenever I felt depressed and led me to find out the correct way.

PREFACE

This M.S. thesis presents the results of investigations of the synthesis, structure and physical properties of multiferroic $\text{Al}_{1-x}\text{Ga}_x\text{FeO}_3$ family of oxides. Multiferroics are materials in which two or all three of ferroelectricity, ferromagnetism and ferroelasticity occur in the same phase. Such materials have the potential applications of their parent materials, as well as new ones because of the interaction between the order parameters. The thesis consists of three parts.

Part 1 gives an overview of multiferroics, explaining the origin of multiferroicity, occurrence of magnetoelectric coupling, their possible technological applications and the challenges involved.

Part 2 gives the results of detailed investigations of magnetic and dielectric properties of $\text{Al}_{1-x}\text{Ga}_x\text{FeO}_3$ family of oxides along with structural aspects by employing X-ray and neutron diffraction, Mössbauer spectroscopy and other techniques.

Part 3 gives the experimental results of structural phase transitions of $\text{Al}_{1-x}\text{Ga}_x\text{FeO}_3$ ($x = 0, 1$) family of oxides, examined by X-ray diffraction, Raman Spectroscopy and Magnetic measurement.

Contents

<i>Declaration</i>	III
<i>Certificate</i>	V
<i>Acknowledgements</i>	VII
<i>Preface</i>	XI
<i>Contents</i>	XIII

Part 1.

<i>Multiferroics: A Brief Overview</i>	<i>1</i>
1.1 <i>Introduction</i>	<i>1</i>
1.2 <i>Ferromagnets (and other magnetic materials)</i>	<i>2</i>
1.3 <i>Ferroelectrics</i>	<i>6</i>
1.3.1 <i>Symmetry</i>	<i>7</i>
1.3.2 <i>Origin of ferroelectricity in perovskite oxides</i>	<i>8</i>
1.4 <i>Multiferroics</i>	<i>11</i>
1.4.1 <i>Symmetry</i>	<i>14</i>
1.4.2 <i>Types of Multiferroics</i>	<i>14</i>
<i>Bismuth-based compounds: Lone Pair effect</i>	<i>15</i>
<i>Hexagonal manganites: Geometric frustration</i>	<i>18</i>
<i>Magnetic ferroelectricity due to charge ordering</i>	<i>21</i>
<i>Ferroelectricity due to magnetic ordering</i>	<i>25</i>
1.5 <i>Magnetoelectric effect</i>	<i>31</i>
<i>Nonlinear Coupling</i>	<i>34</i>
<i>Indirect Coupling</i>	<i>35</i>

<i>References.....</i>	<i>36</i>
Part 2.	
<i>Investigations of $Al_{1-x}Ga_xFeO_3$ family of oxides: magnetic and dielectric properties.....</i>	<i>43</i>
<i>Summary.....</i>	<i>43</i>
2.1 <i>Introduction.....</i>	<i>44</i>
2.2 <i>Scope of the present investigations.....</i>	<i>45</i>
2.3 <i>Experimental.....</i>	<i>45</i>
<i>Synthesis.....</i>	<i>45</i>
<i>Characterization.....</i>	<i>46</i>
<i>Measurement of properties.....</i>	<i>46</i>
2.4 <i>Results and Discussion.....</i>	<i>47</i>
2.4.1 <i>Structure.....</i>	<i>47</i>
<i>X-Ray Diffraction results of $AlFeO_3$ and $GaFeO_3$.....</i>	<i>47</i>
<i>Neutron Diffraction results of $AlFeO_3$.....</i>	<i>50</i>
<i>Neutron Diffraction results of $GaFeO_3$.....</i>	<i>61</i>
2.4.2 <i>Magnetic properties of $AlFeO_3$ and $GaFeO_3$.....</i>	<i>75</i>
2.4.3 <i>Electrical and magnetoresistance properties of $AlFeO_3$ and $GaFeO_3$.....</i>	<i>83</i>
2.4.4 <i>Dielectric and magnetodielectric properties of $AlFeO_3$ and $GaFeO_3$.....</i>	<i>84</i>
2.4.5 <i>Effect of Cr substitution on magnetic properties of $GaFeO_3$.....</i>	<i>87</i>
2.5 <i>Conclusions.....</i>	<i>93</i>
<i>References.....</i>	<i>95</i>

Part 3.

***Phase transformations of AlFeO_3 and GaFeO_3 induced by ball-milling*.....103**

Summary.....103

3.1 Introduction.....103

3.2 Results and Discussion.....104

3.2.1 GaFeO_3104

3.2.2 AlFeO_3 111

3.3 Conclusions.....116

References.....116

Multiferroics: A Brief Overview

1.1 Introduction:

Ferromagnets, ferroelectrics, and ferroelastics all together come under a generic name ‘Ferroics’. Studies on ferroics mainly focuses on the change of different physical properties such as magnetic, dielectric and other related properties due to a change of external stimuli like temperature, magnetic field, electric field etc. Often the changes of physical properties are associated with structural phase transition at some critical temperature. This phase transitions result in only small deviations from the nonferroic crystal structure and also alters the point symmetry of the material. This breaking of symmetry is physically what allows the formation of the ferroic phase. Ferroelectric materials possess a spontaneous polarization that is stable and can be switched hysteretically by an applied electric field where as ferromagnetic materials possess a spontaneous magnetization that is stable and can be switched hysteretically by an applied magnetic field and ferroelastic materials display a spontaneous deformation that is stable and can be switched hysteretically by an applied stress. In recent years a new class of novel ferroic materials, called multiferroics which exhibit more than a single ferroic property simultaneously in a single phase has drawn considerable attention of the researcher. This chapter deals with main aspects of ferromagnets, ferroelectrics and multiferroics.

1.2 Ferromagnets: (and other magnetic materials)

The magnetic effects, except diamagnetism, observed in inorganic materials are due to the presence of unpaired electrons. Thus magnetism is mainly observed in compounds having transition metals and lanthanides due to the presence of unpaired d and f electrons respectively. Magnetism can arise from either the orbital component of the angular momentum, or the spin component (if there are unequal numbers of up and down spin electrons) or both. The random orientations of unpaired electrons on the different atoms lead the material to be paramagnetic. Parallel alignment of these unpaired electrons makes the material as ferromagnetic. If they align in antiparallel, then the material becomes antiferromagnetic. In case of unequal magnetic moment of the spins in antiparallel alignment will lead to ferrimagnetic behaviour. However among the different magnetic behaviours, materials having ferromagnetism are widely used in application.

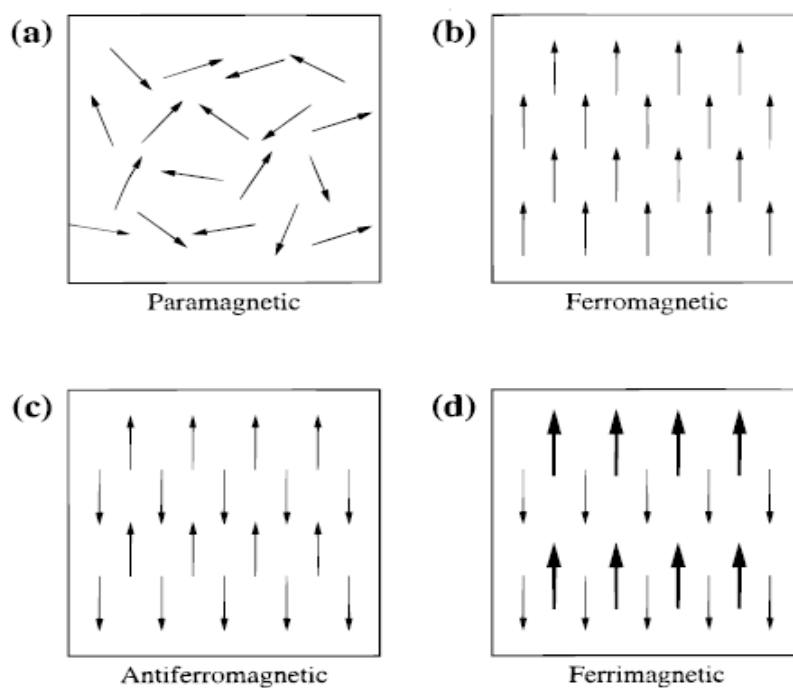


Fig. 1.1: Ordering of the magnetic dipoles in magnetic materials.

Ferromagnetic materials have domains in their structure. In each domain all the spins are aligned parallel and different domains have different spin orientations. At sufficiently high field, all the domains have parallel spin orientated along the magnetic field and the direction can be switched by switching the field in opposite direction. Thus by varying the magnetic field, ferromagnetic materials will show a hysteresis loop. Materials with low coercivity, the magnitude of the reversal field required to achieve demagnetization, are referred as soft magnets. While the materials with high coercivity, are termed as hard magnets.

Indeed there is a strong driving force for electrons to align their spins parallel (creating unequal numbers of up and down spin electrons); this is the quantum-mechanical exchange energy. One can develop an intuition for why exchange coupling is such a strong driving force using simple electrostatic arguments: If two electrons in an atom have antiparallel spins, then they are allowed to share the same atomic or molecular orbital. As a result they will overlap spatially, thus increasing the electrostatic Coulomb repulsion. On the other hand, if they have parallel spins, then they must occupy different orbitals and so will have less unfavourable Coulomb repulsion. So the orientation of the spins affects the spatial part of the wave function, and this in turn determines the electrostatic Coulomb interaction between the electrons.

There are two phenomenological theories of ferromagnetism that have been successful in explaining many of the properties of ferromagnets, the localized moment theory of Curie and Weiss [1], which arose from the study of magnetic insulators, and the Stoner band theory of ferromagnetism in metals [2]. In the localized moment theory, an internal “molecular field” acts in ferromagnetic materials to align the magnetic moments parallel to each other. The origin of this molecular field is quantum mechanical exchange energy, which causes electrons with parallel spins (and therefore parallel magnetic moments) to have a lower energy than electrons

with antiparallel spins, all other factors being equal. Below the Curie temperature, T_c , the molecular field is so strong that it magnetizes the substance even in the absence of an external applied field. At high enough temperatures, the thermal energy, kT , is larger than the alignment energy of the molecular field, resulting in the random orientation of the magnetic moments and paramagnetic behavior. Such behavior is analogous to the order-disorder description of ferroelectrics, in which the constituent ions are always off-centered, but only below the Curie temperature do the directions of off-centering align cooperatively to give a net electric polarization. In the Stoner band theory, there are equal numbers of up and down spin electrons above the Curie temperature, and hence no magnetic moment. Below T_c the up and down spin bands are unequally populated by electrons, leading to a net magnetic moment. Here, the analogy is to the displacive model of ferroelectricity, in which the Curie temperature is coincident with off-centering of the ions.

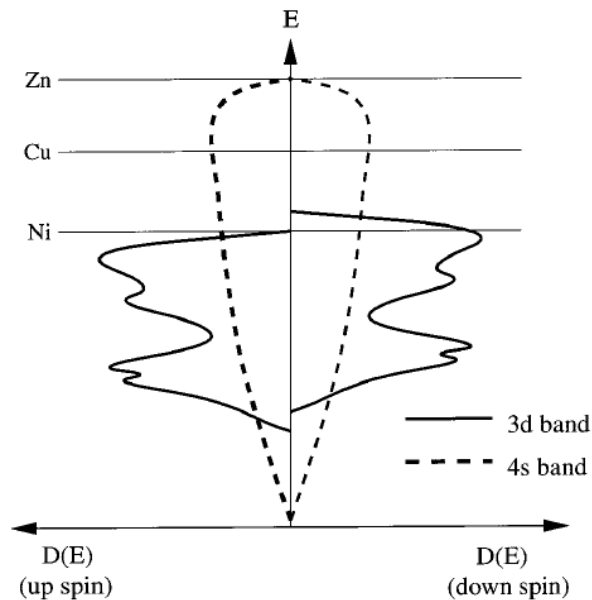


Fig. 1.2: 3d and 4s up and down spin densities of states in first-row transition metals, with exchange interaction included.

From Fig.1.2 it is clear why the later transition metals, Cu and Zn, are not ferromagnetic. In Cu, the Fermi level lies above the $3d$ bands. Because two of the $3d$ bands are filled and the $4s$ band has no exchange splitting, the numbers of up- and down- spin electrons are equal. In Zn, both the $3d$ and $4s$ bands are filled and so do not contribute a magnetic moment.

Most of the ferromagnetic materials known are metallic and there are considerable numbers of insulating ferromagnetic compounds. The ferromagnetism observed in those insulating compounds is explained on the basis of superexchange interaction. Even though superexchange interaction has been explained earlier, a considerably more satisfactory system of semi-empirical rules was developed over a period of years by Goodenough [3] and Kanamori [4]. These rules have the important features of the occupation of various d levels as dictated by ligand field theory. They are related to the prescriptions of Anderson's work about the sign of superexchange [5]. The exchange interaction in magnetic insulators is predominantly caused by the so-called superexchange which is due to the overlap of the localized orbitals of the magnetic electrons with those of intermediate ligands. The main features of the superexchange interactions are usually explained in terms of the so-called Goodenough- Kanamori-Anderson rules [4, 6, 7]. According to these rules, a 180° superexchange (the magnetic ion-ligand-magnetic ion angle is 180°) of two magnetic ions with partially filled d shells is strongly antiferromagnetic, whereas a 90° superexchange interaction is ferromagnetic and much weaker.

1.3 Ferroelectrics:

A ferroelectric material is defined as one which undergoes a phase transition from a high-temperature phase that behaves as an ordinary dielectric (so that an applied electric field induces an electric polarization, which goes to zero when the field is removed) to a low-temperature phase that has a spontaneous polarization whose direction can be switched by an applied field. Many properties of ferroelectric materials are analogous to those of ferromagnets, but with the electric polarization, \mathbf{P} , corresponding to the magnetization, \mathbf{M} ; the electric field, \mathbf{E} , corresponding to the magnetic field, \mathbf{H} ; and the electric displacement, \mathbf{D} , corresponding to the magnetic flux density, \mathbf{B} .

In 1921, Valasek first observed the phenomena, ferroelectricity, in the Rochelle salt ($\text{KNaC}_4\text{H}_4\text{O}_6 \cdot 4\text{H}_2\text{O}$). However, it took many years to unveil its importance in technological applications, especially in memory devices [8]. A colossal increase in the research on ferroelectric materials came in 1950s, leading to the widespread use of barium titanate (BaTiO_3) based ceramics in capacitor applications and piezoelectric transducer devices. Since then, many other ferroelectric materials including lead titanate (PbTiO_3), lead zirconate titanate ($\text{PbZr}_{1-x}\text{Ti}_x\text{O}_3$), lead lanthanum zirconate titanate ($\text{Pb}_{1-x}\text{La}_x\text{Zr}_{1-y}\text{Ti}_y\text{O}_3$), and relaxor ferroelectrics like lead magnesium niobate ($\text{PbMg}_{1-x}\text{Nb}_x\text{O}_3$) have been developed and utilized for several applications. Later many new applications have emerged with the development of ceramic processing and thin film technology. Ferroelectrics are key materials in microelectronics. Their excellent dielectric properties make them viable candidate for electronic components such as tunable capacitors, non-volatile memories, piezoelectric materials for medical ultrasound imaging and actuators, and electro-optic materials for data storage and displays.

1.3.1 Symmetry:

A primary requirement for the existence of ferroelectricity is a structural distortion from the prototypical high-symmetry phase that removes the center of symmetry and allows an electric polarization. Thus the symmetry plays a key role in these materials. In other words, the ferroelectric crystals are characterized by having polarization vectors that can be oriented in two diametrically opposite directions by applying an external electric field.

The symmetry of the crystals is governed by their lattice structure. Though there are thousands of crystals in nature, they all can be grouped together into 230 space groups based on the symmetry elements. The space groups in three dimensions are made from combinations of 32 crystallographic point groups with 14 Bravais lattices which belong to one of 7 crystal systems. The 32 point groups can be further classified into (a) crystals having centre of symmetry and (b) crystals which do not possess center of symmetry. Crystals with center of symmetry include 11 point groups are labeled as centrosymmetric and they do not show polarity. The remaining 21 point groups do not have center of symmetry (i.e. non-centrosymmetric). All non-centrosymmetric point groups, except the point group 432, show piezoelectric effect along the unique directional axes. A crystal having no center of symmetry possesses one or more crystallographically unique directional axes. Space groups lacking an inversion center (non-centrosymmetric) are further divided into polar and chiral types. A chiral space group is one without any rotoinversion symmetry elements. Rotoinversion (also called an 'inversion axis') is rotation followed by inversion; for example, a mirror reflection corresponds to a two-fold rotoinversion. Chiral space groups must therefore only contain (purely) rotational and translational symmetry. These arise from the crystal point groups 1, 2, 3, 4, 6, 222, 422, 622, 32, 23, and 432. Chiral molecules such as proteins crystallize in chiral space groups. The term

‘polar’ is often used for those space groups which are neither centrosymmetric nor chiral. However the term ‘polar’ is more correctly used for any space group containing a unique anisotropic axis. These occur in point groups 1, 2, 3, 4, 6, m , $mm2$, $3m$, $4mm$, and $6mm$. Thus some chiral space groups are also polar. Out of the twenty point groups which show the piezoelectric effect, the ten polar point groups have only one unique direction axis and such crystals show spontaneous polarization.

Thus considering symmetry restrictions, all ferroelectric materials are pyroelectric, however not all pyroelectric materials are ferroelectric. Since all pyroelectric materials are piezoelectric, this means ferroelectric materials are inherently piezoelectric.

1.3.2 Origin of ferroelectricity in perovskite oxides:

Let us consider the ferroelectricity in two related perovskite-structure compounds, PbTiO_3 and BaTiO_3 . Both materials have the cubic structure at high temperatures. PbTiO_3 undergoes a phase transition to a tetragonal phase below 766 K, with the polarization along the [100] direction. BaTiO_3 undergoes a series of phase transitions from cubic to tetragonal to orthorhombic to rhombohedral, with the low-temperature polarization along the [111] direction. Based on the theoretical calculations, Cohen *et al.*, have suggested that in both cases, the Ti $3d$ -O $2p$ hybridization is essential for stabilizing the ferroelectric distortion [9]. So it seems that if we have an empty d level, only the bonding bands would be occupied (solid arrows in Fig.1.3b), there by gaining the electronic energy. If however we have e.g. one d -electron on the corresponding d -orbital (dashed arrow in Fig.1.3b), this electron will occupy an antibonding hybridized state, and the total energy gain will be reduced. In BaTiO_3 , Ba $5p$ does not hybridize with the valence band and the Ba-O interaction is largely ionic in nature. In PbTiO_3 , there is

hybridization between the Pb 6s and O 2p electrons. This results in a large Pb polarizability and a strain that stabilizes the tetragonal phase over the rhombohedral phase in PbTiO_3 .

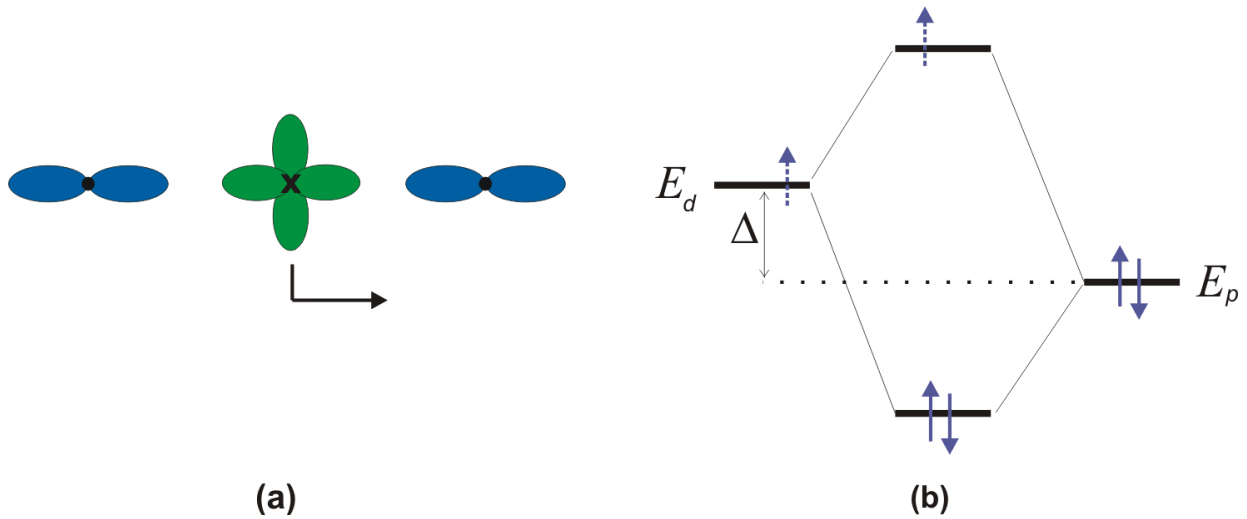


Fig. 1.3: (a) Shifts of transition metal ion toward one of the oxygens and (b) schematic energy levels with empty d-level (solid arrows) and with partially filled d-level (dashed arrow).

In the proper ferroelectrics discussed so far, structural instability towards the polar state, associated with the electronic pairing, is the main driving force of the transition. If, on the other hand, polarization is only a part of a more complex lattice distortion or if it appears as an accidental by-product of some other ordering, the ferroelectricity is called improper [10]. For example, the hexagonal manganites RMnO_3 ($R = \text{Ho-Lu, Y}$) show a lattice transition which enlarges their unit cell. An electric dipole moment, appearing below this transition, is induced by a nonlinear coupling to nonpolar lattice distortions, such as the buckling of R-O planes and tilts of manganese oxygen bipyramids (geometric ferroelectricity) [11,12].

Based on different origin of ferroelectricity, they are classified into two different category such as proper and improper ferroelectrics as shown in the following Table I.

Table I**Classification of ferroelectrics**

	Mechanism of inversion symmetry breaking	Materials
Proper	Covalent bonding between $3d^0$ transition metal (Ti) and oxygen.	BaTiO ₃ .
	Polarization of $6s^2$ lone pair of Bi or Pb	BiMnO ₃ , BiFeO ₃ , Pb(Fe _{2/3} W _{1/3})O ₃ , PbTiO ₃ .
Improper	Structural transition 'Geometric ferroelectrics'	K ₂ SeO ₄ , Cs ₂ CdI ₄ hexagonal RMnO ₃ .
	Charge ordering 'Electronic ferroelectrics'	LuFe ₂ O ₄ .
	Magnetic ordering 'Magnetic ferroelectrics'	Orthorhombic RMnO ₃ , RMn ₂ O ₅ , CoCr ₂ O ₄ .

1.4 Multiferroics:

Materials which exhibit both magnetic and electrical ordering have attracted great interest because of their technological potential. Besides a range of possible device applications, the science of these materials is truly fascinating. Materials in which two or all three of the ferroic properties — such as ferromagnetism, ferroelectricity and ferroelasticity are combined in the same phase, have been coined as “multiferroics” by H. Schmid in 1994 [13]. This implies that they possess spontaneous magnetic polarization that can be reversed by a magnetic field, a spontaneous electric polarization that can be switched by an applied electric field and a change in their electric polarization accompanied by a change in shape which can be reoriented by an applied stress. It is, however, customary to exclude ferroelasticity and only consider magnetic and ferroelectric characteristics. However the definition of multiferroics has been expanded to include also non-primary order parameters, such as antiferromagnetism or ferrimagnetism.

It is generally difficult to find materials that are magnetic as well as ferroelectric. Most ferroelectrics are transition metal oxides, in which transition ions have empty d shells. These positively charged ions like to form molecules with one (or several) of the neighboring negative oxygen ions. This collective shift of cations and anions inside a periodic crystal induces bulk electric polarization. The mechanism of the covalent bonding (electronic pairing) in such molecules is the virtual hopping of electrons from the filled oxygen shell to the empty d shell of a transition metal ion. Magnetism, on the contrary, requires transition metal ions with partially filled d shells, as the spins of electrons occupying completely filled shells add to zero and do not participate in magnetic ordering. The exchange interaction between uncompensated spins of different ions, giving rise to long range magnetic ordering, also results from the virtual hopping of electrons between the ions. In this respect the two mechanisms are not so dissimilar, but the

difference in filling of the d shells required for ferroelectricity and magnetism makes these two ordered states mutually exclusive.

Magnetoelectrics are simultaneously ferromagnetic and ferroelectric in the same phase, with coupling between the two orders. Magnetoelectric coupling describes the influence of a magnetic (electric) field on the polarization (magnetization) of a material and vice versa. Magnetoelectric coupling can exist independent of the nature of the magnetic and electrical order parameters. It is an independent phenomenon which may not necessarily arise in materials that are both magnetically and electrically polarizable (See Fig. 1.4, from ref. [14]).

Nickel iodine boracite, $\text{Ni}_3\text{B}_7\text{O}_{13}\text{I}$ was discovered to be the first ferromagnetic ferroelectric material [15]. The search for other ferromagnetic ferroelectrics began in Russia in the 1950s, with the replacement of some of the d^0 B cations in ferroelectric perovskite oxides by magnetic d^n cations [16]. In the early 1960s, using this approach the first synthetic ferromagnetic ferroelectric material, $(1-x)\text{Pb}(\text{Fe}_{2/3}\text{W}_{1/3})\text{O}_3-x\text{Pb}(\text{Mg}_{1/2}\text{W}_{1/2})\text{O}_3$, was produced [17]. Here, the Mg and W ions are diamagnetic and cause the ferroelectricity, and the formally d^5 Fe^{3+} ion is responsible for the magnetic ordering. The ferromagnetic spinel CdCr_2S_4 exhibits relaxor ferroelectricity below 135 K [7]. YMnO_3 is antiferromagnetic below the Néel temperature (T_N) 80 K and ferroelectric below the Curie temperature (T_{CE}) 914 K [8]. In this material, ferroelectricity is associated with the tilting of the MnO_5 trigonal bipyramids. Another oxide with similar properties is BiFeO_3 ($T_N = 670$ K, $T_{\text{CE}} = 1110$ K) [18], where ferroelectricity arises from the stereochemical activity of the Bi lone pair [19]. BiMnO_3 is one of the few materials shown to be simultaneously ferromagnetic and ferroelectric ($T_C = 450$ K, $T_{\text{CE}} = 105$ K) [20]. While BiFeO_3 and BiMnO_3 are proper ferroelectrics, TbMnO_3 , which is an improper ferroelectric, shows interesting features where in spiral magnetic ordering is the source of the

ferroelectricity [21]. One of the new ideas is that charge-ordered and orbital ordered perovskites could exhibit ferroelectric magnetism due to coupling between magnetic and charge ordering [22]. Beside single phase oxide materials, several two-phase systems have been shown to exhibit magnetoelectric coupling [14], typical examples being $\text{BaTiO}_3\text{-CoFe}_2\text{O}_4$, $\text{Tb}_x\text{Dy}_{1-x}\text{Fe}_2\text{-Pb(Zr,Ti)O}_3$ (PZT) and $\text{La}_{0.7}\text{Sr}_{0.3}\text{MnO}_3\text{-PZT}$.

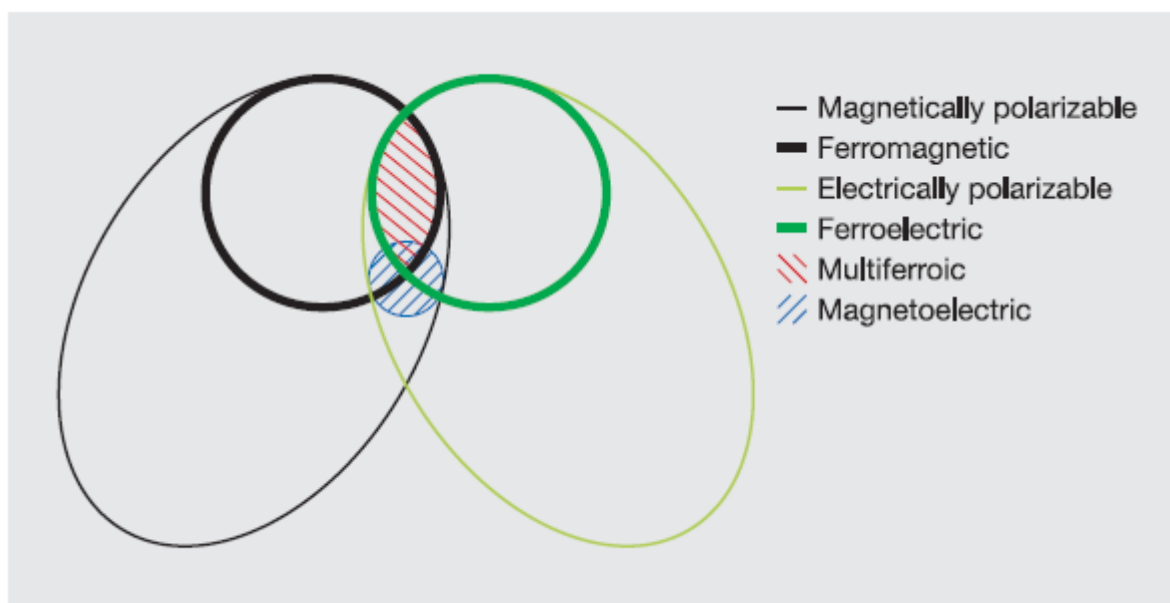


Fig. 1.4: The relationship between multiferroic and magnetoelectric materials. Ferromagnets (ferroelectrics) form a subset of magnetically (electrically) polarizable materials such as paramagnets and antiferromagnets (paraelectrics and antiferroelectrics). The intersection (red hatching) represents materials that are multiferroic. Magnetoelectric coupling (blue hatching) is an independent phenomenon that can, but need not, arise in any of the materials that are both magnetically and electrically polarizable. In practice, it is likely to arise in all such materials, either directly or via strain (from ref. [14]).

1.4.1 Symmetry:

As the crystal symmetry plays a key role in ferroelectric properties, it is clear that multiferroic property is closely linked to symmetry. The primary ferroic properties (Table II) can be characterized by their behaviour under space and time inversion. Space inversion, for example, will reverse the direction of polarization (P), while leaving the magnetization (M) invariant. Time reversal, in turn, will change the sign of M, while the sign of P remains invariant. Magnetoelectric multiferroics require simultaneous violation of space and time inversion symmetry.

Table II: Ferroics - symmetry

Symmetry	Space Invariant	Space Variant
Time Invariant	Ferroelastic	Ferroelectric
Time Variant	Ferromagnetic	Ferrotoroidic

1.4.2 Types of Multiferroics:

Despite this apparently bad compatibility of magnetism and ferroelectricity, there are many systems in which these properties coexist and the mechanism has been classified into four different possible ways to combine magnetism and ferroelectricity typical of them being lone-pair effects, geometric frustration, charge-ordering and magnetic ferroelectricity induced by frustrated magnetism as shown in Table III. Charge-order driven magnetic ferroelectricity is interesting in that it would be expected to occur in a large number of rare earth manganites, $\text{Ln}_{1-x}\text{A}_x\text{MnO}_3$ (Ln = Rare earth, A = alkaline earth), well known for colossal magnetoresistance, electronic phase separation and other properties. Now I shall discuss novel routes to multiferroics, giving specific examples of materials along with their characteristics.

Table III

Mechanisms for Multiferroics

Mechanism	Description	Examples
Lone-pair effects	In perovskites of general formula ABX_3 , lone pairs of electrons on the A cation distort the geometry of the BX_3 anion, resulting in ferroelectricity.	$BiFeO_3$, $BiMnO_3$
Geometric frustration	Long-range dipole–dipole interactions and rotations of oxygen atoms generate a stable ferroelectric state.	$YMnO_3$
Charge ordering	Certain ‘non-centrosymmetric’ arrangements of ions induce ferroelectricity in magnetic materials.	$LuFe_2O_4$
Magnetic ordering	Ferroelectricity is induced by magnetic long-range order in which the arrangement of magnetic dipoles lacks reflection symmetry.	$TbMnO_3$, $DyMnO_3$, $TbMn_2O_4$

(a) Bismuth-based compounds: Lone pair effect

In this section I shall discuss about the origin of ferroelectricity in magnetic $BiFeO_3$ and $BiMnO_3$ although both of these materials contain only magnetic transition metal (TM) ions $Fe^{3+}(d^5)$ and $Mn^{3+}(d^4)$, seems that these two materials violate d^0 requirement for ferroelectricity discussed in the previous section. However the more detailed treatment shows that the main instability leading to FE in these systems is not due to TM ions as e.g. in $BaTiO_3$, but is rather driven by the A-ions, in this case Bi. Properties of the Bismuth compounds are largely determined by the Bi 6s lone pair. The so called lone pairs, two valence electrons of Bi^{3+} (also Pb^{2+}), which could have participated in chemical bonds using (sp)-hybridized states (usually sp^2 or sp^3), but which in these systems do not participate in such bonds. The Bi ion with two electrons on the 6s orbital moves away from the centrosymmetric position in its oxygen

surrounding [19]. From the phenomenological point of view this gives high polarizability of corresponding ions, which in classical theory of FE is believed to lead, or at least strongly enhance, the instability towards FE. From the microscopic point of view we can simply say that the particular orientation of these lone pairs, or dangling bonds, may create local dipoles, which finally can order in a FE or anti-FE fashion. Because the ferroelectric and magnetic orders in these materials are associated with different ions, the coupling between them is weak. BiFeO₃ is an incommensurate antiferromagnet and a commensurate ferroelectric at room temperature [23, 24]. The spins are not collinear and take a long wavelength spiral form and the magnetoelectric effect is, therefore, not linear and occurs in the presence of a large magnetic field [25] or by appropriate chemical substitution [26] and in epitaxial thin films [27]. BiMnO₃ is probably the only single-phase material which is truly biferroic, but the observed polarization is small ($0.12 \mu\text{C}/\text{cm}^2$ at 87 K) [20]. In Fig. 1.5 magnetic and dielectric properties of BiMnO₃ is shown along with the magnetic field induced changes in the dielectric constant [20, 28]. Ferromagnetism in BiMnO₃ is due to orbital ordering [29] and ferroelectric ordering is accompanied by a structural transition [20]. It has been shown recently that BiMnO₃ is centrosymmetric at room temperature with the centrosymmetric space group $C2/c$ [30]. Theoretical calculations also seem to suggest a centrosymmetric structure. It is possible that this material is locally non-centrosymmetric and globally centrosymmetric. BiCrO₃ exhibits a ferroelectric transition at 440 K and parasitic ferromagnetism below 114 K [31]. Bi₂Mn_{4/3}Ni_{2/3}O₆ is a polar oxide showing a magnetic response of a concentrated spin-glass below 35 K [32]. Bi₂MnNiO₆ shows both the ferroelectric and ferromagnetic properties [33]. Interestingly La₂NiMnO₆ which is a ferromagnetic semiconductor is found to exhibit magnetocapacitance and magnetoresistance properties at temperatures upto 280 K [34].

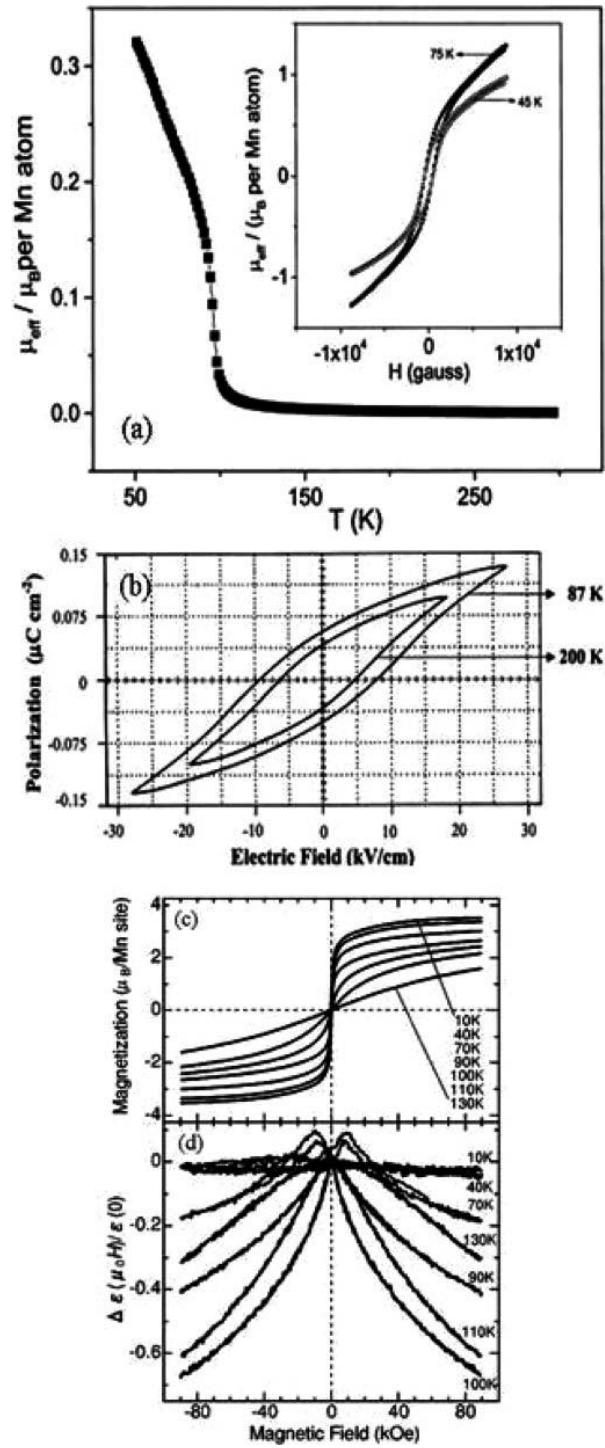


Fig. 1.5: (a) Temperature variation of magnetization of BiMnO₃ at 500 Oe. Inset shows the hysteresis loops at 75 and 45 K, (b) P-E hysteresis loops of polycrystalline BiMnO₃ (from ref. [20]). Isothermal (c) magnetization and (d) field-induced change in dielectric constant as a function of a magnetic field at different temperatures (from ref. [28]).

(b) Hexagonal manganites: Geometric frustration

One important class of compounds which are often cited as violating the “ d^0 -ness” rule, hexagonal manganites RMnO_3 ($\text{R}=\text{Y}$ or small rare earths). In contrast to conventional perovskites and even to quasi-one-dimensional hexagonal perovskites like CsNiCl_3 , in YMnO_3 Mn^{3+} ions are located not in O_6 octahedra, but are in a 5-fold coordination – in the centre of the O_5 trigonal bipyramid. Similarly R-ions, e.g. Y, are not in a 12-fold, but in a 7-fold coordination. Consequently also the crystal field level scheme of Mn ions in these compounds is different from the usual one in an octahedral coordination, instead of a triplet t_{2g} and a doublet e_g , here d -levels are split into two doublets and an upper singlet. Consequently four d -electrons of Mn^{3+} occupy here two lowest-lying doublets and, in contrast to Mn^{3+} in octahedral coordination, there is no orbital degeneracy left, so that in these compounds Mn^{3+} is not a Jahn-Teller ion (this may be relevant for the very existence of this particular crystal structure in these manganites [35]). The materials RMnO_3 are known to be ferroelectric with pretty high transition temperatures ~ 900 - 1000 K and with much lower Néel temperatures as observed in YMnO_3 $T_{\text{FE}} = 950$ K, $T_{\text{N}} = 77$ K. Hexagonal YMnO_3 (space group $P6_3cm$) is an improper ferroelectric [36] and an A-type antiferromagnet with non-collinear Mn spins oriented in a triangular arrangement. Ferroelectricity in YMnO_3 is driven by electrostatic and size effects unlike in other perovskite oxides BaTiO_3 , where the transition is associated with the changes in the chemical bond. Off-centering of the Mn ions is energetically unfavourable in YMnO_3 and ferroelectricity arises from the buckling of the MnO_5 polyhedra, combined with the displacements of Y ions and the layered MnO_5 network [12]. Therefore the main dipole moments are formed not by Mn-O, but by Y-O pairs. But it does not prove that it is Y or other R-ions which are directly responsible for FE. Instead it appears that tilting in the hexagonal structure of YMnO_3 leads to a loss of an inversion

centre and to FE, with dipole moments mostly formed by Y – O pairs. We can say that FE in these compounds is almost an “accidental by-product” [37] of the tendency to close packing. It is not surprising then that also here the corresponding structural phase transitions occurs at pretty high transition temperatures $\sim 900\text{-}1000$ K. Since the mechanisms of magnetic and FE ordering in these systems have quite different nature, so the coupling between magnetic and FE degrees of freedom will be very weak. Coupling between electric and magnetic ordering in YMnO_3 is accompanied by the formation of domains and domain walls as shown in Fig. 1.6.

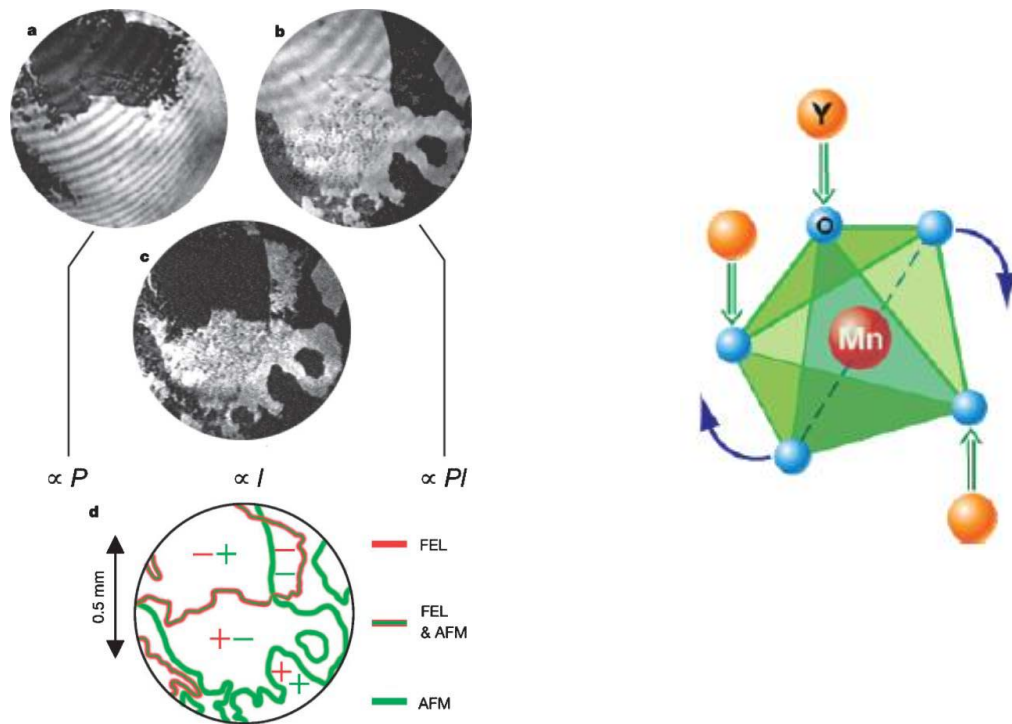


Fig. 1.6: Coexistence of electric and magnetic domains in a YMnO_3 sample at 6 K and Polyhedral tilting. (a) Exposed with second harmonic light from $\chi(P)$, where χ is the non-linear optical susceptibility and P is the ferroelectric order parameter. Dark and bright areas correspond to opposite ferroelectric (FEL) domains. (b) Exposed with ferroelectromagnetic (FEM) second harmonic light from $\chi(Pl)$ where l is the anti-ferromagnetic (AFM) order parameter. Bright and dark regions are distinguished by an opposite sign of the product Pl . (c) Dark and bright areas correspond to opposite AFM domains. (d) Topology of FEL (red) walls and AFM (green) walls in the sample with \pm signs of the corresponding colour indicating the orientation of the FEL and AFM order parameters in selected domains (from ref. [38]).

Domain wall interaction is seen in spatial maps obtained by imaging with optical second harmonic generation [38]. The antiferromagnetic domain walls interact with the lattice strain (ferroelectric walls), coupling between the two being mediated by the piezomagnetic effect [39]. This lowers the total energy of the system and leads to a piezomagnetic clamping of the electric and magnetic order parameters. Neutron diffraction experiments show that the structural parameters of YMnO_3 abruptly change at T_N indicating spin-lattice coupling [40]. Thermal conductivity undergoes a sudden increase upon magnetic ordering and enhances in magnitude below T_N [41].

Just like YMnO_3 , hexagonal HoMnO_3 also exhibits a dielectric anomaly at T_N (75 K) [42]. An electrically driven magnetic phase transition has also been observed in HoMnO_3 . Orthorhombic HoMnO_3 and YMnO_3 show a large increase in the dielectric constant at T_N due to strong magnetoelectric coupling [43]. Hexagonal LuMnO_3 also shows a dependence of the dielectric constant in the T_N region with a weak magnetoelectric coupling. Magnetic exchange coupling in LuMnO_3 is mainly in the a - b plane of the MnO_5 trigonal bipyramids, while the electric dipole moment of LuO_7 is oriented along the hexagonal c axis [44].

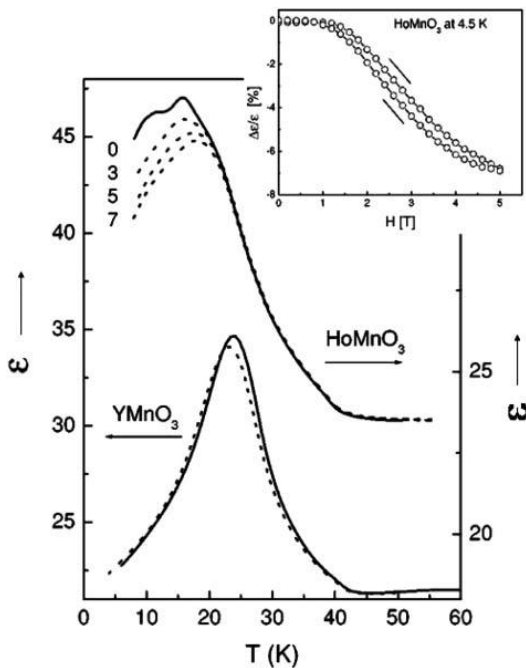


Fig. 1.7: Magnetodielectric effect in YMnO_3 (left scale, full line: $H = 0$; dotted line: $H = 7$ T) and in HoMnO_3 (right scale, full line: $H = 0$; dotted lines: $H = 3, 5, 7$ T from top to bottom). Inset: relative change of the dielectric constant as a function of the magnetic field for HoMnO_3 at 4.5K (from ref. [43]).

(c) Magnetic ferroelectricity due to charge ordering:

One more novel mechanism of ferroelectricity in magnetic materials was pointed out by Khomskii and coworkers [35] and they suggested that coupling between magnetic and charge-ordering in charge-ordered and orbital-ordered perovskites like $\text{Ln}_{1-x}\text{A}_x\text{MnO}_3$, can give rise to magneto-ferroelectricity. The essential mechanism by which charge ordering can lead to the appearance of ferroelectricity is easily explained with the help of the schematic picture shown in Figs. 1.8 and 1.9.

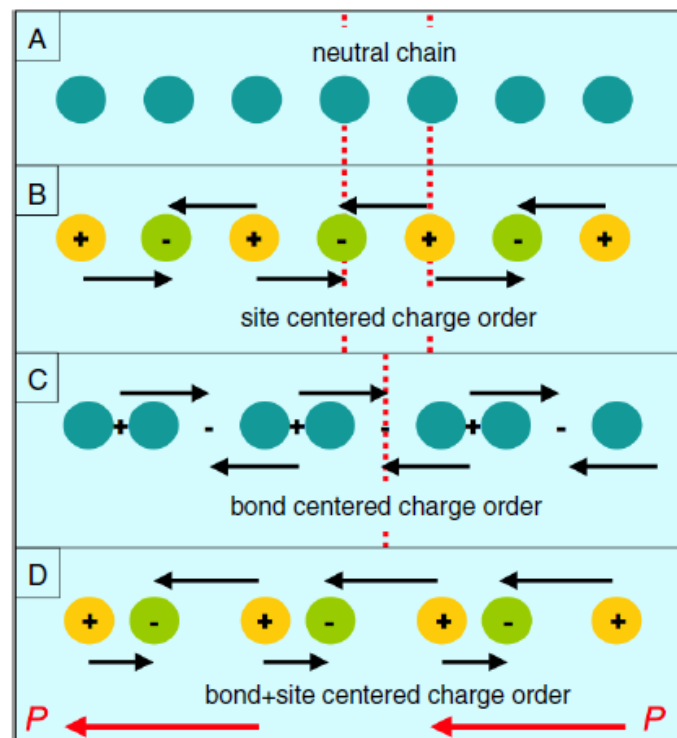


Fig. 1.8: (a) Example of a neutral one-dimensional chain exhibiting (b) site-centered charge ordering, (c) bond-centered charge ordering, and (d) a linear combination of these two that is ferroelectric. The arrows indicate the polarization, which is in total zero in (b) and (c), but develops a macroscopic moment, indicated by the red arrow in (d). The red dashed lines in (a), (b) and (c) indicate mirror planes of the system (from ref. [45]).

Charge ordering (CO) is a phenomenon which involves an ordering of TM ions with different valencies, or a site-centered ordering of extra electrons or holes on a metal sublattice. Thus for half-doped manganites, $x = 0.5$, one uses the picture of a checkerboard CO with alternation of formally, Mn^{3+} and Mn^{4+} ions. In Fig. 1.8 (a) a homogeneous crystal (a one-dimensional chain in this case) with equal (say zero) charge on each site is shown. Fig. 1.8 (b) shows the same chain after a charge ordering at which the sites become inequivalent, one set of sites has charge $+e$ and the other $-e$, as in NaCl. This process does not break spatial inversion symmetry, so that the resulting state cannot have a net dipole moment as seen from Fig. 1.9 (a). This is made explicit in Fig. 1.8(b) by marking mirror planes of the charge ordered structure.

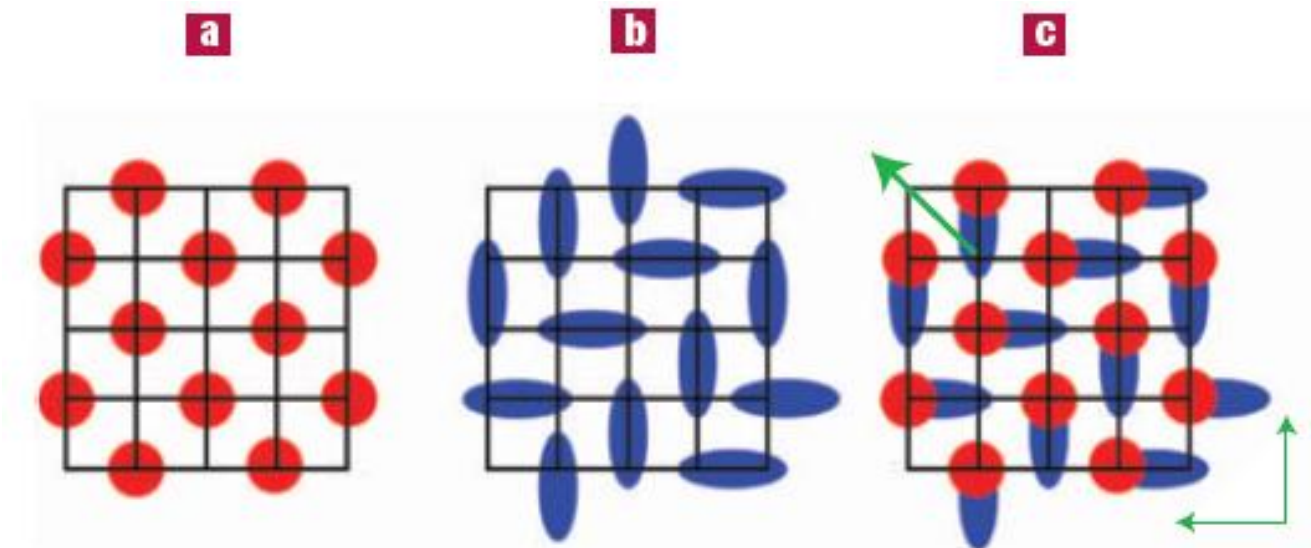


Fig. 1.9: Three types of charge ordering. (a) Site-centred charge order; (b) bond-centred charge order (the Zener polaron state); and (c) a ferroelectric intermediate state. The charge-ordered structure in c lacks inversion symmetry. Thin green arrows indicate the dipole moments of horizontal and vertical dimers, and the diagonal arrow is the total ferroelectric moment (from ref. [46]).

Another type of charge ordering occurs when a system dimerizes, where the charge is localized not on sites but on bonds, see Figs. 1.8 (c) and 1.9 (b). Such a lattice dimerization can have different origins, *e.g.* a Peierls distortion. In this case the sites remain equivalent, but the bonds are not, as the strong and weak bonds alternate. In this bond-centered CO state one extra electron is shared by the pair of neighboring Mn ions, moving back and forth between them, and thus by the double exchange mechanism, orienting the localized spins of their t_{2g} electrons parallel. Hence the terminology ‘Zener polaron’—a two-site polaron with ferromagnetic coupling. One can use the terminology of a site-centered charge ordering (SCO) or site-centered charge density wave (S-CDW) in the case of Figs. 1.8 (b) and 1.9 (a), and a bond-centered CO (BCO) or bond-centered charge density wave (B-CDW) in the case of Figs. 1.8 (c) and 1.9 (b). Also the B-CDW structure is centrosymmetric and thus cannot be ferroelectric [45].

If one now combines both types of charge ordering in one system, the situation changes drastically. The situation with simultaneous site- and bond-centered CO is schematically shown in Fig. 1.8 (d) and 1.9 (c). In this region the character of the CO actually changes in a regular way, it evolves from a pure site-centered ground state with magnetic CE-type order at $x = 0.5$, to an admixture of bond-centered state increasing with decreasing x , and finally to a pure bond-centered one around $x = 0.4$. From the figures it is immediately clear that the charge-ordering pattern of this state lacks inversion symmetry. Each molecule [short bond in Fig. 1.8(d)] develops a net dipole moment, so that as a result the whole system becomes ferroelectric. Thus solids can become ferroelectric if on top of site-centered charge ordering also a bond dimerization occurs [46]. This simultaneous presence of inequivalent sites and bonds can have a number of different origins. In some materials bonds are inequivalent just because of the crystallographic structure, and a spontaneous CO that occurs below a certain ordering

temperature drives the in equivalence of the sites. Or vice versa, the material can contain ions with different valences, which after a structural dimerization transition induce FE. These two effects may also occur simultaneously, in which case there is one common phase transition. These different charge ordered states are in general very close in energy. This observation is confirmed independently by density functional calculations [47, 48].

It is important to note some of the important characteristics of the charge-ordered manganites in order to fully understand their ferroic properties. The most important feature is that all these manganites exhibit electronic phase separation at low temperatures ($T < T_{CO}$) [49]. They exhibit a decrease in resistivity on application of large magnetic fields (> 4 T) [49, 50]. Application of electric fields also causes a significant decrease in the resistivity of the manganites [50, 51]. On the application of electric fields, the manganites show magnetic response [52]. Such electric field-induced magnetization may also be taken as evidence for coupling between the electric and magnetic order parameters in the manganites. It is likely that grain boundaries between the different electronic phases have a role in determining the dielectric behaviour. The importance of grain boundaries in giving rise to high dielectric constants has indeed been recognized [53, 54]. Besides the manganites, ferroelectricity caused by the charge ordering was also observed in LuFe_2O_4 [55], which is a charge-ordered bilayer system exhibits electric polarization at the ferromagnetic transition temperature [56, 57]. With the average valence $\text{Fe}^{2.5+}$, the ordering of Fe^{2+} and Fe^{3+} at $T_c=320$ K leads to the formation of dipoles between these layers, with the creation of total polarization, confirmed by the measurements of pyroelectric current. Ferroelectricity observed in magnetite (Fe_3O_4) is also attributed to the coexistence of charge-centered and bond-centered charge ordering.

(d) Ferroelectricity due to magnetic ordering:

Another novel class of multiferroics was observed where ferroelectricity exists only in a magnetically ordered state and is caused by particular type of magnetism. For example, in TbMnO_3 magnetic ordering appears at $T_{N1} = 41$ K, and at a lower temperature, $T_{N2} = 28$ K, the magnetic structure changes. It is only in the low temperature phase that a nonzero electric polarization appears. Similar behaviour occurs in TbMn_2O_5 . It was found that a magnetic field can strongly influence the electric polarization of TbMnO_3 , e.g. the polarization rotates (or “flops”) by 90 degrees when a critical magnetic field is applied along a certain direction [21]. Large magnetocapacitance and magnetoelectric effects are observed in TbMnO_3 due to the switching of the electric domains by the magnetic field (Fig. 1.10) [21].

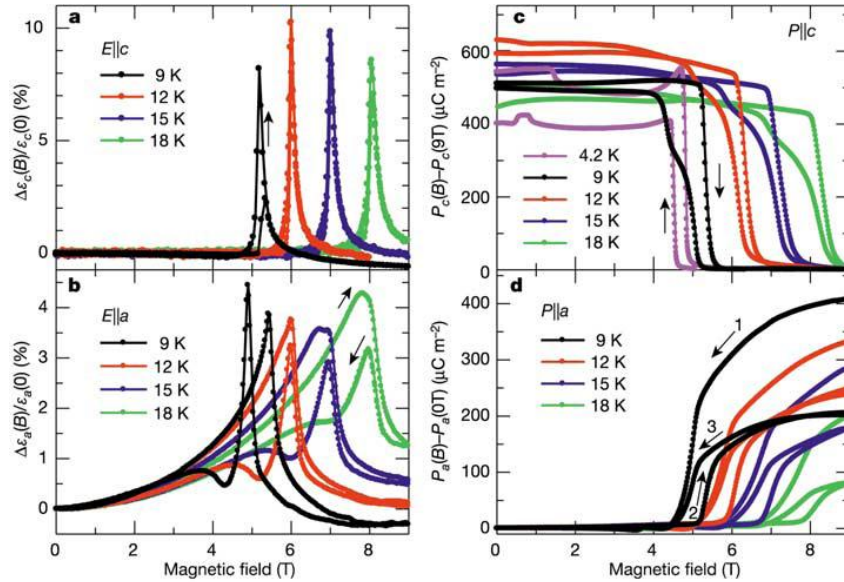


Fig. 1.10: Magnetocapacitance and magnetoelectric effects in TbMnO_3 . Magnetic field-induced change in dielectric constant (a) and (b), electric polarization along the c and a axes, respectively (c) and (d). Magnetic fields are applied along the b axis. The data of (d) were collected after the magnetic field cooling. The numbers in (d) denote the order of measurements at 9 K (from ref. [21]).

In TbMnO_3 below $T_{N1} = 41$ K the magnetic structure is a sinusoidal spin-density wave, where all spins point in one direction, but the size of the local moment varies periodically in space [Fig. 1.11]. (This is actually a sort of antiferromagnetic phase because the total moment for the magnet is zero.) Below $T_{N2} = 28$ K, the Mn spins order so that the tip of the spins sweep out a cycloid [Fig. 1.11].

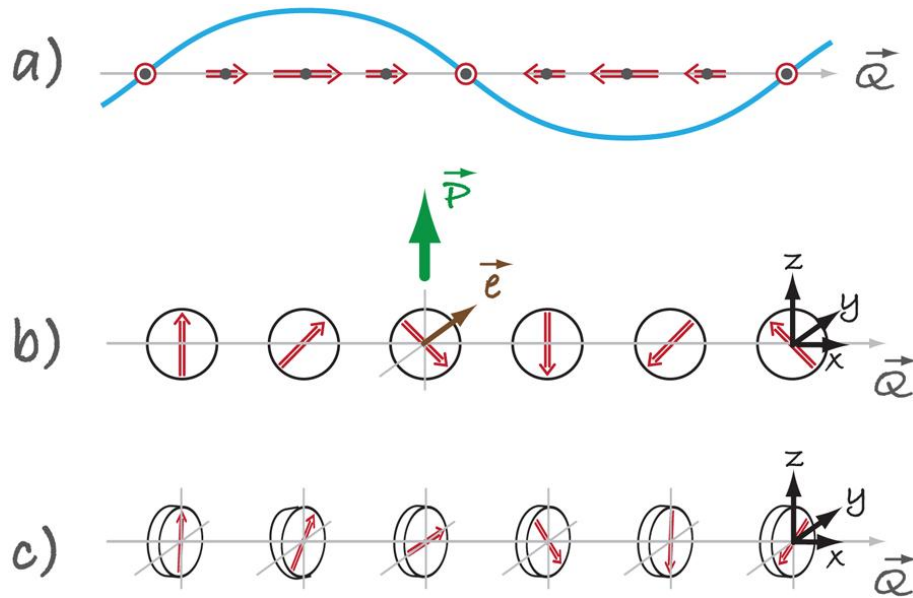


Fig. 1.11: Different types of spin structures relevant for magnetic spiral. (a) Sinusoidal spin density wave, in which spins point along one direction but vary in magnitude. This structure is centrosymmetric and consequently not ferroelectric. (b) The cycloidal spiral with the wave vector $\mathbf{Q} = \mathbf{Q}_x$ and spins rotating in the (x,z) plane. It is in this case where one finds nonzero polarization, $\mathbf{P}_z \neq 0$. (c) In a so-called “proper screw” the spins rotate in a plane perpendicular to \mathbf{Q} . Here the inversion symmetry is broken, but most often it does not produce polarization, although in certain cases it might (from ref. [61]).

Magnetic frustration is the source of spiral magnetic ordering in this material. From Fig. 1.11 it appears that FE appears in magnetic phases with the spiral, or helicoidal magnetic structures. Thus in TbMnO_3 there is no electric polarization in the phase with sinusoidal

magnetic structure between ~ 41 and 28 K, but nonzero \mathbf{P} appears below 28 K, when magnetic structure changes from the sinusoidal to a helicoidal one [58].

The existence of a spiral magnetic structure alone is not yet sufficient for FE, not all the spiral can lead to it. Katsura, Nagaosa, and Balatsky [59], using a microscopic approach, and Mostovoy [60], using a phenomenological approach, showed that in a cycloidal spiral a polarization, \mathbf{P} , appears if the spin rotation axis \mathbf{e} does not coincide with the wave vector of a spiral \mathbf{Q} and the polarization \mathbf{P} appears only if these two directions are different, and it is proportional to the vector product of \mathbf{e} and \mathbf{Q} , $\mathbf{P} \sim [\mathbf{Q} \times \mathbf{e}]$. When a magnetic field forces the plane of a magnetic cycloid to flop by 90 degrees, the polarization \mathbf{P} also flops [61], according to above equation \mathbf{P} lies in the plane of spins but perpendicular to \mathbf{Q} . Qualitatively the notion of spiral implies that the inversion symmetry is actually already broken in it. By some mechanism, most probably involving spin-orbit coupling, e.g. in the form of Dzyaloshinskii's antisymmetric exchange [62], this magnetic spiral can exert an influence on a charge and lattice subsystem, producing FE [63].

DyMnO₃ shows similar properties [64]. It is interesting to compare the magnetic properties of TbMnO₃ and DyMnO₃ with those of LaMnO₃. In LaMnO₃, orbital ordering between the neighbouring spins gives rise to ferromagnetic exchange in the a - b plane and antiferromagnetic exchange along the c axis. Replacement of La by Tb or Dy increases the structural distortion, inducing next-nearest-neighbour antiferromagnetic exchange in the a - b planes comparable to the nearest-neighbour ferromagnetic exchange. This frustrates the ferromagnetic ordering of spins in the a - b planes, and below ~ 42 K Tb(Dy)MnO₃ shows an

incommensurate magnetic ordering with a collinear sinusoidal modulation along the b axis, which is paraelectric.

LnMn_2O_5 type manganites are orthorhombic solids where the Mn^{3+} and Mn^{4+} ions occupy different crystallographic sites, with the Mn^{3+} ion at the base centre of a square pyramid and octahedrally coordinated Mn^{4+} ions [65,66]. They show sequential magnetic transitions, incommensurate sinusoidal orderings of magnetic Mn spins, commensurate antiferromagnetic ordering, re-entrant transition into the incommensurate sinusoidal state and finally ordering due to rare earth spins [67-72]. These manganites exhibit electric polarization induced by collinear spin order in a frustrated magnetic system. Ferroelectricity occurs in the temperature range 25-39 K and antiferromagnetic behaviour in the range 39-45 K [73], and the magnetic transitions are accompanied by dielectric anomalies. Magnetically induced changes in bond lengths between Mn ions with different formal valence, adding up to a net ferroelectric moment is the most plausible explanation of microscopic mechanism of ferroelectricity in this system [74]. In a magnetic field, DyMn_2O_5 shows a 100% change in the dielectric constant at 3 K, and a similar behaviour is noticed in other compounds of this family as well. In TbMn_2O_5 [75] the influence of an external field is even stronger, the polarization changes sign with field, and a field alternating between +1.5 and -1.5 Tesla leads to corresponding oscillations in the polarization. In TbMn_2O_5 , polarization is $0.04 \mu\text{C}/\text{cm}^2$ and it is magnetically reversed [75]. Reproducible polarization reversal in TbMn_2O_5 by magnetic field is shown in Fig. 1.12.

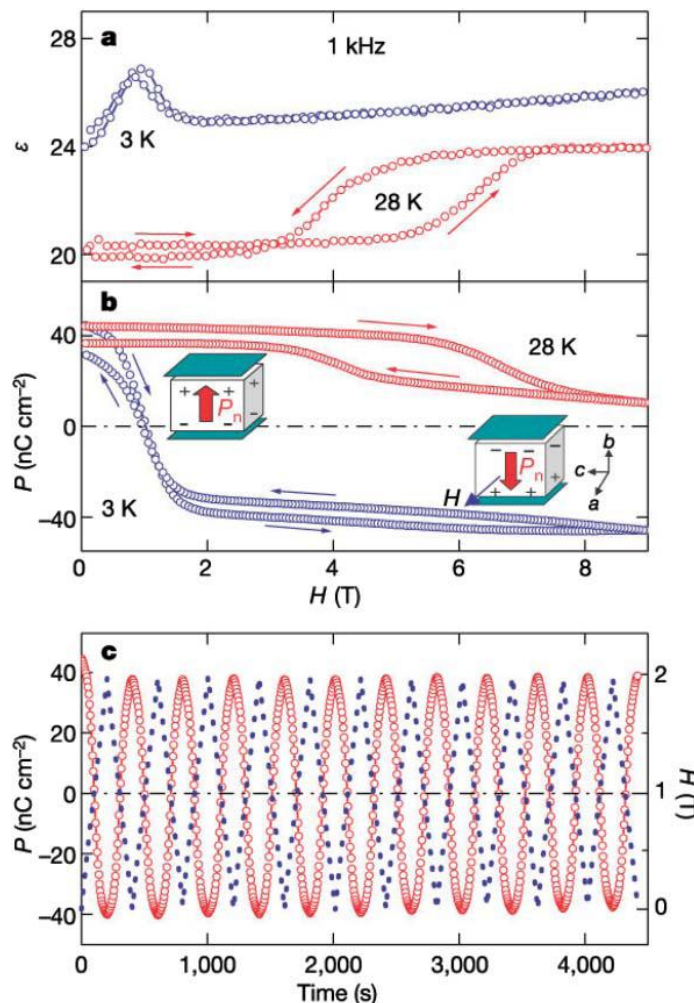


Fig. 1.12: Reproducible polarization reversal in TbMn₂O₅ by magnetic fields. (a) Dielectric constant versus applied magnetic field at 3 and 28 K. (b) Change of total electric polarization by applied magnetic fields at 3 and 28 K. (c) Polarization flipping at 3 K by linearly varying magnetic field from 0 to 2 T. The results clearly display highly reproducible polarization switching by magnetic fields (from ref. [75]).

Recent research on multiferroic systems gives an optimistic scenario wherein alternative mechanisms bring about magnetic ferroelectricity in a variety of materials. Some of the important mechanisms that have emerged relate to tilting of metal-oxygen polyhedra, spiral magnetic ordering and stereochemical activity of the Bi lone pair. In many of the multiferroic

oxides, magnetic frustration appears to give rise to novel magnetic properties which then induce ferroelectricity. The role of local non-centrosymmetry and charge ordering of mixed valent ions are two new ideas that have come to the fore. It appears that many ferroelectric materials formally possessing centrosymmetric structure may indeed have local non-centrosymmetry [76]. In principle, non-centrosymmetry can also be achieved by making use of strain, defects and other factors. Multiferroics also offer theoretical challenges besides attractive experimental possibilities. In particular, there is considerable scope for investigations of the large family of charge-ordered manganites and related materials. It is likely that a large number of materials in this family are not only multiferroic but also magnetoelectric, considering the known effects of electric and magnetic fields on these materials. There is every possibility that magnetoelectric effects in the manganites can be exploited technologically in memory devices, recording and other applications. For experimental materials scientists, the challenge of discovering materials exhibiting both magnetism and ferroelectricity with coupling between them makes the subject exciting. Some of the important aspects are related to unified theoretical development, study of spectroscopic properties and discovery of monophasic multiferroic materials showing magnetoelectric coupling.

1.5 Magnetoelectric effect:

The magnetoelectric (ME) effect in its most general definition tells about the coupling between electric and magnetic fields in matter i.e. it describes the influence of a magnetic (electric) field on the polarization (magnetization) of a material. Although increased interest to investigate the origin of the magnetoelectric (ME) effect in multiferroic materials started around 2000 the discovery of ME effect was made long back by two independent events: (i) in 1888 Röntgen discovered that a moving dielectric became magnetized when placed in an electric field [77], which was followed by the observation of the reverse effect polarization of a moving dielectric in a magnetic field [78] in the year 1905. (ii) In 1894 Curie pointed out the possibility of intrinsic ME behaviour of (non-moving) crystals on the basis of symmetry considerations [79]. The term ‘magnetoelectric’ was coined by Debye [80] a few years after the first attempts to demonstrate the static ME effect experimentally [81, 82]. In spite of Curie's early recognition of symmetry being a key issue in the search for ME behaviour, many decades passed until it was realized that the ME response is only allowed in time-asymmetric media [83]. Such violation of time-reversal symmetry can extrinsically occur through application of an external magnetic field [84] or movement as in the historic experiment conducted by Röntgen [77], or intrinsically in the form of long-range magnetic ordering. Dzyaloshinskii [85] first demonstrated the violation of time-reversal symmetry explicitly for a particular system (antiferromagnetic Cr_2O_3), which was soon followed by experimental confirmation of an electric field-induced magnetization[86,87] and a magnetic field- induced polarization [88, 89] in Cr_2O_3 , both linear in the applied field. The experiments on Cr_2O_3 constituted a breakthrough in research on the ME effect. Nevertheless the technical applications, in the form of ME switches, could not be realized due to the small magnitude of the induced polarization or magnetization. The subsequent search for alternative

multiferroics revealed the ME behavior in several materials such as Ti_2O_3 [90], GaFeO_3 [91], several boracites [15], and phosphate compounds [92], solid solutions like $\text{PbFe}_{0.5}\text{Nb}_{0.5}\text{O}_3$ [93] and garnet films [94, 95] *etc.* Soon, about eighty compounds exhibiting ME properties had been identified [96], and magnetoelectric multiferroics were proposed to be promising materials for application in devices for (i) modulation of amplitudes, polarizations and phases of optical waves, (ii) ME data storage and switching, (iii) optical diodes, (iv) spin-wave generation, (v) amplification, (vi) frequency conversion *etc* [97].

The magnetoelectric effect in a single-phase crystal is traditionally described in Landau theory by writing the free energy F of the system in terms of an applied magnetic field \mathbf{H} whose i th component is denoted H_i , and an applied electric field \mathbf{E} whose i th component is denoted E_i . Note that this convention is unambiguous in free space, but that E_i within a material encodes the resultant field that a test particle would experience. Let us consider a non-ferroic material, where both the temperature-dependent electrical polarization $P_i(\text{T})$ ($\mu\text{C}/\text{cm}^2$) and the magnetization $M_i(\text{T})$ (μ_B per formula unit, where μ_B is the Bohr magneton) are zero in the absence of applied fields and there is no hysteresis. It may be represented as an infinite, homogeneous and stress-free medium by writing F under the Einstein summation convention in S.I. units as:

$$-F(E, H) = \frac{1}{2} \varepsilon_0 \varepsilon_{ij} E_i E_j + \frac{1}{2} \mu_0 \mu_{ij} H_i H_j + \alpha_{ij} E_i H_j + \frac{\beta_{ijk}}{2} E_i H_j H_k + \frac{\gamma_{ijk}}{2} H_i E_j E_k + \dots \quad (1.1)$$

The first term on the right hand side describes the contribution resulting from the electrical response to an electric field, where the permittivity of free space is denoted ε_0 , and the relative permittivity $\varepsilon_{ij}(\text{T})$ is a second-rank tensor that is typically independent of E_i in non-ferroic materials. The second term is the magnetic equivalent of the first term, where $\mu_{ij}(\text{T})$ is the relative permeability and μ_0 is the permeability of free space. The third term describes linear

magnetolectric coupling via α_{ij} (T); the third-rank tensors β_{ijk} (T) and γ_{ijk} (T) represent higher-order (quadratic) magnetolectric coefficients. In the present scheme, all magnetolectric coefficients incorporate the field independent material response functions ε_{ij} (T) and μ_{ij} (T). The magnetolectric effects can then easily be established in the form $P_i(H_j)$ or $M_i(E_j)$. The former is obtained by differentiating F with respect to E_i , and then setting $E_i = 0$. A complementary operation involving H_i establishes the latter. One obtains:

$$P_i = \alpha_{ij}H_j + \frac{\beta_{ijk}}{2}H_jH_k + \dots \quad (1.2)$$

$$\mu_0 M_i = \alpha_{ji}E_j + \frac{\gamma_{ijk}}{2}E_jE_k + \dots \quad (1.3)$$

In ferroic materials, the above analysis is less rigorous because ε_{ij} (T) and μ_{ij} (T) display field hysteresis. Moreover, ferroics are better parameterized in terms of resultant rather than applied fields. This is because it is then possible to account for the potentially significant depolarizing/demagnetizing factors infinite media, and also because the coupling constants would then be functions of temperature alone, as in standard Landau theory. In practice, resultant electric and magnetic fields may sometimes be approximated [42] by the polarization and magnetization respectively. A multiferroic that is ferromagnetic and ferroelectric is liable to display large linear magnetolectric effects. This follows because ferroelectric and ferromagnetic materials often (but not always) possess a large permittivity and permeability respectively, and α_{ij} is bounded by the geometric mean of the diagonalized tensors ε_{ii} and μ_{jj} such that [98]:

$$\alpha_{ij}^2 \leq \varepsilon_0 \mu_0 \varepsilon_{ii} \mu_{jj} \quad (1.4)$$

Equation (1.4) is obtained from equation (1.1) by forcing the sum of the first three terms to be greater than zero, that is, ignoring higher-order coupling terms. It represents a stability condition on ε_{ij} and μ_{ij} , but if the coupling becomes so strong that it drives a phase transition to a more stable state, then α_{ij} , ε_{ij} and μ_{ij} take on new values in the new phase. Note that a large ε_{ij} is not a prerequisite for a material to be ferroelectric (or vice versa); and similarly ferromagnets do not necessarily possess large μ_{ij} . For example, the ferroelectric KNO_3 possesses a small $\varepsilon = 25$ near its Curie temperature of 120°C [99], whereas paraelectric SrTiO_3 exhibits $\varepsilon > 50,000$ at low temperatures [100]. Therefore large magnetoelectric couplings need not arise in, or be restricted to, multiferroic materials.

Nonlinear Coupling:

Most materials have small values of either ε_{ij} or μ_{ij} or both, so the linear magnetoelectric effect will also be small, given that permittivity and permeability appear as a product in equation (1.4). However, no such restriction applies to higher-order couplings, such as those described by β_{ijk} and γ_{ijk} . For example, in some materials terms such as $\beta_{ijk} H_j H_k$ can dominate the linear term $\alpha_{ij} H_j$ in equation (1.2), as first shown experimentally at low temperatures in the piezoelectric paramagnet $\text{NiSO}_4 \cdot 6\text{H}_2\text{O}$ [101]. In order to achieve large magnetoelectric effects at room temperature through higher-order terms, we suggest investigating magnetic materials with reduced dimensionality. Indeed, two-dimensional spin order associated with β (T) can persist to a temperature T_{2D} that exceeds the temperature T_{3D} at which three-dimensional spin order associated with α (T) is destroyed. This scenario arises [102] at low temperature in BaMnF_4 .

Indirect Coupling:

So far, our discussion of linear and higher-order magnetoelectric coupling has ignored the effects of strain. Such effects could be significant or even dominant. For example, the inclusion of piezomagnetism (magnetostriction) would generate cross terms in equation (1.1) that are proportional to strain and vary linearly (quadratically) with H_i . Analogous expressions would arise from piezoelectricity or electrostriction. Furthermore, mixed terms involving products of strain, H_i and E_j have been predicted [103]. In two-phase materials, magnetic and electrical properties are strain-coupled by design in the quest for large magnetoelectric effects. The strength of this indirect coupling is not restricted by equation (1.4), and enhancements over single-phase systems of several orders of magnitude have been achieved [104].

REFERENCES:

1. Weiss, P., *J. Phys.*, 1907, **6**, 661.
2. Stoner, E. C., *Philos. Mag.*, 1933, **15**, 1018.
3. Goodenough, J. B., *Phys. Rev.*, 1955, **100**, 564.
4. Kanamori, J., *J. Phys. Chem. Solids*, 1959, **10**, 87.
5. Anderson, P. W., *Phys. Rev.*, 1959, **115**, 2.
6. Anderson, P. W., *Academic Press*, New York, (1963).
7. Goodenough, J. B., *Interscience Publisher*, New York, (1963).
8. Jona, F. and Shirane, G., *Pergamon Press*, New York, (1962).
9. Cohen, R. E., *Nature*, 1992, **358**, 136.
10. Levanyuk, A. P. and Sannikov, D. G., *Sov. Phys. Usp.*, 1974, **17**, 199.
11. Fennie, C. J. and Rabe, K. M., *Phys. Rev. B: Condens. Matter*, 2005, **72**, 100103.
12. Van Aken, B. B., Palstra, T. T. M., Filippetti, A. and Spaldin, N. A., *Nat. Mater.*, 2004, **3**, 164.
13. Schmid, H., *Ferroelectrics*, 1994, **162**, 317.
14. Eerenstein, W., Mathur, N. D. and Scott, J. F., *Nature*, 2006, **442**, 759.
15. Ascher, E., Rieder, H., Schmid, H. and Stössel, H., *J. Appl. Phys.*, 1966, **37**, 1404.
16. Smolensky, G. A.; Agranovskaya, A. I.; Isupov, V. A. *Sov. Phys. Solid State*, 1959, **1**, 149.
17. Smolensky, G. A.; Isupov, V. A.; Krainik, N. N.; Agranovskaya, A. I. *Isvest. Akad. Nauk SSSR, Ser. Fiz.*, 1961, **25**, 1333.
18. J. R. Teage, R. Gerson and W. J. James, *Solid State Commun.*, 1970, **8**, 1073.
19. R. Seshadri and N. A. Hill, *Chem. Mater.*, 2001, **13**, 2892.

20. A. M. dos Santos, S. Parashar, A. R. Raju, Y. S. Zhao, A. K. Cheetham and C. N. R. Rao, *Solid State Commun.*, 2002, **122**, 49.
21. T. Kimura, T. Goto, H. Shintani, K. Ishizaka, T. Arima and Y. Tokura, *Nature*, 2003, **426**, 55.
22. D. V. Efremov, J. van den Brink and D. I. Khomskii, *Nat. Mater.*, 2004, **3**, 853.
23. Teague, J. R., Gerson, R. and James, W. J., *Solid State Commun.*, 1970, **8**, 1073.
24. Sosnowska, I., Neumaier, T. P. and Steichele, E., *J. Phys. C: Solid State Phys.*, 1982, **15**, 4835.
25. Popov, Y. F., Kadomtseva, A. M., Vorobev, G. P. and Zvezdin, A. K., *Ferroelectrics*, 1994, **162**, 135.
26. Murashov, V. A., Rakov, D. N., Ionov, V. M., Dubenko, I. S., Titov, Y. V. and Gorelik, V. S., *Ferroelectrics*, 1994, **162**, 11.
27. Bai, F., Wang, J., Wuttig, M., Li, J., Wang, N., Pyatakov, A. P., Zvezdin, A. K., Cross, L. E. and Viehland, D., *Appl. Phys. Lett.*, 2005, **86**, 032511.
28. Kimura, T., Kawamoto, S., Yamada, I., Azuma, M., Takano, M. and Tokura, Y., *Phys. Rev. B: Condens. Matter*, 2003, **67**, 1804011.
29. dos Santos, A. M., Cheetham, A. K., Atou, T., Syono, Y., Yamaguchi, Y., Ohoyama, K., Chiba, H. and Rao, C. N. R., *Phys. Rev. B: Condens. Matter*, 2002, **66**, 644251.
30. Belik, A. A., Iikubo, S., Yokosawa, T., Kodama, K., Igawa, N., Shamoto, S., Azuma, M., Takano, M., Kimoto, K., Matsui, Y. and Takayama-Muromachi, E., *J. Am. Chem. Soc.*, 2007, **129**, 971.
31. Niitaka, S., Azuma, M., Takano, M., Nishibori, E., Takata, M. and Sakata, M., *Solid State Ionics*, 2004, **172**, 557.

32. Hughes, H., Allix, M. M. B., Bridges, C. A., Claridge, J. B., Kuang, X., Niu, H., Taylor, S., Song, W. and Rosseinsky, M. J., *J. Am. Chem. Soc.*, 2005, **127**, 13790.
33. Azuma, M., Takata, K., Saito, T., Ishiwata, S., Shimakawa, Y. and Takano, M., *J. Am. Chem. Soc.*, 2005, **127**, 8889.
34. Rogado, N. S., Li, J., Sleight, A. W. and Subramanian, M. A., *Adv. Mater.*, 2005, **17**, 2225.
35. D. I. Khomskii, *Physica Scripta*, 2005, **72**, CC8 (Comments *Cond.Matter Physics*); condmat/0508631.
36. Ramesh, R. and Spaldin, N. A., *Nat. Mater.*, 2007, **6**, 21.
37. D. I. Khomskii, *J. Magn. Magn. Mater.*, 2006, **00**, 000–0001.
38. Fiebig, M., Lottermoser, T., Frohlich, D., Goltsev, A. V. and Pisarev, R. V., *Nature*, 2002, **419**, 818.
39. Goltsev, A. V., Pisarev, R. V., Lottermoser, T. and Fiebig, M., *Phys. Rev. Lett.*, 2003, **90**, 177204.
40. Lee, S., Pirogov, A., Han, J. H., Park, J., Hoshikawa, A. and Kamiyama, T., *Phys. Rev. B: Condens. Matter*, 2005, **71**, 180413.
41. Sharma, P. A., Ahn, J. S., Hur, N., Park, S., Kim, S. B., Lee, S., Park, J., Guha, S. and Cheong, S., *Phys. Rev. Lett.*, 2004, **93**, 177202.
42. Lottermoser, T., Lonkai, T., Amann, U., Hohlwein, D., Ihringer, J. and Fiebig, M., *Nature*, 2004, **430**, 541.
43. Lorenz, B., Wang, Y. Q., Sun, Y. Y. and Chu, C. W., *Phys. Rev. B: Condens. Matter*, 2004, **70**, 212412.

-
44. Van Aken, B. B. and Palstra, T. T. M., *Phys. Rev. B: Condens. Matter*, 2004, **69**, 134113.
 45. van den Brink, J. and Khomskii, D. I., *J. Phys.: Condens. Matter*, 2008, **20**, 434217.
 46. Efremov, D. V., van den Brink, J. and Khomskii, D. I., *Nat. Mater.*, 2004, **3**, 853.
 47. Efremov, D. V. and Khomskii, D. I., *Phys. Rev. B: Condens. Matter*, 2005, **72**, 012402.
 48. Wang, C., Guo, G. and He, L., *Phys. Rev. Lett.*, 2007, **99**, 177202.
 49. Shenoy, V. B., Sarma, D. D. and Rao, C. N. R., *Chem Phys Chem*, 2006, **7**, 2053.
 50. Rao, C. N. R., $\text{Ln}_{1-x}\text{A}_x\text{MnO}_3$ (Ln = Rare Earth, A = Ca or Sr), *J. Phys. Chem. B*, 2000, **104**, 5877.
 51. Parashar, S., Sudheendra, L., Raju, A. R. and Rao, C. N. R., *J. Appl. Phys.*, 2004, **95**, 2181.
 52. Guha, A., Khare, N., Raychaudhuri, A. K. and Rao, C. N. R., *Phys. Rev. B: Condens. Matter*, 2000, **62**, R11941.
 53. Lunkenheimer, P., Bobnar, V., Pronin, A. V., Ritus, A. I., Volkov, A. A. and Loidl, A., *Phys. Rev. B: Condens. Matter*, 2002, **66**, 521051.
 54. Sudheendra, L. and Rao, C. N. R., *J. Phys.: Condens. Matter*, 2003, **15**, 3029.
 55. N. Ikeda, et al., *J. Phys. Soc. Jpn*, 2000, **69**, 1526.
 56. N. Ikeda, H. Ohsumi, K. Ohwada, K. Ishii, T. Inami, K. Kakurai, Y. Murakami, K. Yoshii, S. Mori, Y. Horibe and H. Kito, *Nature*, 2005, **436**, 1136.
 57. M. A. Subramanian, T. He, J. Chen, N. S. Rogado, T. G. Calvarese and A. W. Sleight, *Adv. Mater.*, 2006, **18**, 1737.
 58. M. Kenzelman et al., *Phys. Rev. Lett.*, 2005, **95**, 087206.

59. H. Katsura, N. Nagaosa, and A. V. Balatsky, *Phys. Rev. Lett.*, 2005, **95**, 057205.
60. M. V. Mostovoy, *Phys. Rev. Lett.*, 2006, **96**, 067601.
61. T. Arima, *J. Phys. Soc. Jpn.*, 2007, **76**, 073702.
62. E. Sergienko and E. Dagotto, *cond-mat/0508075*
63. P. W. Anderson and E. I. Blount, *Phys. Rev. Lett.*, 1965, **14**, 217.
64. Prokhnenko, O., Feyerherm, R., Dudzik, E., Landsgesell, S., Aliouane, N., Chapon, L. C. and Argyriou, D. N., *Phys. Rev. Lett.*, 2007, **98**, 057206.
65. A. Alonso, M. R. T. Casas, M. J. Martinez-Lope and I. Rasines, *J. Solid State Chem.*, 1997, **129**, 105.
66. S. C. Abrahams and J. L. Bernstein, *J. Chem. Phys.*, 1967, **46**, 3776.
67. S. Quezel-Ambrunaz, F. Bertaut and G. Buisson, *Compt. Rend.*, 1964, **258**, 3025.
68. M. Schieber, A. Grill, I. Nowik, B. M. Y. Wanklyn, R. C. Sherwood and L. G. van Uiter, *J. Appl. Phys.*, 1973, **44**, 1864.
69. E. I. Golovenchits, N. V. Morozov, V. A. Sanina and L. M. Sapozhnikova, *Sov. Phys. Solid State*, 1992, **34**, 56.
70. Saito and K. Kohn, *J. Phys.: Condens. Matter*, 1995, **7**, 2855.
71. A. Inomata and K. Kohn, *J. Phys.: Condens. Matter*, 1996, **8**, 2673.
72. P. P. Gardner, C. Wilkinson, J. B. Forsyth and B. M. Wanklyn, *J. Phys. C: Solid State Phys.*, 1998, **21**, 5653.
73. Kagomiya, I., Kohn, K. and Uchiyama, T., 2002, **280**, 131.
74. Cheong, S. W. and Mostovoy, M., *Nat. Mater.*, 2007, **6**, 13.
75. Hur, N., Park, S., Sharma, P. A., Ahn, J. S., Guha, S. and Cheong, S. W., *Nature*, 2004, **429**, 392.

-
76. C. N. R. Rao and C. R. Serrao, *J. Mater. Chem.*, 2007, **17**, 4931.
 77. Rontgen, W. C. *Ann. der Phys.*, 1888, **35**, 264.
 78. Wilson, H. A. *Phil. Trans. R. Soc. A*, 1905, **204**, 129.
 79. Curie, P., *J. Phys. (Paris)*, 1894, **3**, 393.
 80. Debye, P., *Zeitschrift fur Physik*, 1926, **36**, 300.
 81. Perrier, A. and Staring, A. J. *Arch. Sci. Phys. Nat.*, 1922, **4**, 373.
 82. Perrier, A. and Staring, A. J. *Arch. Sci. Phys. Nat.*, 1923, **5**, 333.
 83. Landau, L. D. and Lifshitz, E. M., *Oxford: Pergamon*, (1960).
 84. Van Vleck, J. H., *Oxford University Press*, London, (1932).
 85. Dzyaloshinskii, I. E., *Sov. Phys. JETP*, 1960, **10**, 628.
 86. Astrov, D. N., *Sov. Phys. JETP*, 1960, **11**, 708.
 87. Astrov, D. N., *Sov. Phys. JETP*, 1961, **13**, 729.
 88. Rado, G. T. and Folen, V. J., *Phys. Rev. Lett.*, 1961, **7**, 310.
 89. Folen, V. J., Rado, G. T. and Stalder, E. W., *Phys. Rev. Lett.*, 1961, **6**, 607.
 90. Alshin, B. I. and Astrov, D. N., *Sov. Phys. JETP*, 1963, **17**, 809.
 91. Rado, G. T., *Phys. Rev. Lett.*, 1964, **13**, 335.
 92. Santoro, R. P., Segal, D. J. and Newnham, R. E., *J. Phys. Chem. Solids*, 1966, **27**, 1192.
 93. Watanabe, T. and Kohn, K., 1989, **15**, 57.
 94. O'Dell, T. H., *Philos. Mag.*, 1967, **16**, 487.
 95. Krichevtsov, B. B., Pavlov, V. V., Pisarev, R. V. and Selitsky, A. G., *Ferroelectrics*, 1993, **161**, 65.
 96. Schmid, H., *Int. J. Magn.*, 1973, **4**, 337.

97. Woods, V. E. and Austin, A. E., *Int. J. Magn.*, 1974, **5**, 303.
98. Brown, W. F. Jr., H. R. M. and Shtrikman, S., *Phys. Rev.*, 1968, **168**, 574.
99. Chen, A. and Chernow, F., *Phys. Rev.*, 1967, **154**, 493.
100. Saifi, M. A. and Cross, L. E., *Phys. Rev. B: Condens. Matter*, 1970, **2**, 677.
101. Hou, S. L. and Bloembergen, N., *Phys. Rev.*, 1965, **138**, A1218.
102. Scott, J. F., *Phys. Rev. B: Condens. Matter*, 1977, **16**, 2329.
103. Grimmer, H., *Acta Crystallogr.*, 1992, **A48**, 266.
104. Ryu, J., Carazo, A. V., Uchino, K. and Kim, H. E., *Jpn. J. Appl. Phys.*, 2001, **40**, 4948.

***Al_{1-x}Ga_xFeO₃ family of oxides:
magnetic and dielectric
properties***

Summary*

Al_{1-x}Ga_xFeO₃ family of oxides crystallizing in a non-centrosymmetric space group show interesting magnetic and dielectric properties, which was investigated in detail along with structural aspects by employing X-ray and neutron diffraction, Mössbauer spectroscopy and other techniques. The study has revealed the occurrence of several interesting features related to unit cell parameters, site disorder and ionic size. First-principles density functional theory based calculations performed by Prof. U. V. Waghmare *et al.* show that magnetic ordering and related properties in these oxides depend sensitively on disorder at the cation site. The origin and tendency of cations to disorder and the associated properties are traced to the local structure and ionic sizes.

More importantly, magnetodielectric properties of multiferroic Al_{1-x}Ga_xFeO₃ family of oxides (x = 0, 1) have been investigated. The nature of the A-cations as well as cation disorder has a significant effect on dielectric and related properties. GaFeO₃ is found to be multiferroic and also to show large magnetocapacitance at 300 K, exceeding the performance of AlFeO₃. Also interesting changes in magnetic properties are found on substitution of isovalent Cr³⁺ in GaFeO₃. Substitution of Cr³⁺ in Fe site reduces the

**Papers based on these studies have appeared in J. Mater. Chem. (2011) and J. Solid State Chem. (2011).*

magnetic ordering temperature, while it increases slightly when Cr^{3+} is doped in the Ga site of GaFeO_3 .

2.1 Introduction:

Multiferroic oxides are not common since it is difficult to satisfy the criteria required for magnetism and ferroelectricity in the same material [1-3]. However, there are a few materials which show multiferroic properties because of mechanisms different from those in conventional ferroelectrics such as BaTiO_3 . All multiferroic materials are not necessarily magnetoelectric because the latter property arises from the interaction between the magnetic and the electric order parameters [1-3]. Al_2O_3 , Ga_2O_3 and Fe_2O_3 are known to crystallize in the rhombohedral structure. Metastable orthorhombic phases ($Pna2_1$) of these materials are also known [4]. Surprisingly the stable structures of AlFeO_3 and GaFeO_3 belong to the non-centrosymmetric chiral space group with an orthorhombic ($Pna2_1$) structure [5-7]. AlFeO_3 and GaFeO_3 are reported to be ferrimagnetic [8-10]. These materials are also expected to be multiferroic. These materials also exhibit magnetodielectric properties, with GaFeO_3 showing unusually large magnetocapacitance at 300 K. In view of their unusual properties, the structure and magnetic properties of AlFeO_3 and GaFeO_3 have been investigated in detail by carrying out a neutron diffraction study of the structures, along with magnetic and Mössbauer measurements to establish the nature of magnetic properties. First-principles density functional theory calculations have been carried out to understand the properties of these materials in relation to their structures.

2.2 Scope of the present investigations:

It has been reported that AlFeO_3 , which is derived from Fe_2O_3 by the substitution of one Fe^{3+} by Al^{3+} , shows ferrimagnetic as well as ferroelectric properties, unlike the parent binary oxides, Al_2O_3 and Fe_2O_3 . Magnetodielectric properties of multiferroic AlFeO_3 are not established. So multiferroic and magnetodielectric properties of $\text{Al}_{1-x}\text{Ga}_x\text{FeO}_3$ ($x = 0, 1$) have been studied. More importantly, investigation of magnetic properties of $\text{Al}_{1-x}\text{Ga}_x\text{FeO}_3$ was carried out to understand that how magnetic ordering and related properties in these oxides depend sensitively on disorder at the cation site. The origin and tendency of cations to disorder and the associated properties are strongly related to the local structure and ionic sizes. Also doping effect of Cr^{3+} on multiferroic GaFeO_3 was studied and it showed interesting changes in magnetic transition temperature.

2.3 Experimental:

AlFeO_3 and GaFeO_3 were prepared by the co-precipitation method [10] starting from stoichiometric amounts of Fe_2O_3 (99.9%) and Al (Ga_2O_3) (99.9%) powder. The powders were dissolved separately in conc. HCl to form the chlorides of the metal ion. Respective metal chloride solutions were mixed and stirred for half an hour. After that NH_4OH solution was added drop by drop with continuous stirring until rich precipitation. The precipitate was filtered, washed with distilled water to remove the residual ammonium chloride salt until neutral pH and dried at $80\text{ }^\circ\text{C}$ in an air oven for 24 hrs. The dried powders were grounded, pelletized and sintered at $1350\text{ }^\circ\text{C}$ for 2 hours in air with a heating rate of $3\text{ }^\circ\text{C}/\text{min}$. These oxides were also prepared by the ceramic method by

heating mixtures of the component oxides at 1400 °C with a repeated grinding, pelletizing and heating. Other compositions of $\text{Al}_{1-x}\text{Ga}_x\text{FeO}_3$ were also prepared by the ceramic method. The polycrystalline $\text{GaFe}_{1-x}\text{Cr}_x\text{O}_3$ ($x = 0.05, 0.1$ and 0.2) and $\text{Ga}_{1-x}\text{Cr}_x\text{FeO}_3$ ($x = 0.05$ and 0.1) samples were prepared by solid state reaction method. First appropriate amounts of Cr_2O_3 (99.9%) was substituted to Fe_2O_3 (or Ga_2O_3) (99.9%) by grinding followed by heating at 1000°C and then it was mixed with Ga_2O_3 (or Fe_2O_3) maintaing the 1:1 ratio .This mixture was reground thoroughly, pelletized and sintered at 1300°C (12 h).

Phase purities of these oxides were confirmed by recording the X-ray diffraction patterns with a Bruker D8 Advance X-ray diffractometer and all of them were found to crystallize in orthorhombic structure (space group $Pna2_1$). A software package Fullprof was used to analyze the structural data. Neutron powder diffraction measurements on polycrystalline $\text{Al}_{1-x}\text{Ga}_x\text{FeO}_3$ ($x = 0, 1$) samples were carried out at BARC by Dr. S. M. Yusuf *et al.* over the temperature range of 5-300 K using the five linear position sensitive detector (PSD) based powder diffractometer ($\lambda=1.2443 \text{ \AA}$). The powdered sample was placed in a cylindrical vanadium container and a commercial closed cycle helium refrigerator was used for low temperature measurements.

DC magnetization measurements were carried out using a vibrating sample magnetometer in Physical Property Measurement System (PPMS) under zero-field-cooled (ZFC) and field-cooled (FC) condition in the temperature range of 10 to 330 K under a magnetic field of 100 Oe. Magnetic hysteresis curves were recorded at 5 K in magnetic fields going up to 60 kOe. Dielectric measurements were carried out with an

Impedance Analyzer (Agilent 4294A) using compensated cable wire in a 4TP-2T configuration. Silver paint was used as electrode and the sample was placed in a custom made sample holder which goes inside the sample chamber of a 14 Tesla magnet cryo-cooled cyclic refrigerator system. Mössbauer spectra were recorded by Dr. Y. Sundarayya in transmission mode using ^{57}Co γ -ray source in a Rhodium matrix and multi-channel analyzer. The sample thickness was adjusted so that the Fe content was approximately 10 mg/cm^2 . Calibrations of velocity and isomer shift were performed using α -iron (Fe) foil. Measurements at low temperatures were carried out using a helium close cycle cooler system attached to the sample chamber.

2.4 Results and Discussion:

2.4.1 Structure:

To investigate the crystal structures of $\text{Al}_{1-x}\text{Ga}_x\text{FeO}_3$ family of oxides, PXRD as well as neutron diffraction were carried out and found that AlFeO_3 crystallizes in orthorhombic structure with the chiral, non-centrosymmetric $Pna2_1$ space group. GaFeO_3 has a structure similar to that of AlFeO_3 with a non-centrosymmetric space group [11].

(a) XRD results of AlFeO_3 & GaFeO_3

X-ray diffraction measurements on AlFeO_3 and GaFeO_3 carried out by us gave the following lattice parameters: $a = 4.9806(3) \text{ \AA}$, $b = 8.5511(6) \text{ \AA}$ and $c = 9.2403(6) \text{ \AA}$ for AlFeO_3 ; $a = 5.0814(2) \text{ \AA}$, $b = 8.7436(3) \text{ \AA}$ and $c = 9.3910(2) \text{ \AA}$ for GaFeO_3 . The space group of both these oxides is $Pna2_1$. X-ray Diffraction measurements showed that $\text{Al}_{0.5}\text{Ga}_{0.5}\text{FeO}_3$ also crystallizes in the $Pna2_1$ space group with the lattice parameters, $a =$

5.0306(1) Å, $b = 8.6461(2)$ Å, and $c = 9.3175(2)$ Å. These parameters are in between those of AlFeO_3 and GaFeO_3 . In Fig. 2.1, X-ray diffraction patterns of AlFeO_3 and GaFeO_3 are shown along with profile fits and difference patterns to show how they possess the same structure.

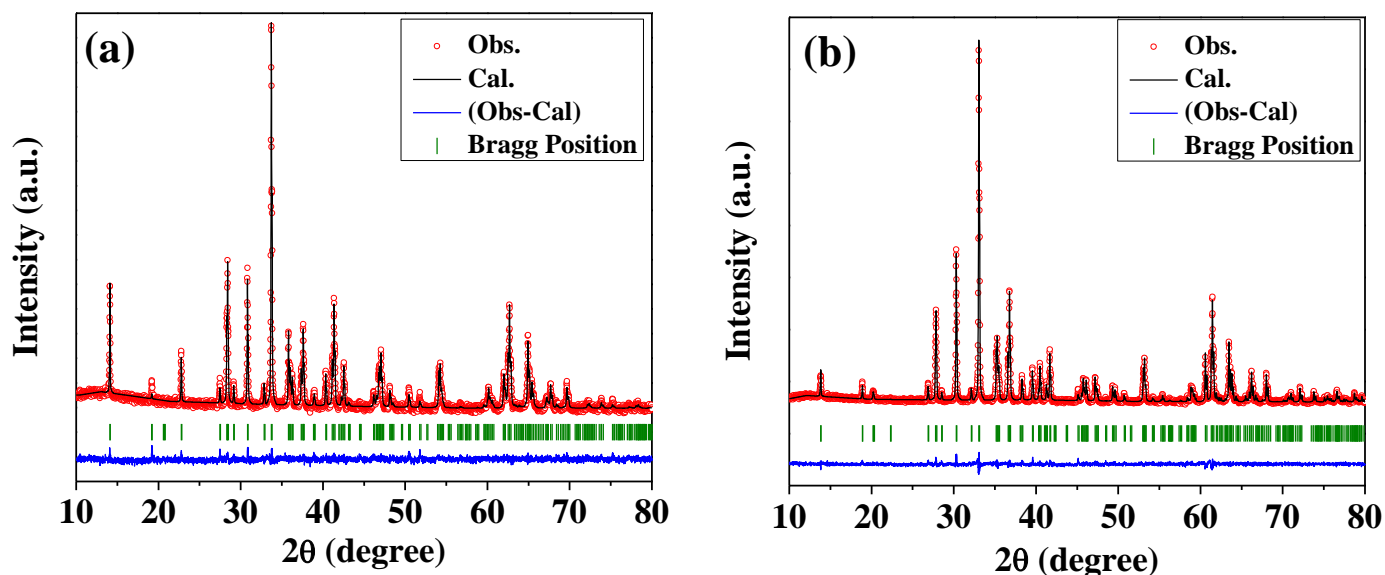


Fig. 2.1: XRD patterns of (a) AlFeO_3 and (b) GaFeO_3 along with profile fits, difference patterns and Bragg positions.

A series of compounds of $\text{Al}_{1-x}\text{Ga}_x\text{FeO}_3$ ($x = 0.3, 0.7, 0.9$) made by solid state reaction were studied using PXRD. It was found that all of them crystallize in orthorhombic structure with the chiral, non-centrosymmetric $Pna2_1$ space group. In Fig. 2.2, X-ray diffraction patterns of $\text{Al}_{1-x}\text{Ga}_x\text{FeO}_3$ compositions are shown along with profile fits and difference patterns. In the $\text{Al}_{1-x}\text{Ga}_x\text{FeO}_3$ ($x = 0.3, 0.7, 0.9$) compositions, the unit cell parameters and volume increase linearly with the Ga content as shown in Figs. 2.3 and 2.4.

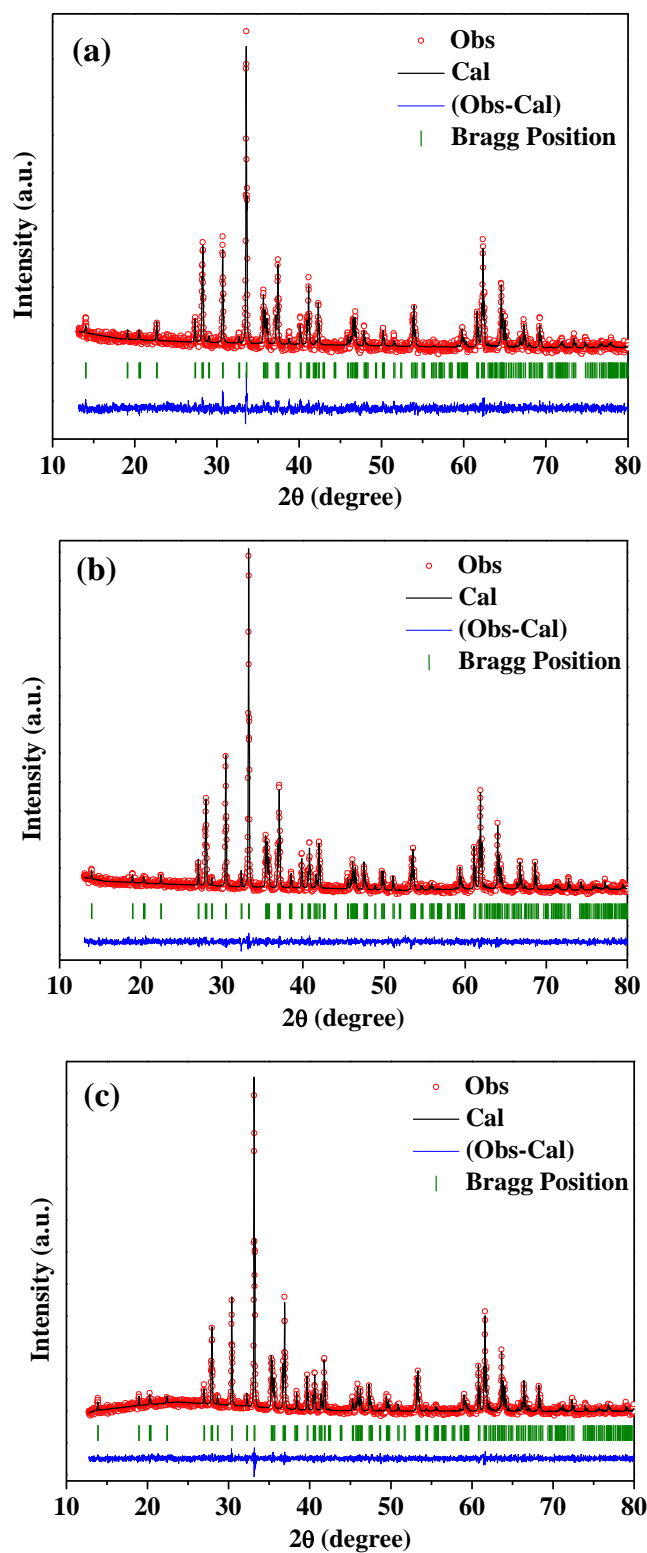


Fig. 2.2: XRD patterns of (a) $\text{Al}_{0.7}\text{Ga}_{0.3}\text{FeO}_3$, (b) $\text{Al}_{0.3}\text{Ga}_{0.7}\text{FeO}_3$ and (c) $\text{Al}_{0.1}\text{Ga}_{0.9}\text{FeO}_3$ along with profile fits, difference patterns and Bragg positions.

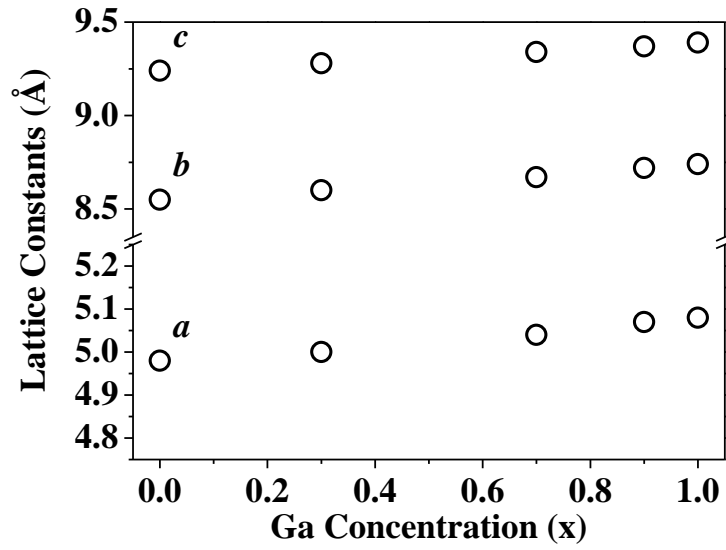


Fig. 2.3: Variation of lattice constants in $\text{Al}_{1-x}\text{Ga}_x\text{FeO}_3$ with Ga content at 300 K obtained from XRD.

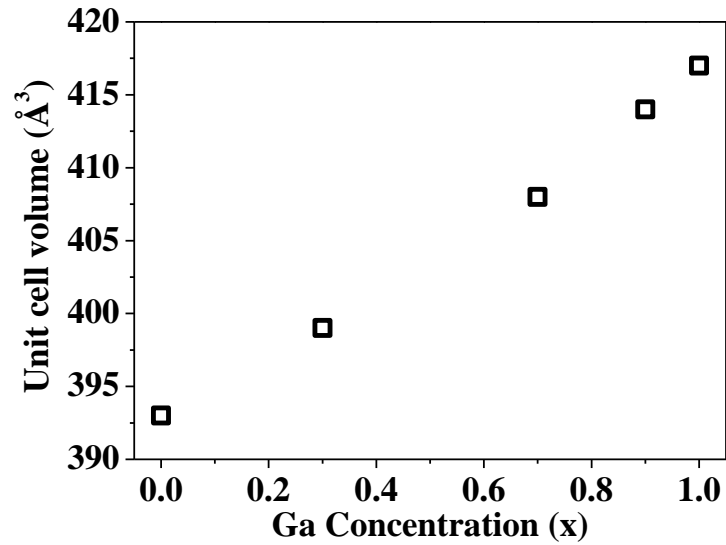


Fig. 2.4: Variation of unit cell volume in $\text{Al}_{1-x}\text{Ga}_x\text{FeO}_3$ as a function of Ga content at 300 K obtained from XRD.

Table I

Lattice parameters and unit cell volume of $\text{Al}_{1-x}\text{Ga}_x\text{FeO}_3$ ($x= 0, 0.3, 0.7, 0.9, 1$)

Compound formula	a (Å)	b (Å)	c (Å)	Unit cell volume (Å ³)
AlFeO_3	4.9806(3)	8.5511(6)	9.2403(6)	393
$\text{Al}_{0.7}\text{Ga}_{0.3}\text{FeO}_3$	5.0049(3)	8.5998(5)	9.2848(5)	400
$\text{Al}_{0.3}\text{Ga}_{0.7}\text{FeO}_3$	5.0443(1)	8.6728(3)	9.3395(3)	409
$\text{Al}_{0.1}\text{Ga}_{0.9}\text{FeO}_3$	5.0688(2)	8.7165(3)	9.3705(3)	414
GaFeO_3	5.0814(2)	8.7436(3)	9.3910(2)	417

(b) Neutron diffraction results of AlFeO_3

A detailed neutron diffraction study was carried out on AlFeO_3 . Fig. 2.5 shows the observed and Rietveld refined neutron diffraction patterns for AlFeO_3 at 300, 250, 150, 50 and 5 K. The Rietveld analysis of the neutron diffraction patterns confirm the single phase formation of the compound with the orthorhombic crystal structure under the space group $Pna2_1$. At 300 K, the observed diffraction pattern could be fitted with only nuclear intensities confirming the paramagnetic nature of the sample. In the Rietveld refinement, the coherent nuclear scattering lengths of 0.9450×10^{-12} , 0.3449×10^{-12} , and 0.5803×10^{-12} cm for Al, Fe, and O, respectively, have been used. The refined lattice parameters and other structural parameters are given in Table II. The values of the lattice parameters are in good agreement with the earlier reported values for the same compound [5].

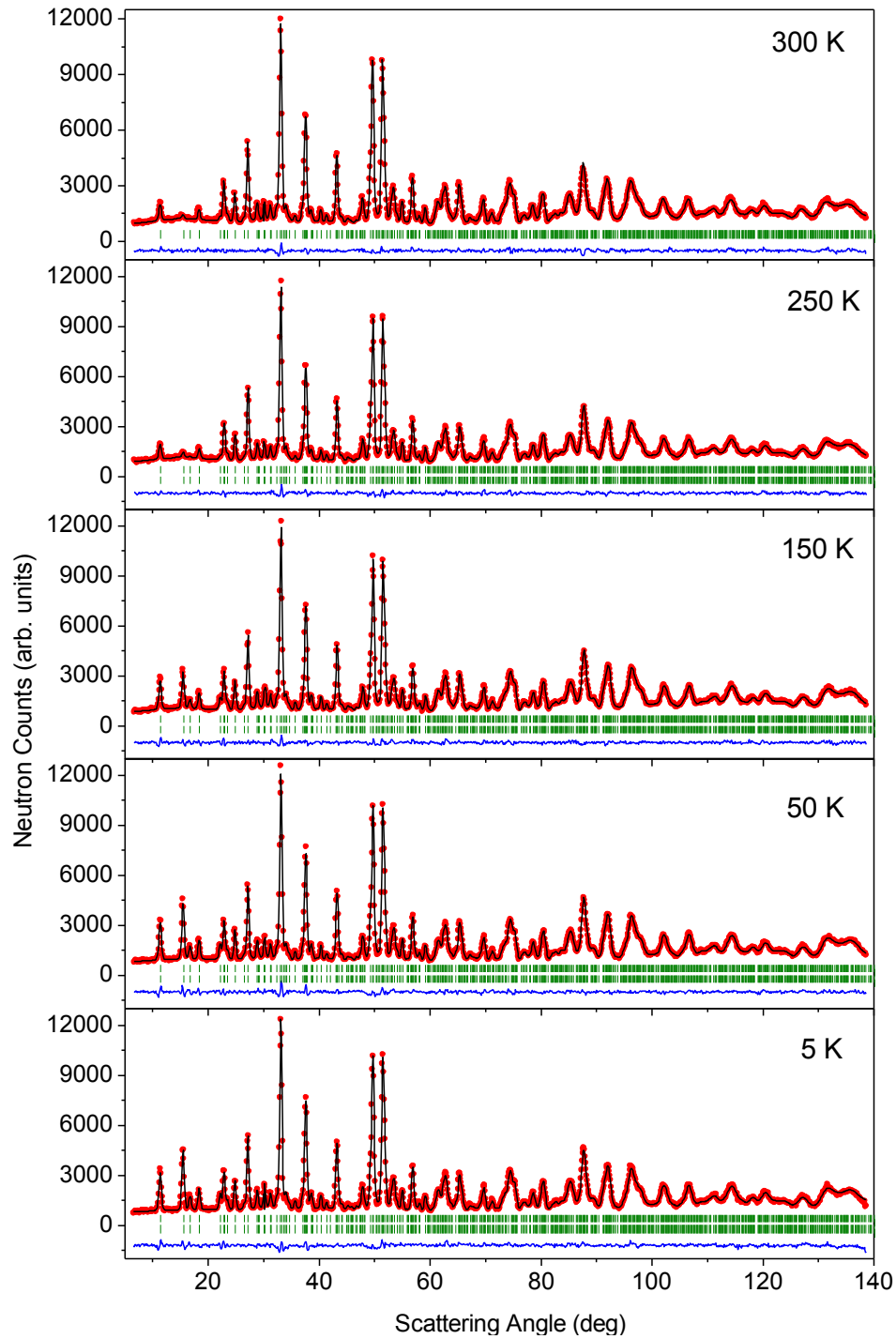


Fig. 2.5: Observed (red solid circles) and calculated (solid lines) neutron diffraction patterns of the AlFeO_3 at 300, 250, 150, 50, and 5 K. Solid line at the bottom in each panel shows the difference between observed and calculated patterns. Vertical lines show the position of Bragg peaks.

Under the space group $Pna2_1$, all atoms (both anions and cations) are in general position and thus the fractional atomic coordinates were varied during the refinement except for the z coordinate of the Al1 site. Here, the z value of the Al1 site was kept fixed at zero to define the origin of the unit cell. The isotropic thermal parameters and the occupancy factors of all cations were varied during the refinement. The occupancy factors of the oxygen atoms were kept fixed at 1.0 (fully occupied). The refined values of the relative occupations of the Fe and Al ions are given in Table II.

Table II**Atomic coordinates of $AlFeO_3$ at 300 K.**

300 K					
Space Group: $Pna2_1$ (Orthorhombic), $a = 4.9806(3)$ Å, $b = 8.5511(6)$ Å, and $c = 9.2403(6)$ Å					
Atoms	x/a	y/b	z/c	B_{iso}	Occ.
Fe1/Al	0.1876(6)	0.1502(4)	0.5827(9)	0.20(2)	0.83(2)/ 0.17(2)
Fe2/Al	0.6646(3)	0.0320(3)	0.7998(9)	0.38(3)	0.81(1) /0.19(1)
Al1/Fe	0.1686(2)	0.1545(3)	0.00000(0)	0.56(2)	0.85(1)/ 0.14(1)
Al2/Fe	0.8164(7)	0.1613(3)	0.3098(4)	0.56(4)	0.74(2)/ 0.26(2)
O1	0.8164(7)	0.1613(3)	0.3098(4)	0.53(5)	1.0
O2	0.9824(5)	0.3218(9)	0.4201(2)	0.53(3)	1.0
O3	0.5073(2)	0.4905(7)	0.4331(5)	0.80(2)	1.0
O4	0.6620(9)	0.0047(9)	0.2040(8)	0.50(1)	1.0
O5	0.1418(5)	0.1630(7)	0.1984(6)	0.66(2)	1.0
O6	0.8372(5)	0.1652(6)	0.6767(1)	0.50(3)	1.0
χ^2	2.13%				
R_p	5.49%				
R_{wp}	6.42%				
R_{exp}	4.40%				
R_{Bragg}	2.04%				

Table III

Bond lengths and bond angles for the AlFeO₃ sample at 300 K.

Site	Bond Length		Bond Angles	
	Fe1	Fe1-O1 ₁ [*]	2.337(11)	O1 ₂ -Fe1-O3
Fe1-O1 ₂ [*]		2.115(12)	O1 ₁ -Fe1-O5 ₂	158.2(8)
Fe1-O2		2.041(14)	O2-Fe1-O5 ₁	161.3(10)
Fe1-O3		1.890(11)		
Fe1-O5 ₁		1.954(11)		
Fe1-O5 ₂		1.950(11)		
Fe2	Fe2-O1	2.236(10)	O1-Fe2-O5	165.0(8)
	Fe2-O2	2.076(14)	O2-Fe2-O3	158.8(10)
	Fe2-O3	1.879(11)	O4-Fe2-O6	163.8(9)
	Fe2-O4	2.142(11)		
	Fe2-O5	1.824(11)		
	Fe2-O6	1.960(13)		
Al1	Al1-O2	1.767(15)	O2-Al1-O4	110.1(10)
	Al1-O4	1.840(10)	O2-Al1-O6 ₁	115.7(10)
	Al1-O6 ₁	1.743(14)	O2-Al1-O6 ₂	108.3(9)
	Al1-O6 ₂	1.780(14)	O4-Al1-O6 ₁	112.1(10)
			O4-Al1-O6 ₂	103.7(9)
			O6 ₁ -Al1-O6 ₂	106.0(10)

Al2	Al2-O1 ₁	1.900(14)	O1 ₁ -Al2-O3	179.0(10)
	Al2-O1 ₂	1.956(14)	O1 ₂ -Al2-O4 ₁	175.3(9)
	Al2-O2	1.972(16)	O2-Al2-O4 ₂	173.0(10)
	Al2-O3	1.827(14)		
	Al2-O4 ₁	1.920(13)		
	Al2-O4 ₂	2.018(14)		

* The equivalent oxygen atoms in a given polyhedra are labeled by suffix 1 and 2.

Table IV

Cation-oxygen-cation bond angles for different sites and the corresponding cation-cation distances for the AlFeO₃ sample.

Bond Angles		Cation-Cation Distance	
Fe1-O1 ₂ -Fe2	165.5(6)	Fe1-Fe2	4.539(6)
Fe1-O1 ₁ -Al2	162.3(9)	Fe1-Al2	4.018(8)
Fe1-O2-Al1	116.7(9)	Fe1-Al1	3.246(12)
Fe2-O2-Al1	117.6(8)	Fe2-Al1	3.291(11)
Al1-O2-Al2	119.0(10)	Al1-Al2	3.224(15)
Fe1-O3-Fe2	120.3(7)	Fe1-Fe2	3.269(10)
Fe1-O3-Al2	131.6(9)	Fe1-Al2	3.390(12)

Al1-O4-Al2	126.6(8)	Al1-Al2	3.359(12)
Al1-O4-Al2	120.4(8)	Al1-Al2	3.348(12)
Fe1-O5-Fe2	131.1(7)	Fe1-Fe2	3.439(10)
Fe1-O5-Fe2	127.1(7)	Fe1-Fe2	3.379(9)
Fe2-O6-Al1	123.2(8)	Fe2-Al1	3.258(11)
Fe2-O6-Al1	121.0(9)	Fe2-Al1	3.256(12)

Based on the diffraction data, the crystal and magnetic structures are drawn as shown in Fig. 2.6 and 2.7. The crystal structure of these compounds is made up of alternative layers of cations and oxygen ions along the crystallographic c direction. There are four different cation sites (Fe/Al) which are labeled as Fe1, Fe2, Al1 and Al2. The Fe1 and Fe2 sites are predominantly occupied by Fe ions, whereas, the Al1 and Al2 sites are predominantly occupied by Al ions. Fe1, Fe2, and Al2 sites being present in an octahedral environment and Al1 sites are in a tetrahedral environment (Fig. 2.6). The octahedra are connected to each other by the sharing of edges, whereas the tetrahedron shares oxygen ions at the corners. No edge sharing occurs between the octahedra and tetrahedra. There are eight formula units (40 atoms) per unit cell, in agreement with the earlier reports. The crystal structure remains same down to 5 K. From the derived values of bond lengths and bond angles, given in Table III, a distortion in (Fe/Al)O₆ octahedra

as well as AlIO_4 tetrahedra is evident. The observed distortion in the polyhedra is due to the large difference between ionic radii of Fe^{3+} (0.645 Å for coordination number VI) and Al^{3+} (0.535 Å for coordination number VI) along with the site disorder caused by Fe and Al mixed occupation [6].

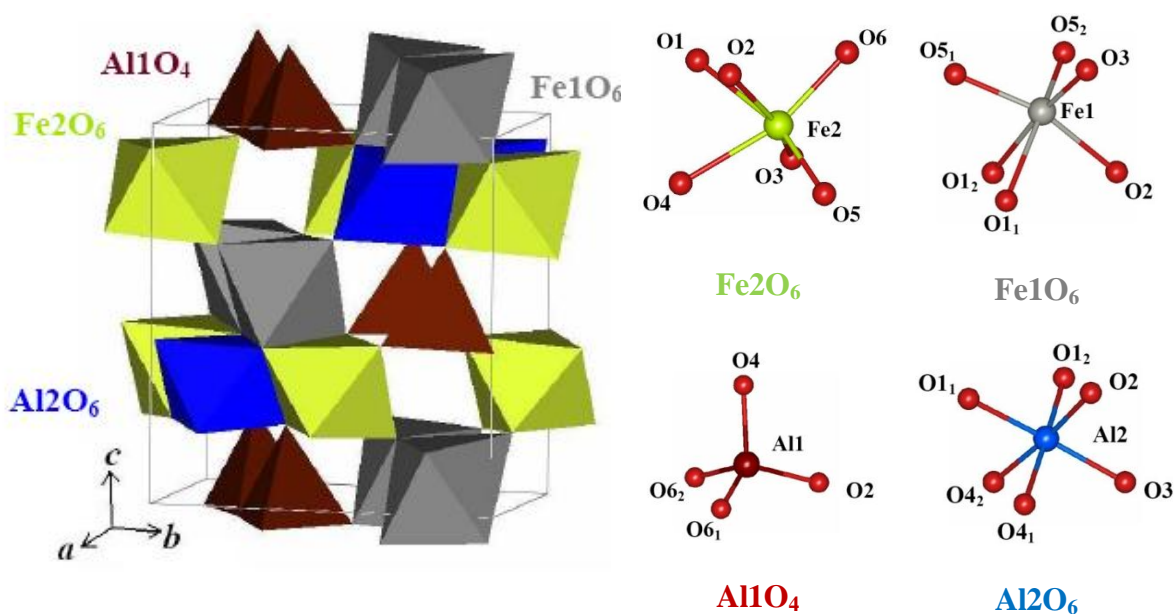


Fig. 2.6: The crystal structure (unit cell) of the AlFeO_3 . A schematic view of the $(\text{Fe}/\text{Al})\text{O}_6$ octahedra and AlIO_4 tetrahedra. The orientation of Fe_1 , Fe_2 , Al_1 , Al_2 polyhedra are shown as they appeared in the right part of the unit cell.

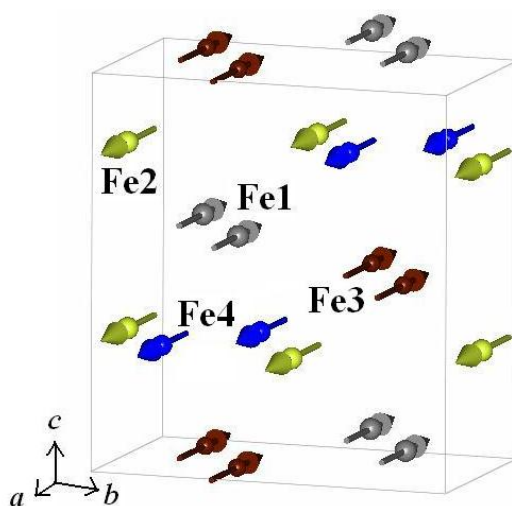


Fig. 2.7: The magnetic structure (unit cell) of the AlFeO_3 .

The magnetic structure is a collinear ferrimagnetic in nature with the ordered magnetic moment aligned along the crystallographic a direction. The site occupancies were found not to vary with lowering of temperature. Therefore, the values of the site occupancies as derived from the analysis of the diffraction pattern at 300 K (paramagnetic state) were used for the magnetic structure refinement. The averaged ordered magnetic moments are found to be 3.88(15), 3.64(14), 3.01(75), and 2.79(43) μ_B/Fe ion at Fe1, Fe2, Fe3 (A11), and Fe4 (A12) sites respectively. Here, the moments at Fe1 and Fe3 sites are parallel to each other and aligned antiparallel to the parallelly aligned moments at Fe2 and Fe4 sites.

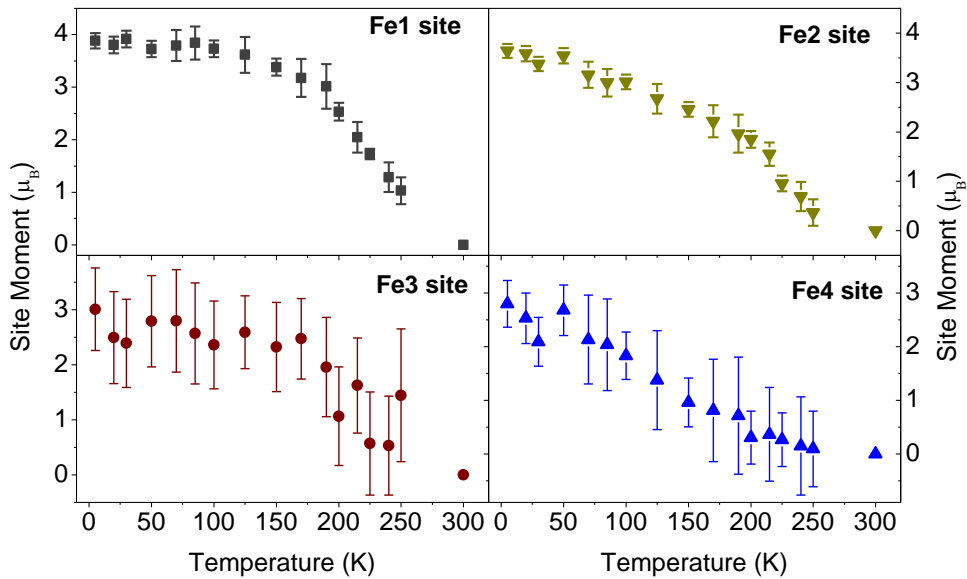


Fig. 2.8: The temperature dependence of the ordered site moments per Fe ion at Fe1, Fe2, Fe3 and Fe4 sites in AlFeO_3 .

In Fig. 2.8, the temperature dependence of the ordered site moments for all four cation sites are shown. The moments of the Fe1, Fe2 and Fe3 sites show almost a normal Brillouin function like temperature dependence. Whereas, a clear deviation from a normal Brillouin function temperature dependence has been observed for the ordered

moment of the Fe₄ site. The magnetic ordering temperature for all four sites is found to be ~ 270 K (T_N). Temperature dependence of the lattice parameters (subsequently, the unit cell volume), depicted in Fig. 2.9, shows a unique nature with a dip at $T \sim 150$ K. The expansion of the lattice at lower temperatures is a very uncommon and an interesting phenomenon of negative thermal expansion.

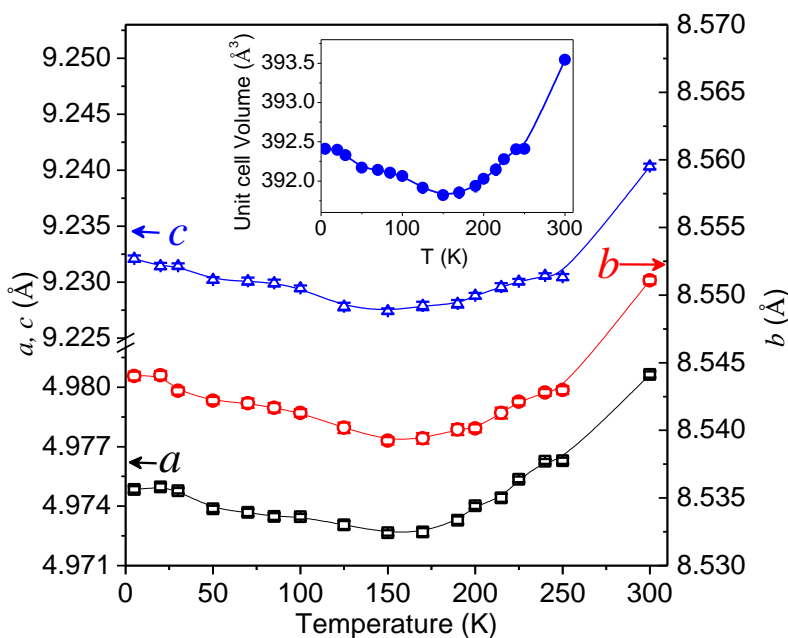


Fig. 2.9: The temperature dependence of lattice parameters of AlFeO_3 . Inset: The temperature dependence of the unit cell volume.

In the present compound, the magnetic ordering occurs due to the cation-oxygen-cation superexchange antiferromagnetic interactions where the strength of the interaction strongly depends on the bond angles and bond lengths. The exchange interaction is strongest for the 180° cation-oxygen-cation bond angle and weakens with the deviation of the bond angle from 180° . The $A\text{-O-A}'$ ($A, A' = \text{Fe/Al}$) bond angles which are greater than 115° and the corresponding cation-cation distances are given in Table IV. The

most important pathways for the superexchange antiferromagnetic interactions are Fe1-[O1/O3/O5]-Fe2 and Fe1-[O1/O3]-Al2 (26 at. % of the Al2 site is occupied by Fe ions). In all other cases, the Al1 site is involved which is less populated by Fe ions (~ 14 at. %). The temperature dependence of Fe1-O5-Fe2 bond angles (a representative case) and corresponding Fe1-Fe2 distances are shown in Fig. 2.10. Interestingly, the Fe1-O5₁-Fe2 bond angle starts to decrease below ~ 150 K, where a volume expansion has been observed [Fig. 2.9]. Whereas, the Fe1-O5₂-Fe2 bond angle starts increasing below this temperature. Besides, an anomaly in the Fe1-Fe2 distances around the same temperature has been found.

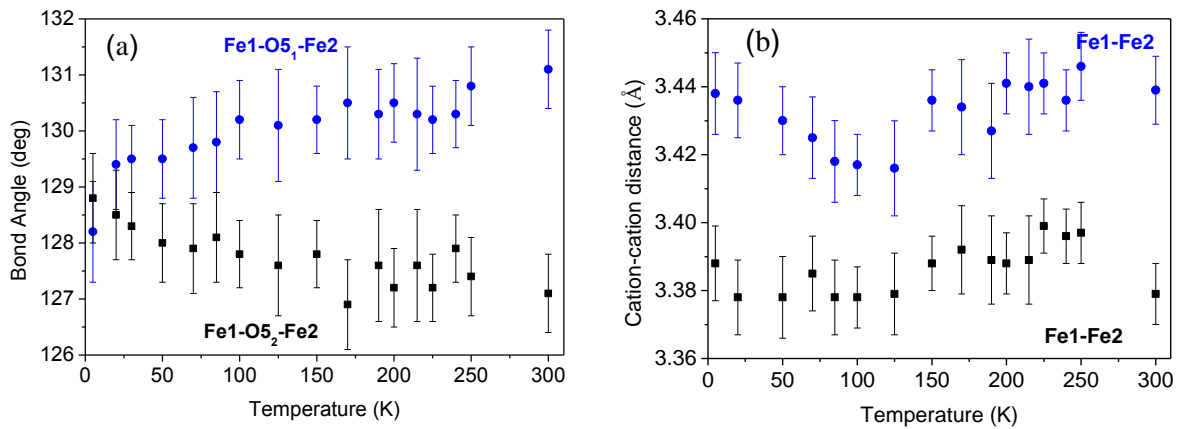


Fig. 2.10: (a) The temperature dependence of Fe1-O5-Fe2 bond angles of AlFeO₃ and (b) Corresponding Fe1-Fe2 distances as a function of temperature of AlFeO₃.

To study the crystal structure in further details, the distortion in the polyhedral has been calculated in the following way. The distortion parameter (Δ) of a coordination

polyhedron AO_N (A: Fe1, Fe2, Al1, and Al2) with an average value of the A-O bond length $\langle d \rangle$, is defined as:

$$\Delta = (1/N) \sum_1^N \{(d_N - \langle d \rangle) / \langle d \rangle\}^2$$

The temperature dependent values of Δ for all three octahedral and Al2 tetrahedral sites are shown in Fig. 2.11. The $Al1O_4$ tetrahedra are almost regular in nature. The octahedral environment of both Fe1 and Fe2 sites is highly distorted. For the other octahedral site ($Al2O_6$), a relatively less distortion has been observed; however, the temperature dependence Δ shows a peak at around $T \sim 150$ K. This may be correlated with the observed temperature dependence of unit cell volume which is a mirror image of the Δ versus T curve (Fig. 2.9).

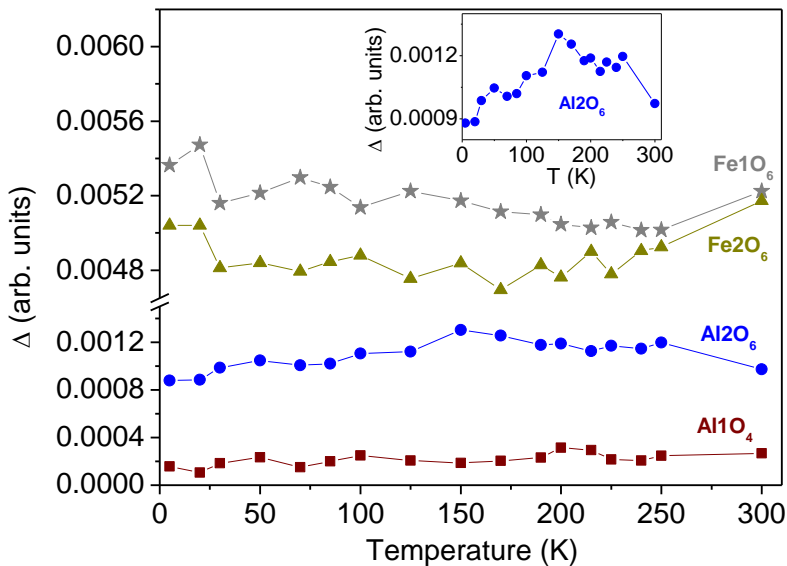


Fig. 2.11: The distortion parameter (Δ) as a function of temperature for Fe/Al polyhedral in $AlFeO_3$. An enlarged view of the temperature dependence of Δ for $Al2O_6$ octahedra is shown in inset.

(c) Neutron diffraction results of GaFeO₃

Neutron diffraction study followed by Rietveld refined pattern reveals that GaFeO₃ also crystallizes in chiral non-centrosymmetric space group $Pna2_1$. In Fig. 2.12 neutron diffraction patterns of GaFeO₃ at 300 and 5 K are shown.

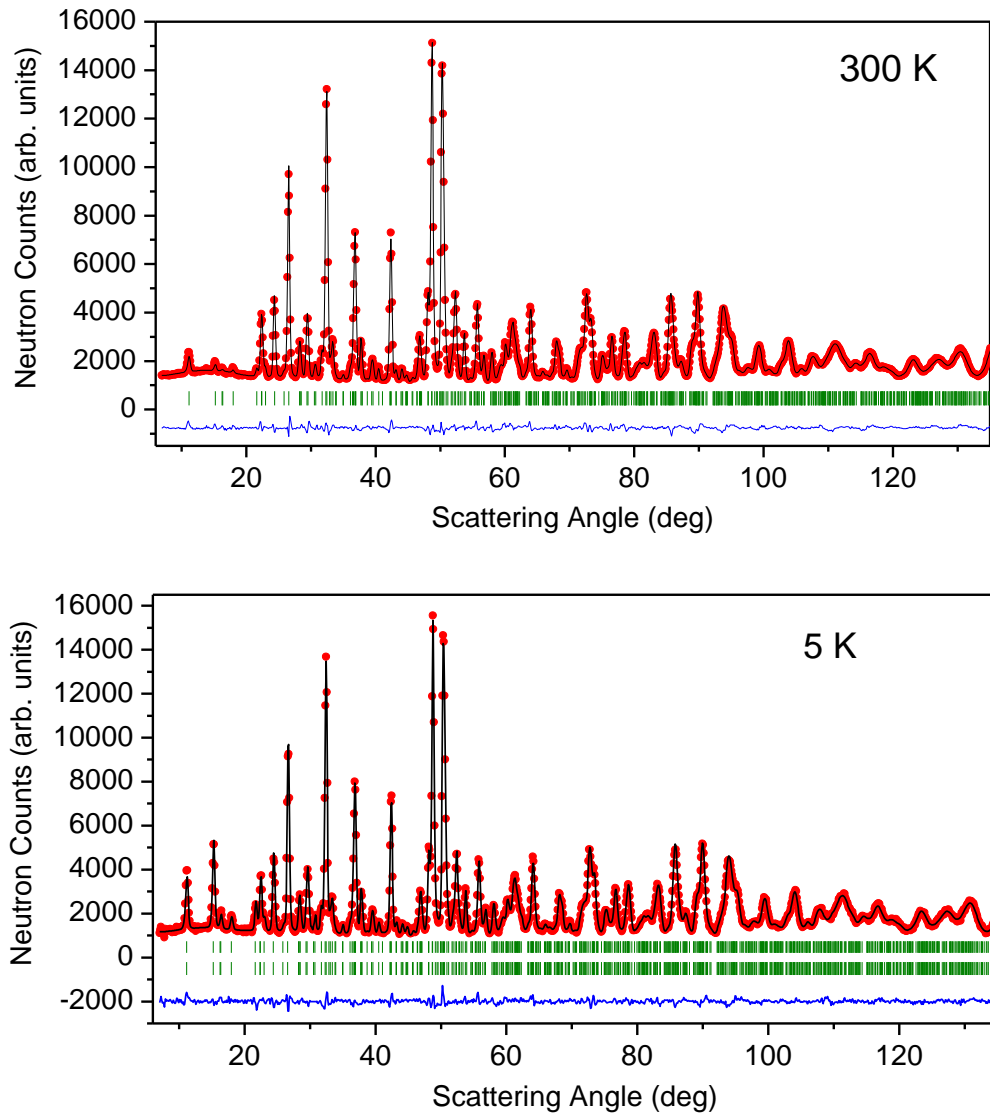


Fig. 2.12: Observed (red solid circles) and calculated (solid lines) neutron diffraction patterns of the GaFeO₃ at 300 and 5 K. Solid line at the bottom in each panel shows the difference between observed and calculated patterns. Vertical lines show the position of Bragg peaks.

In both AlFeO_3 and GaFeO_3 , at lower temperatures, an increase in the intensity of the fundamental (nuclear) Bragg peaks at lower scattering angles suggest a ferromagnetic or ferrimagnetic ordering (Figs. 2.5 & 2.12). The refined lattice parameters and other structural parameters are given in Table V (300 K) and Table VI (5 K). In the Rietveld refinement, the coherent nuclear scattering lengths of 0.9450×10^{-12} , 0.7288×10^{-12} , and 0.5803×10^{-12} cm for Fe, Ga and O, respectively, have been used.

Table V

Atomic coordinates of GaFeO_3 at 300 K.

300 K					
Space Group: $Pna2_1$ (Orthorhombic), $a = 5.0814(2)$ Å, $b = 8.7436(3)$ Å, and $c = 9.391(2)$ Å					
Atoms	x/a	y/b	z/c	B_{iso}	Occ.
Fe1/Ga	0.1895(5)	0.1531(5)	0.5842(4)	0.21(3)	0.65(2)/ 0.35(2)
Fe2/Ga	0.6705(9)	0.0327(4)	0.7995(6)	0.64(2)	0.70(1) /0.30(1)
Ga1/Fe	0.1755(2)	0.1491(5)	0	0.36(4)	0.91(3)/ 0.09(3)
Ga2/Fe	0.8053(8)	0.1575(7)	0.3073(6)	0.40(1)	0.46(1)/ 0.54(1)
O1	0.9771(9)	0.3269(7)	0.4230(6)	0.87(5)	1.0
O2	0.5171(4)	0.4921(9)	0.4403(5)	0.84(3)	1.0
O3	0.6538(9)	-0.0009(8)	0.2005(9)	0.60(4)	1.0
O4	0.1492(8)	0.1605(8)	0.1957(5)	0.68(5)	1.0
O5	0.8401(7)	0.1744(7)	0.6688(7)	0.58(3)	1.0
O6	0.5093(3)	0.1676(10)	0.9405(8)	0.65(4)	1.0
χ^2	2.3%				
R_p	4.93%				
R_{wp}	5.76%				
R_{exp}	3.80%				
R_{Bragg}	2.74%				

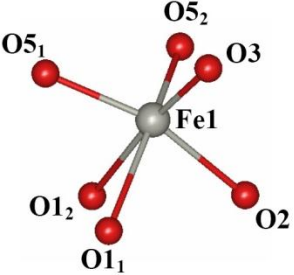
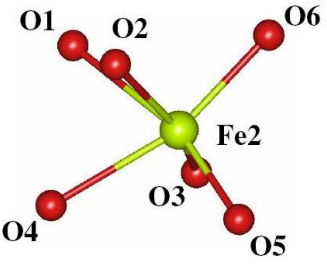
Table VI

Atomic coordinates of GaFeO₃ at 5 K.

5 K					
Space Group: $Pna2_1$ (Orthorhombic), $a = 5.0814(2)$ Å, $b = 8.7436(3)$ Å, and $c = 9.391(2)$ Å					
Atoms	x/a	y/b	z/c	B_{iso}	Occ.
Fe1/Ga	0.1931(2)	0.1537(6)	0.5850(5)	0.05(3)	0.65(2)/0.35(2)
Fe2/Ga	0.6741(1)	0.0308(5)	0.7987(8)	0.48(1)	0.70(1)/0.30(1)
Ga1/Fe	0.1821(8)	0.1479(8)	0	0.10(2)	0.91(3)/0.09(3)
Ga2/Fe	0.8138(3)	0.1586(6)	0.3084(7)	0.14(4)	0.46(1)/0.54(1)
O1	0.9764(2)	0.3266(5)	0.4256(9)	0.61(5)	1.0
O2	0.5187(9)	0.4906(6)	0.4376(4)	0.59(2)	1.0
O3	0.6508(8)	0.0007(6)	0.2025(1)	0.45(3)	1.0
O4	0.1550(9)	0.1630(1)	0.1976(3)	0.42(4)	1.0
O5	0.8448(8)	0.1716(1)	0.6719(4)	0.31(2)	1.0
O6	0.5113(2)	0.1655(3)	0.9412(2)	0.49(3)	1.0
μ_{Fe1}	-4.41(25)				
μ_{Fe2}	3.45(22)				
μ_{Fe3}	-2.81(77)				
μ_{Fe4}	2.99(52)				
χ^2	3.57%				
R_p	5.61%				
R_{wp}	6.67%				
R_{exp}	3.53%				
R_{Bragg}	2.5%				
R_{Mag}	6.92%				

The site occupancies were found not to vary with lowering of temperature. Therefore, the values of the site occupancies as derived from the analysis of the diffraction pattern at 300 K (paramagnetic state) were used for the magnetic structure refinement.

Table VII: Bond lengths & Bond Angles of GaFeO₃ (300 K)

Site	Bond Length		Bond Angles	
<p style="text-align: center;">Fe1</p> 	Fe1-O1 ₁	2.401(9)	O1 ₂ -Fe1-O3	174.7(7)
	Fe1-O1 ₂	2.112(9)	O1 ₁ -Fe1-O5 ₂	155.9(7)
	Fe1-O2	2.051(10)	O2-Fe1-O5 ₁	162.8(7)
	Fe1-O3	1.897(9)		
	Fe1-O5 ₁	1.954(10)		
	Fe1-O5 ₂	1.868(9)		
<p style="text-align: center;">Fe2</p> 	Fe2-O1	2.268(9)	O1-Fe2-O5	167.0(7)
	Fe2-O2	2.097(10)	O2-Fe2-O3	159.2(8)
	Fe2-O3	1.913(9)	O4-Fe2-O6	163.4(7)
	Fe2-O4	2.155(9)		
	Fe2-O5	1.945(9)		
	Fe2-O6	1.954(10)		

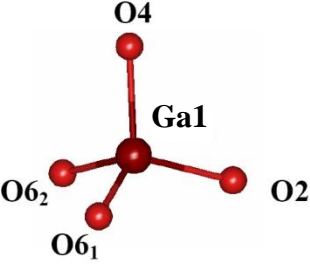
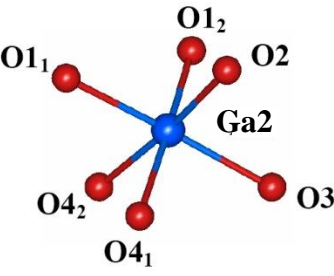
Site	Bond Length		Bond Angles	
<p style="text-align: center;">Ga1</p> 	Ga1-O2	1.776(9)	O2-Ga1-O4	108.4(7)
	Ga1-O4	1.845(6)	O2-Ga1-O6 ₁	119.5(8)
	Ga1-O6 ₁	1.793(11)	O2-Ga1-O6 ₂	108.3(7)
	Ga1-O6 ₂	1.894(10)	O4-Ga1-O6 ₁	111.9(7)
			O4-Ga1-O6 ₂	102.5(6)
			O6 ₁ -Ga1-O6 ₂	104.7(8)
<p style="text-align: center;">Ga2</p> 	Ga2-O1 ₁	2.034(9)	O1 ₁ -Ga2-O3	178.7(7)
	Ga2-O1 ₂	1.994(10)	O1 ₂ -Ga2-O4 ₁	175.0(7)
	Ga2-O2	2.106(10)	O2-Ga2-O4 ₂	167.8(7)
	Ga2-O3	1.876(9)		
	Ga2-O4 ₁	2.039(9)		
	Ga2-O4 ₂	2.064(9)		

Table VIII

Cation-oxygen-cation bond angles for different sites and the corresponding cation-cation distances for GaFeO₃ sample.

Bond Angles			Cation-Cation Distance	
Fe1-O1 ₂ -Fe2	166.7(5)		Fe1-Fe2	4.637(7)
Fe1-O1 ₁ -Ga2	164.5(6)		Fe1-Ga2	4.068(7)
Fe1-O2-Ga1	120.5(5)		Fe1-Ga1	3.325(7)
Fe2-O2-Ga1	119.0(5)		Fe2-Ga1	3.342(7)
Ga1-O2-Ga2	112.7(5)		Ga1-Ga2	3.237(6)
Fe1-O3-Fe2	122.6(6)		Fe1-Fe2	3.342(7)
Fe1-O3-Ga2	130.9(5)		Fe1-Ga2	3.432(7)
Ga1-O4-Ga2	121.3(4)		Ga1-Ga2	3.409(6)
Ga1-O4-Ga2	125.0(4)		Ga1-Ga2	3.446(6)
Fe1-O5-Fe2	126.8(5)		Fe1-Fe2	3.486(7)
Fe1-O5-Fe2	127.0(5)		Fe1-Fe2	3.412(7)
Fe2-O6-Ga1	123.6(6)		Fe2-Ga1	3.303(7)
Fe2-O6-Ga1	121.6(5)		Fe2-Ga1	3.359(6)

GaFeO_3 has a structure similar to that of AlFeO_3 with a non-centrosymmetric space group. In GaFeO_3 , there are four different cation sites Fe1, Fe2, Ga1 and Ga2, of which Fe1, Fe2 and Ga2 have an octahedral oxygen environment. The cation in the Ga1 site is in the tetrahedral oxygen environment. The crystal structure of this compound is made up of alternative layers of cations and oxygen ions along the crystallographic c direction. The octahedra are connected to each other by the sharing of edges, whereas the tetrahedron shares oxygen ions at the corners. No edge sharing occurs between the octahedra and tetrahedra. There are eight formula units (40 atoms) per unit cell and the crystal structure remains same down to 5 K.

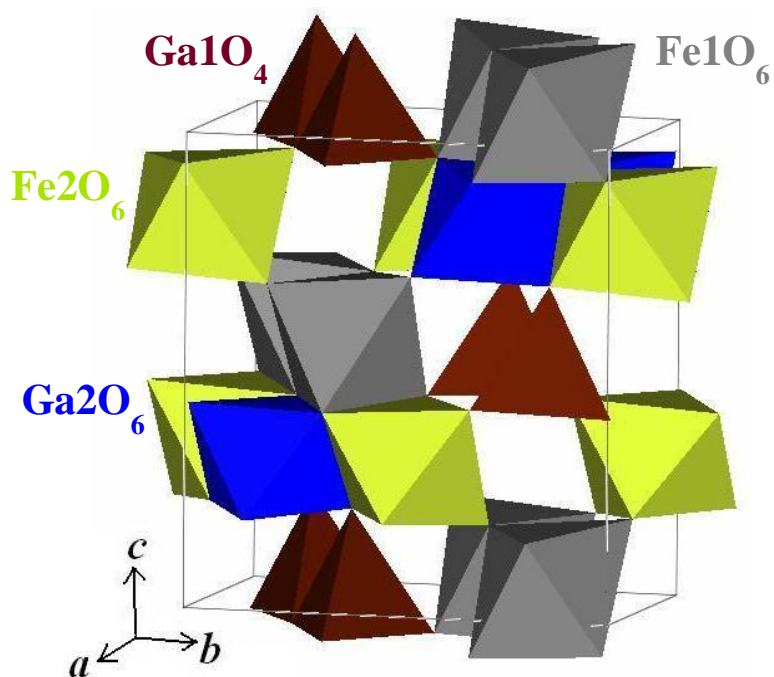


Fig. 2.13: The crystal structure (unit cell) of the GaFeO_3 .

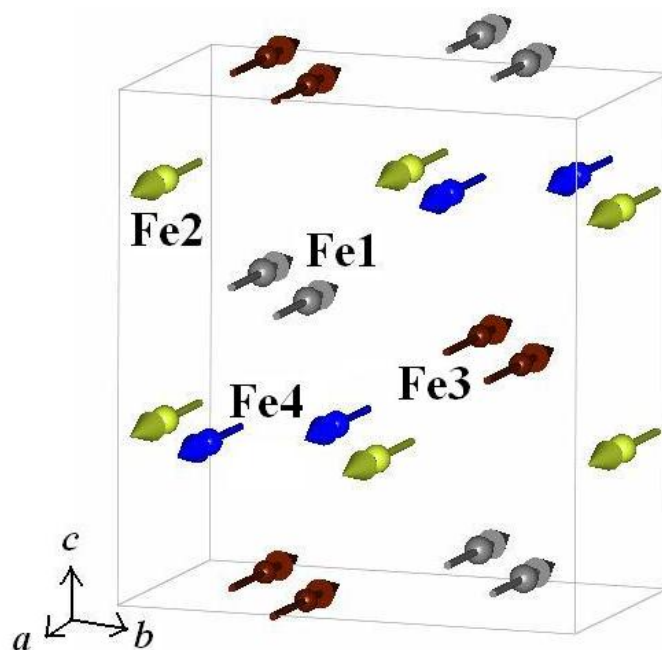


Fig. 2.14: The magnetic structure (unit cell) of the GaFeO_3 .

The magnetic unit cell dimension of GaFeO_3 is the same as the chemical (nuclear) one (Figs. 2.13 and 2.14). The magnetic structure is collinear ferrimagnetic with the ordered magnetic moment aligned along the crystallographic a direction. The Néel sublattices are $A = \text{Fe1} + \text{Ga1}$ and $B = \text{Fe2} + \text{Ga2}$. Here, the moments at Fe1 and Fe3 (Ga1) sites are parallel to each other and aligned antiparallel to the parallelly aligned moments at Fe2 and Fe4 (Ga2) sites. In Fig. 2.15 the temperature dependence of the ordered site moments for all four cation sites are shown.

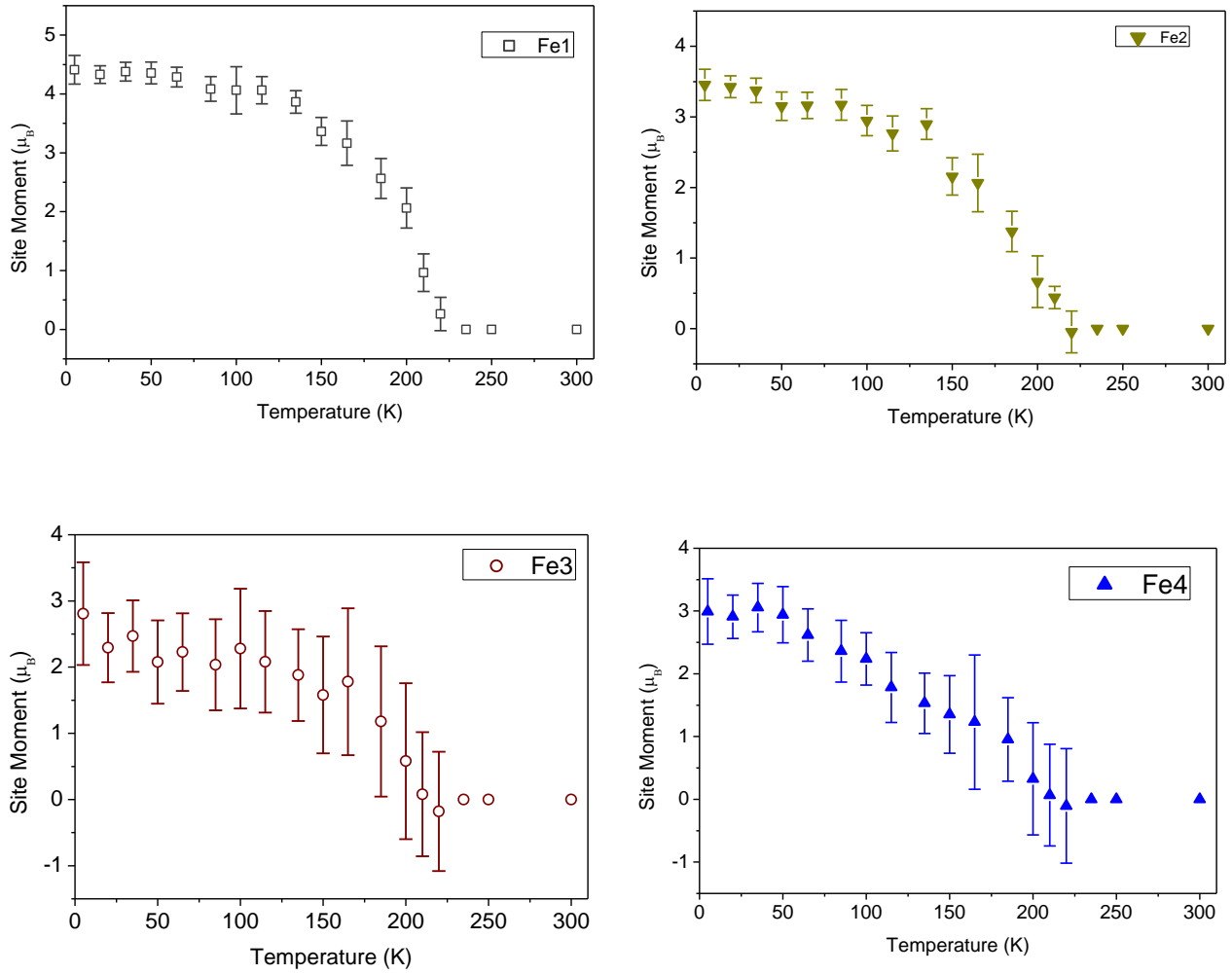


Fig. 2.15: The temperature dependence of the ordered site moments per Fe ion at Fe1, Fe2, Fe3 and Fe4 sites in GaFeO_3 .

Temperature dependence of the lattice parameters (subsequently, the unit cell volume), depicted in Fig. 2.16, shows a unique nature with a dip at $T \sim 150$ K. The expansion of the lattice at lower temperatures is a very uncommon and an interesting phenomenon of negative thermal expansion.

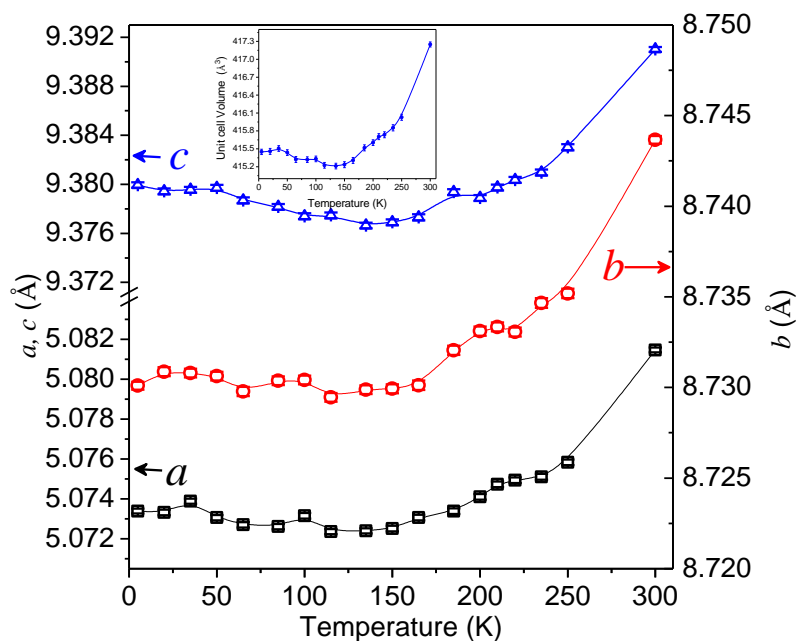


Fig. 2.16: The temperature dependence of lattice parameters of GaFeO₃. Inset: The temperature dependence of the unit cell volume.

The temperature dependent values of Δ for all three octahedral and Ga₂ tetrahedral sites are shown in Fig. 2.17.

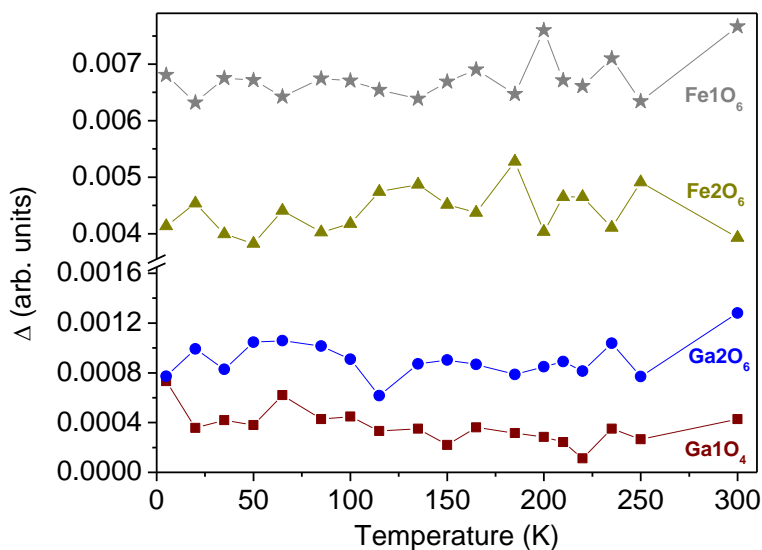


Fig. 2.17: The distortion parameter (Δ) as a function of temperature for Fe/Ga polyhedral in GaFeO₃.

The octahedral environment of both Fe1 and Fe2 sites is highly distorted while the other octahedral site (Ga_2O_6), is relatively less distorted (Tables VII & VIII). The temperature dependence of Δ was found to be negligible for the Ga_1O_4 tetrahedron. More importantly, it was found that (Fe/Ga) polyhedra are more distorted in comparison with (Fe/Al) polyhedra, which could be due to larger amount of site disorder associated with relatively better size matching between Fe^{+3} and Ga^{+3} .

The unit cell volume of $\text{Al}_{1-x}\text{Ga}_x\text{FeO}_3$ ($x = 0, 1$) compounds have been found to show a significant temperature dependence with a change in slope around 150 K, the increase in the parameters becoming even more marked in the 200-250 K range (Fig. 2.18). It is noteworthy that the T_N values of $\text{Al}_{1-x}\text{Ga}_x\text{FeO}_3$ are in the 200-250 K range as will be seen later.

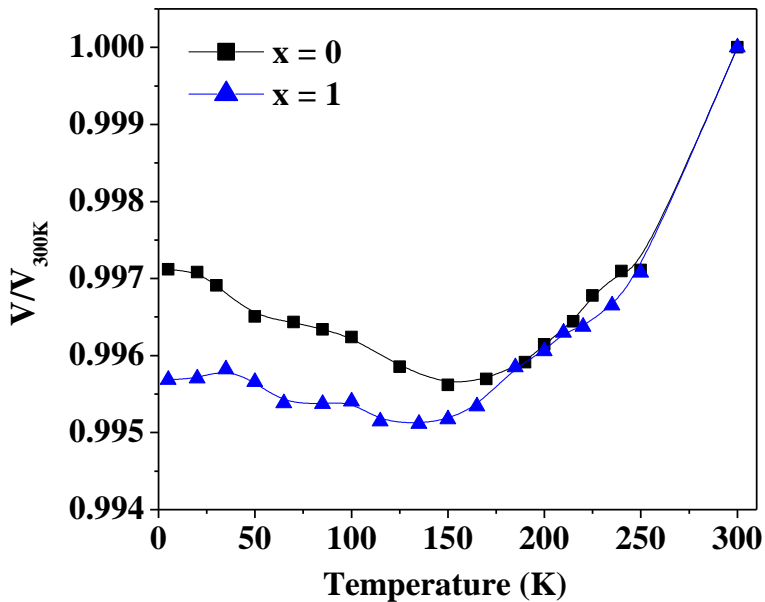


Fig. 2.18: Relative change in unit cell volumes of $\text{Al}_{1-x}\text{Ga}_x\text{FeO}_3$ ($x = 0, 1$) as a function of temperature.

Magnetic ordering in GaFeO_3 is antiferromagnetic in nature and it strongly depends on bond angle and bond length. Temperature dependence of magnetically important structural parameters ($A\text{-O-A}'$ angle; $A\text{-A}'$ bond and $A\text{-O}$ bond) are shown below.

Case 1:

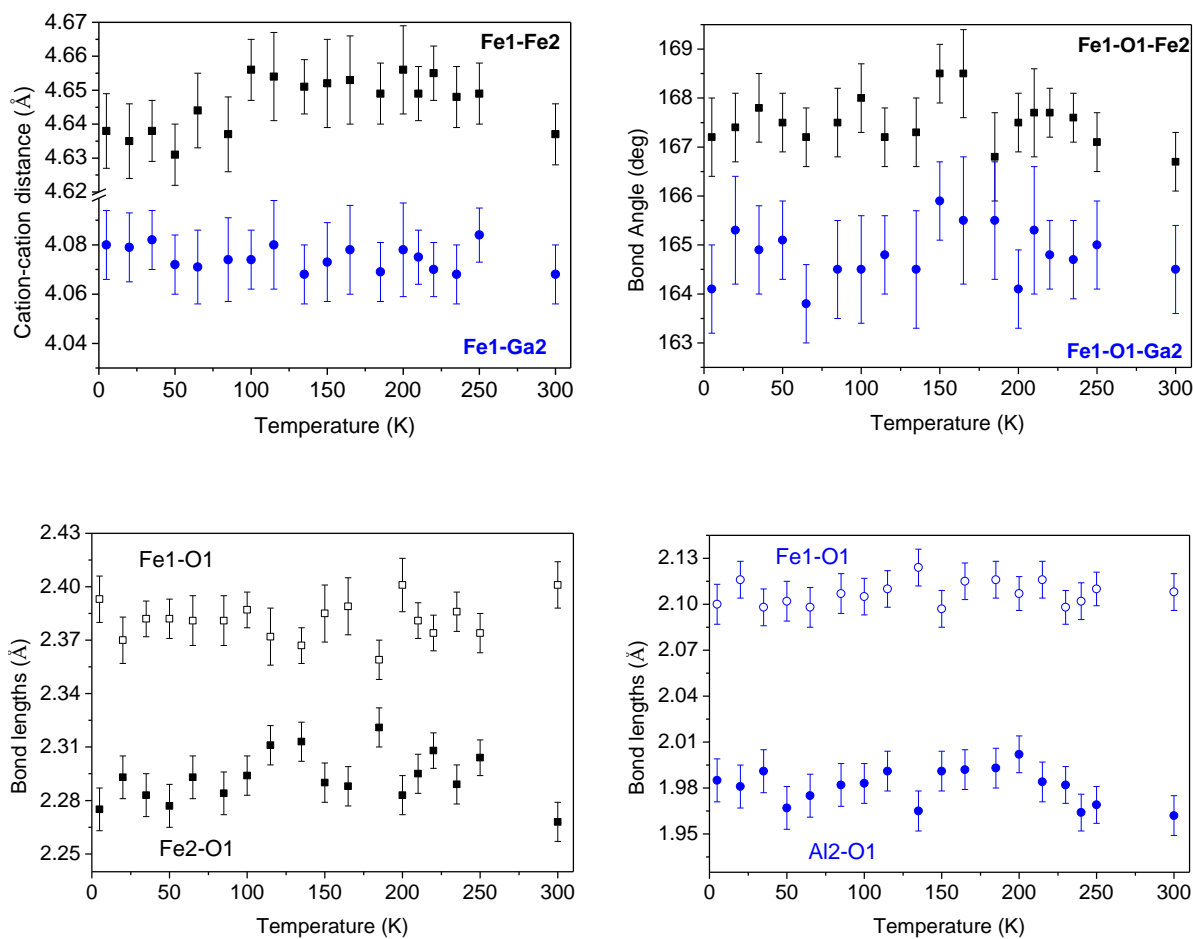


Fig. 2.19: Cations at the Fe1, Fe2, and Ga2 sites are connected via O1 ions in GaFeO_3 ; bond lengths ($A\text{-O1}$ and $A'\text{-O1}$) and bond angles ($A\text{-O1-A}'$) (where, $A, A' = \text{Fe1, Fe2, and Ga2}$ sites).

Case 2:

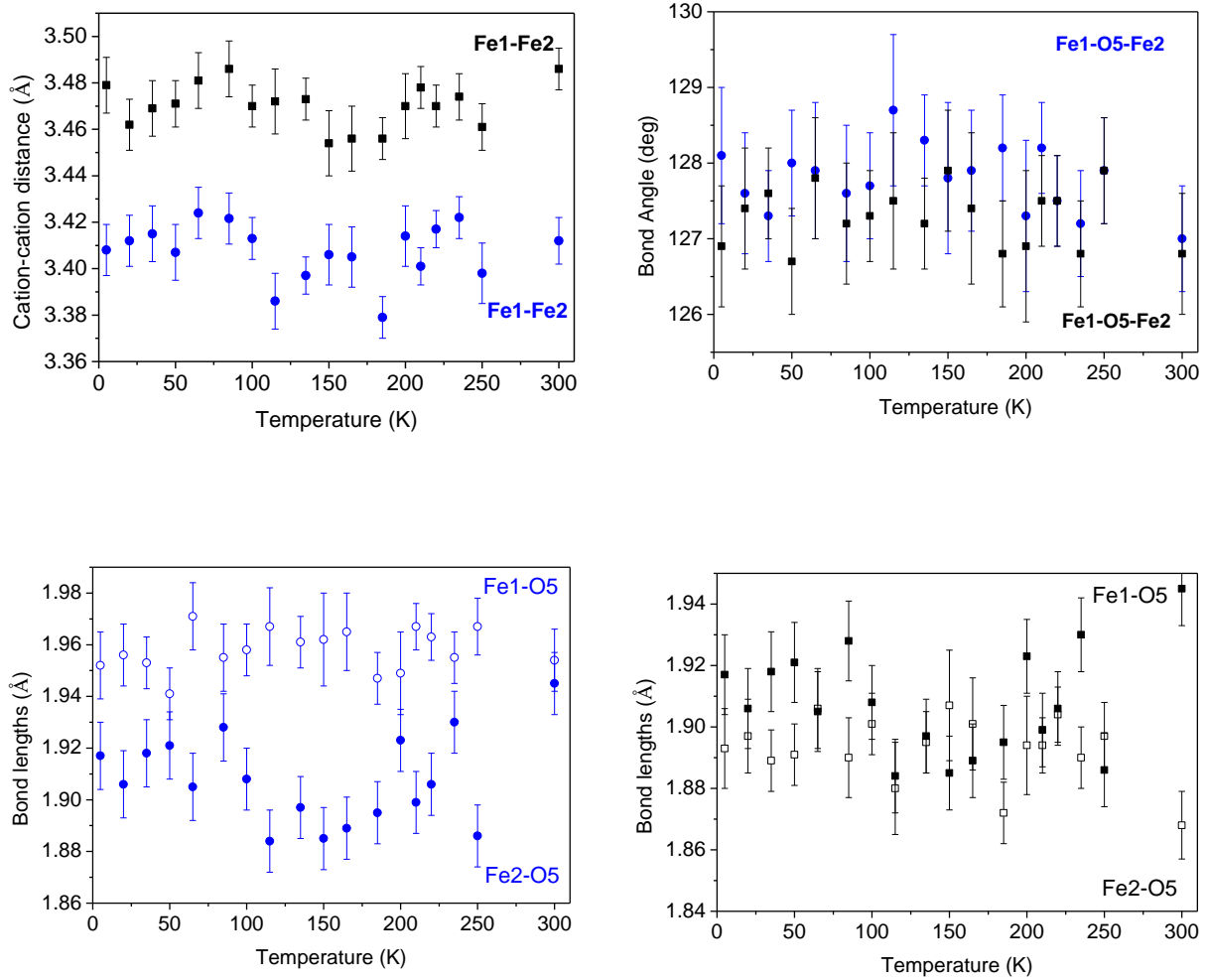


Fig. 2.20: Cations at the Fe1, and Fe2 sites connected via O5 ions in GaFeO₃; bond lengths (Fe1-O5 and Fe2-O5) and bond angles (Fe1-O5-Fe2).

Case 3:

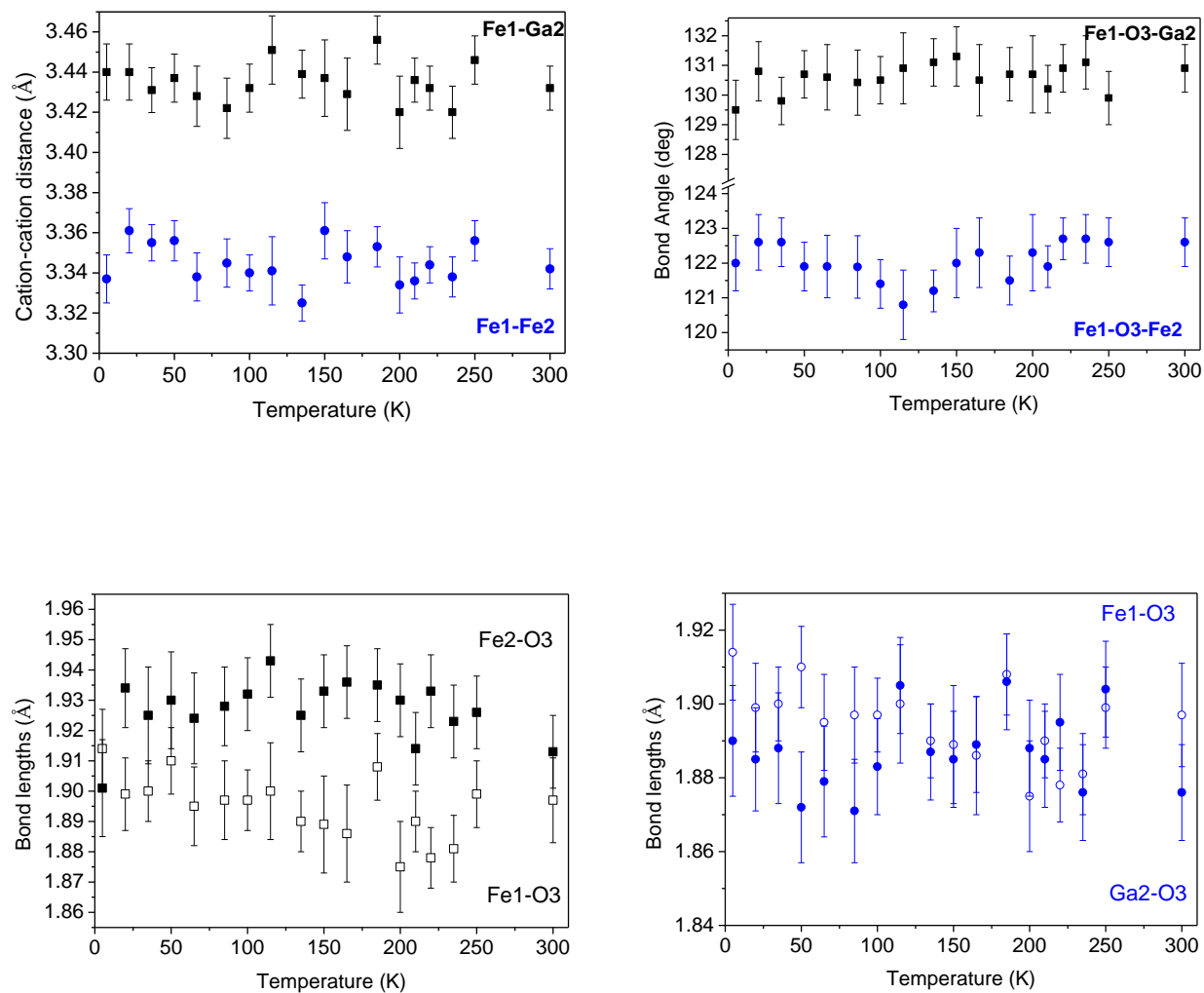


Fig. 2.21: Cations at the Fe1, Fe2, and Ga2 sites connected via O3 ions in GaFeO₃; bond lengths (A-O3 and A'-O3) and bond angles (A-O3-A') (where, A, A' = Fe1, Fe2, and Ga2 sites)

2.4.2 Magnetic Properties of AlFeO_3 and GaFeO_3 :

AlFeO_3 is ferrimagnetic with a T_N of 250 K, while GaFeO_3 exhibits a ferrimagnetic T_N of 210 K as shown in Fig. 2.22. Magnetic hysteresis was observed at low temperatures (see insets of Fig. 2.22). The value of saturation magnetization, remanant magnetization, and coercive field in the case of AlFeO_3 (GaFeO_3) are 13.9 (19.9) emu/g, 7.9 (10.1) emu/g and 12.9 (7.7) kOe respectively. Thus, both magnetic ordering and unit cell parameters vary systematically with the cation size or Ga content. Both the compounds show divergence between the zero-field cooled and field-cooled magnetisation data. Ferrimagnetic magnetization of $\text{Al}_{1-x}\text{Ga}_x\text{FeO}_3$ ($x = 0, 1$) mainly originates from the difference in Fe occupation at the four inequivalent cation sites. Low temperature magnetic ordering in these oxides is due to the cation-oxygen-cation superexchange antiferromagnetic interaction.

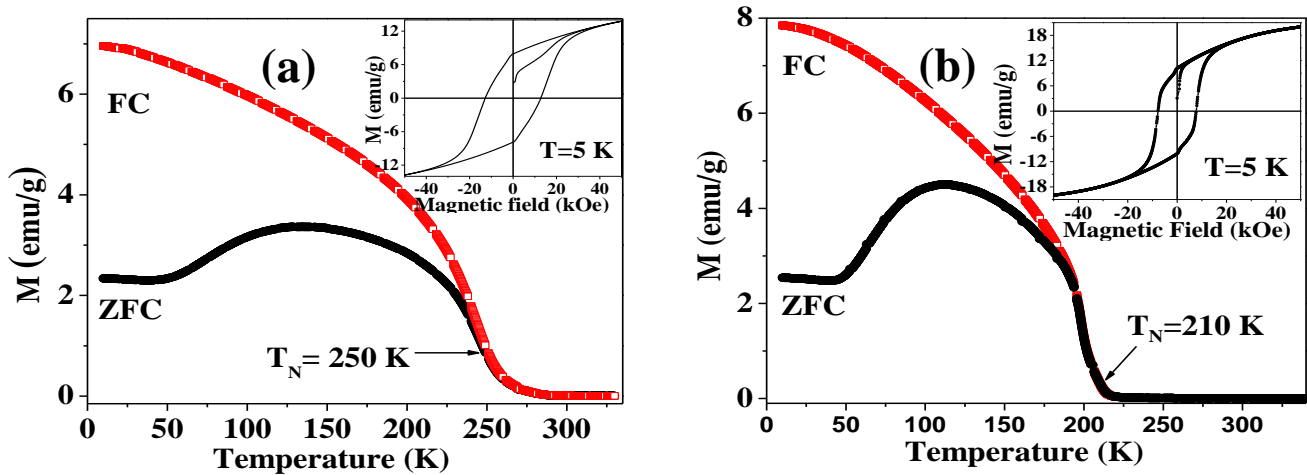


Fig. 2.22: Temperature dependent magnetization of (a) AlFeO_3 and (b) GaFeO_3 under field-cooled (FC) and zero-field-cooled (ZFC) conditions. Magnetic hysteresis at 5 K is shown in the inset.

Mössbauer spectra of both oxides were recorded by Dr. Y. Sundarayya at 300 K, appear as doublets. An analysis of this doublet reveals the paramagnetic nature of the randomly oriented Fe^{3+} ions with no exchange interactions. The isomer shift values obtained for this doublet also confirms the presence of iron in ferric state. To ascertain the distribution of Fe at different cation sites, Mossbauer spectra were recorded on the samples at low temperatures using a helium close cycle cooler system attached to the sample chamber. In Fig. 2.23, we show the Mössbauer spectra of AlFeO_3 and GaFeO_3 at 10 K. The spectra were analysed using the WinNormos-for-Igor Mössbauer spectra fitting software sold by WissEl GmbH, Starnberg, Germany. The hyperfine parameters were obtained by fitting theoretical subspectral curves to experimental data with Lorentzian line shapes to deconvolute Fe sites in the spectra. The areas of the lines in the hyperfine spectra were constrained to be in the ratio 3:2:1:1:2:3. In Table IX we give the refined parameters. The isomer shifts obtained at 10 K are found to be 0.2–0.35 mm/s relative to α -iron for the three samples, consistent with the ferric state in oxide materials [12-14].

The site occupancies of the three octahedral sites Fe1, Fe2, (Al/Ga)2 and one tetrahedral site (Al/Ga)1 were determined from the respective areas of different Fe sites by the method described in the literature [15]. From this analysis, the Fe site occupancies of the Fe1, Fe2, A2 and A1 sites in AlFeO_3 are found to be 50, 26, 17 and 7 respectively. The Fe site occupancy values for GaFeO_3 are respectively 50, 23, 17, 10. The magnetic hyperfine field values in these oxides correspond to the ferric state and the hyperfine fields at the Fe1, Fe2, (Al/Ga)2, and (Al/Ga)1 sites decreases with the Ga content in $\text{Al}_{1-x}\text{Ga}_x\text{FeO}_3$ ($x = 0, 1$).

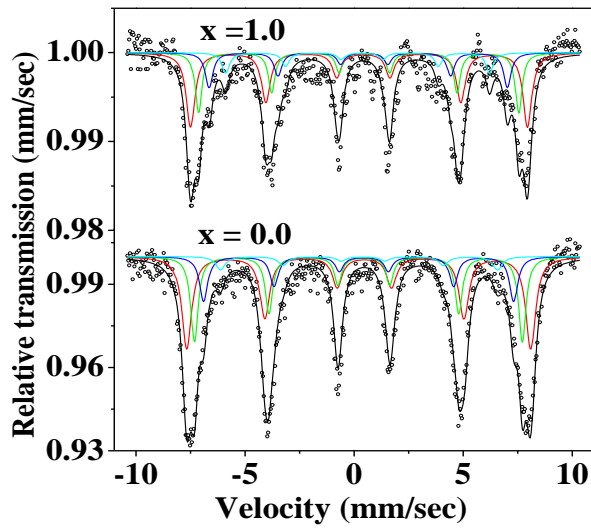


Fig. 2.23: Mössbauer spectra of $\text{Al}_{1-x}\text{Ga}_x\text{FeO}_3$ ($x = 0, 1$) at 10K.

Table IX

Mössbauer parameters for $\text{Al}_{1-x}\text{Ga}_x\text{FeO}_3$ system at 10K

Compound formula	Site	δ (mm/sec)	ΔE_Q (mm/sec)	B_{hf} (kOe)	Fe Occupancy (%)
AlFeO_3	Fe1	0.340(3)	-0.257(5)	489(1)	50
	Fe2	0.321(4)	-0.252(7)	466(1)	26
	Al2	0.326(7)	-0.24(1)	441(1)	17
	Al1	0.32(2)	-0.19(4)	394(1)	7
GaFeO_3	Fe1	0.32(1)	-0.20(3)	479(1)	50
	Fe2	0.339(7)	-0.26(3)	455(1)	23
	Ga2	0.33(2)	-0.28(5)	424(2)	17
	Ga1	0.25(2)	-0.20(7)	375(1)	10

Disorder, magnetic ordering and stability of AlFeO_3 have been studied theoretically by Prof. U. V. Waghmare *et al.* and the main results are shown below. Cation site disorder here means occupation of Fe site by an Al cation or vice versa, arising from an interchange of Al and Fe atoms in the perfectly ordered structure. From the observed data of occupancies of cation sites (Table II) at low temperature, disorder arises with highest probability through interchange in the positions of Fe and Al cations at Fe2 and Al2 sites.

(1) From the energies of the ferromagnetically and antiferromagnetically ordered states of AlFeO_3 (Table X), it becomes clear that the antiferromagnetic state (AFM) is more stable than the ferromagnetic (FM) one in the chemically ordered case. Magnetic moments of the various Fe ions change significantly (Table XI) with change in their ordering, resulting in Fe^{3+} in the low-spin state in the FM-ordered state. As the low-spin state of Fe^{3+} is known to be rare in nature, FM state of AlFeO_3 is indeed much higher in energy than the AFM one.

Table X

Energetics of magnetic configuration in AlFeO_3

order/ disorder	Total energy of magnetic configuration (eV)		
	$\text{AlFeO}_3\text{-FM}$	$\text{AlFeO}_3\text{-AFM}$	$\text{GaFeO}_3\text{-AFM}$
ordered	-297.02	-300.67	-270.75
disordered	-298.59	-300.09	-270.64

Table XI**Magnetic moments of individual Fe ions (μ_B) in AlFeO_3**

Atom no.	Cation site	Magnetic moment (μ_B)			
		FM		AFM	
		order	disorder	order	disorder
1	Fe1	1.26	3.85	3.59	3.69
2	Fe1	1.26	-3.20	3.59	3.40
3	Fe1	1.26	3.12	3.59	3.71
4	Fe1	1.26	3.77	3.59	3.58
5	Fe2/Al2	0.50	1.27	-3.57	-3.72
6	Fe2	0.50	3.70	-3.57	-3.59
7	Fe2	0.50	3.66	-3.57	-3.58
8	Fe2	0.50	3.81	-3.57	-3.54

(2) On introducing the anti-site disorder between Fe2 and Al2 it was found that, FM ordering in the disordered state is lower in energy than the FM ordering in the chemically ordered state. Secondly, the magnetic moments (Table XI) change significantly only of the Fe ion located at the Al2 site, indicating its low-spin state in the FM ordering and the magnetic moment on each Fe^{3+} ion varies with the site in both the AFM and FM states, and in this sense the system is ferrimagnetic with a rather small effective magnetic moment, as seen experimentally.

(3) Finally, larger exchange energy E_{xc} in the disordered FM state than that in the ordered FM state is responsible for its high-spin state and its greater stability (Fig. 2.24).

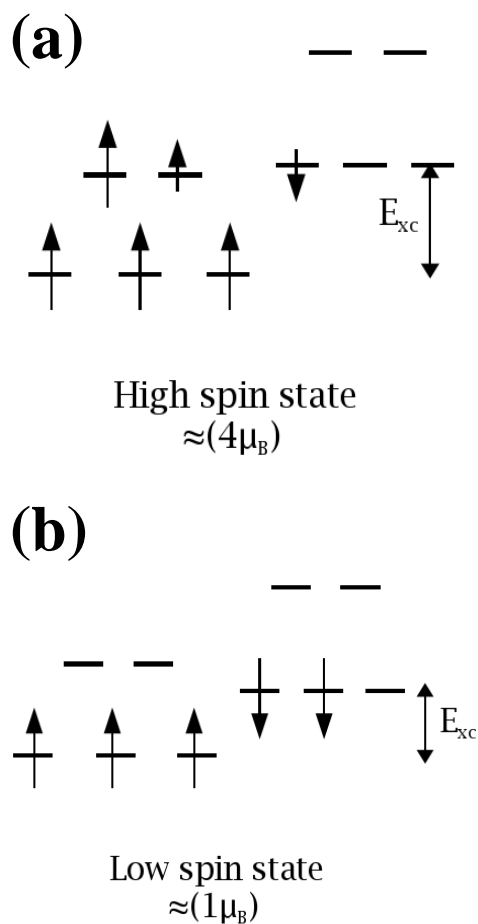
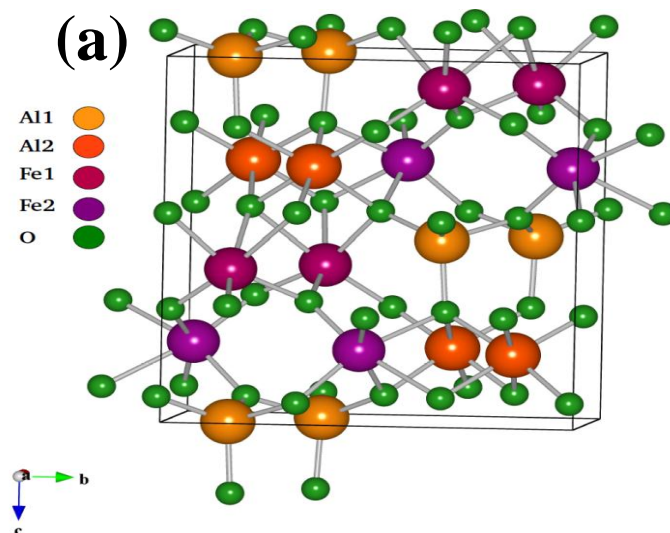


Fig. 2.24: (a) High-spin and (b) low-spin states.

The relation between structure and magnetic ordering as well as anti-site disorder have been examined and it was found that Fe2 site prefers dichotomous (bi-modal distribution) of bond lengths while the Al2 site exhibits uniformity in bond lengths. In the relaxed structures the bond lengths change considerably with the change in magnetic ordering implying a strong spin-phonon coupling in the system. It implies that (a) a high-spin state of Fe^{3+} is energetically favorable (lower) than the low-spin state, and (b) Fe-O

bonds are longer when Fe^{3+} is in the high-spin state, a feature intimately linked with disorder, since the Shannon-Prewitt radius of Fe^{3+} in the low-spin state is close to that of Al^{3+} in octahedral coordination, the FM state in the disordered case is significantly lower in energy because only Fe^{3+} at the Al2-site takes the low-spin state and Fe^{3+} at other sites are in the high-spin state. This results in longer Fe-O bond-lengths in the high-spin configuration, reflected in the Fe-O bonds in the AFM state with Fe^{3+} taking the high-spin state.

The energetics of AlFeO_3 in perovskite and corundum structures (see Fig. 2.25) has been determined. While Fe is found to prefer A site with a high-spin state and G-AFM ordering, the energy of the cubic perovskite structure is almost 3 eV higher than the observed one. Secondly, Fe^{3+} randomly occupying Al sites in the corundum structure takes the low spin state (due to size mismatch), and hence AlFeO_3 in the corundum structure is higher in energy by about 84 meV/formula unit. Thus, the stability of the observed structure is partly due to the distinct sites associated with Al and Fe.



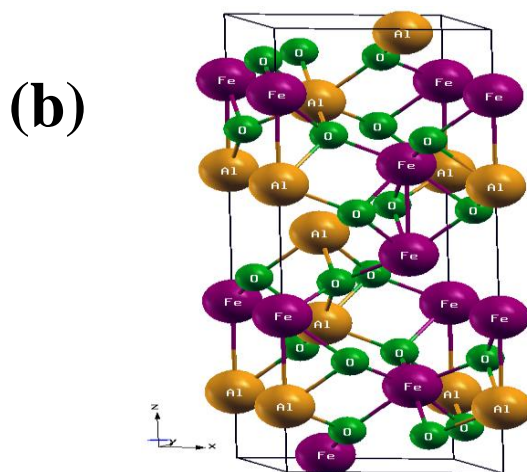


Fig 2.25: Structure of AlFeO_3 in (a) orthorhombic and (b) corundum structures.

Disorder, magnetic ordering and stability of GaFeO_3 have also been examined and found a greater degree of anti-site disorder in GaFeO_3 because the radius of Fe^{3+} in high-spin state ($R=0.62 \text{ \AA}$) is close to that of Ga^{3+} in octahedral coordination in contrast to relatively weaker mismatch in the ionic radii of Fe^{3+} in high-spin state and Al^{3+} . The interesting results are shown below:

(a) AFM state is lower in energy than the FM one in both the ordered and disorderd cases with a slightly larger magnetic moment in the latter.

(b) In the AFM state, magnetic moments at Fe1 and Fe2 sites are not of the same magnitude giving a weak magnetic moment effectively.

(c) The energy difference between the AFM states in the disordered and ordered cases is only 36 meV/formula unit (as opposed to 73 meV/formula unit of AlFeO_3). Thus, anti-site disorder in GaFeO_3 is expected to be more prominent than in AlFeO_3 .

2.4.3 Electrical and Magnetoresistance Properties of AlFeO_3 and GaFeO_3 :

AlFeO_3 and GaFeO_3 show ferroelectric hysteresis at relatively low temperatures (< 300 K) with the hysteresis loops reflecting the leaky nature of these materials. In Fig. 2.26, hysteresis loops of both AlFeO_3 and GaFeO_3 are shown. The maximum (saturation) polarization (P_m), remanant polarization (P_R) and coercive field of AlFeO_3 (GaFeO_3) are $P_m = 0.05(0.07) \mu\text{C}/\text{cm}^2$, $P_R = 0.02(0.04) \mu\text{C}/\text{cm}^2$ and $E_c = 1.22(6.4) \text{ kV}/\text{cm}$ respectively, at 200 K for an applied voltage of 500 V. Clearly, AlFeO_3 and GaFeO_3 are multiferroic as well as ferroelectric.

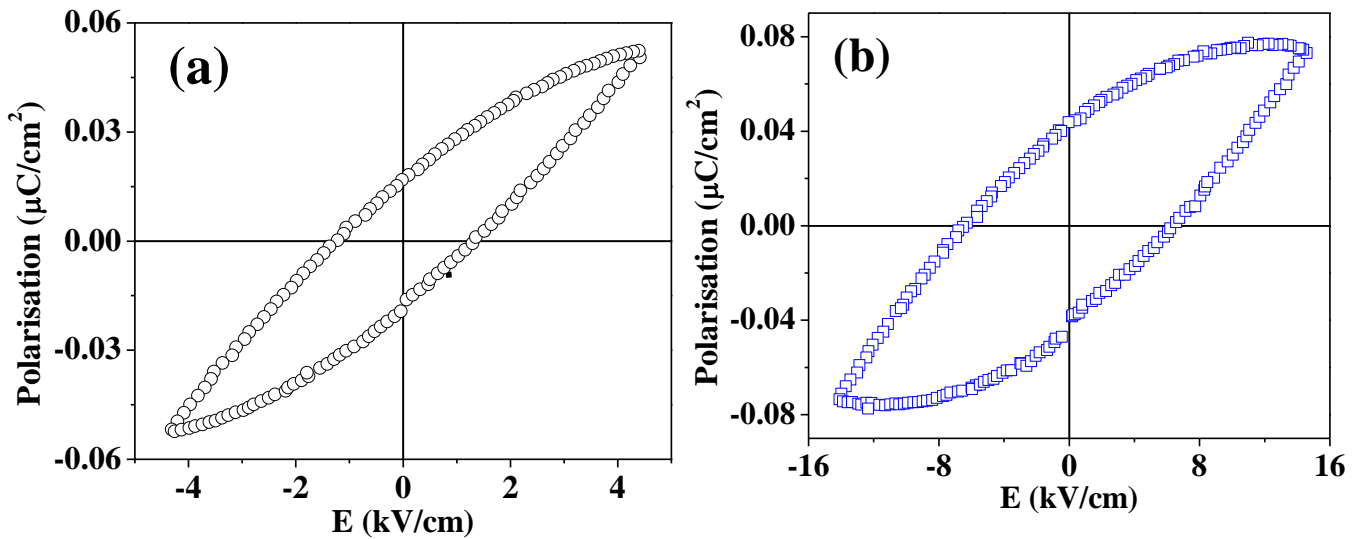


Fig. 2.26: Ferroelectric hysteresis loops of (a) AlFeO_3 and (b) GaFeO_3 at 200 K (1 kHz).

Magnetoresistance properties of both AlFeO_3 and GaFeO_3 were examined. Both the oxides are insulators and show negligible magnetoresistance around 300 K, being 0.5% or less in the case of AlFeO_3 and GaFeO_3 at 2 T and 300 K as shown in Fig. 2.27.

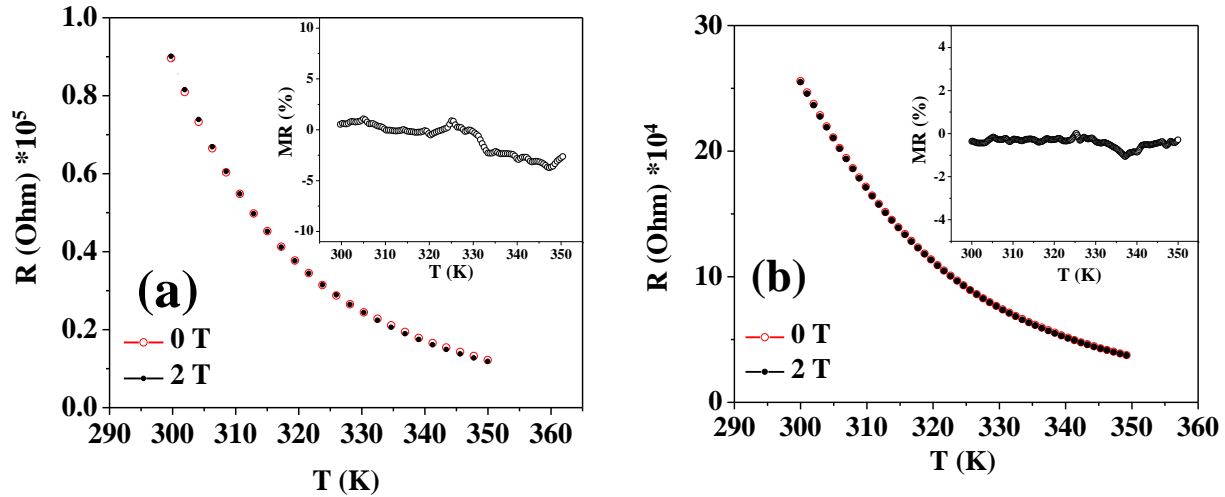
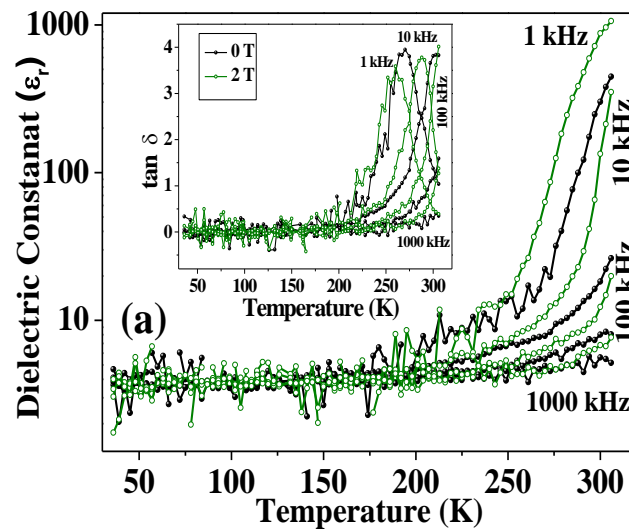


Fig. 2.27: DC resistance vs temperature plots of (a) AlFeO_3 and (b) GaFeO_3 at 0T and 2T. Inset shows the % magnetoresistance of the respective samples.

2.4.4 Dielectric and Magnetodielectric Properties of AlFeO_3 and GaFeO_3 :

Temperature variation of dielectric properties of AlFeO_3 and GaFeO_3 are shown in Figs.2.28 (a) and (b), respectively. Dielectric dispersion below T_N and a significant increase in the dielectric constant above T_N , was observed in both compound. The dielectric behaviour shown in Fig. 2.28 is not unlike that of relaxor ferroelectrics.



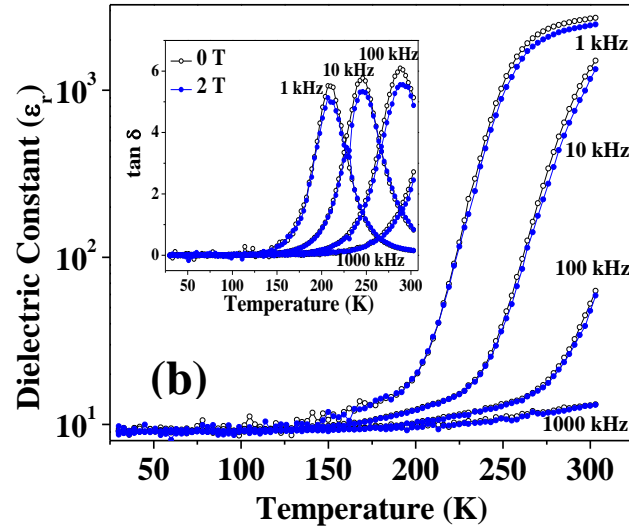


Fig. 2.28: Temperature variation of dielectric properties of (a) AlFeO_3 and (b) GaFeO_3 . Effect of 2 T is also shown for both (a) and (b).

A marked increase in the dielectric constant around T_N signifies interaction between electric and magnetic order parameters. Application of a magnetic field has a marked effect on the dielectric properties of GaFeO_3 , but the effect is considerably smaller in AlFeO_3 . The effect of magnetic field of 2 T on the properties of AlFeO_3 and GaFeO_3 are shown in Fig. 2.28. Magnetocapacitance in AlFeO_3 reaches a value of around 20% at 300 K at 0.5 kHz and 2 T and does not vary significantly with frequency. The effect of magnetic field is however large in the case of GaFeO_3 , which shows large magnetocapacitance and a significant variation of the magnetocapacitance with frequency as shown in Fig. 2.29 (a). Maximum magnetocapacitance is observed in GaFeO_3 around 40 kHz and at this frequency, GaFeO_3 shows 40% magnetocapacitance at 2 T and 20% at 1 T. Such a large magnetocapacitance is indeed noteworthy.

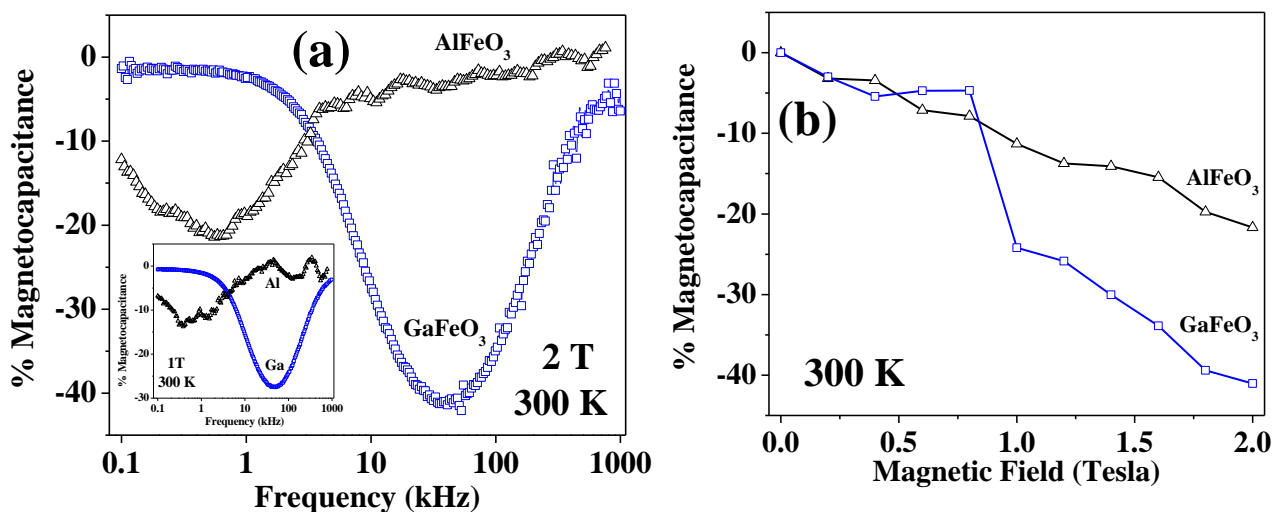


Fig. 2.29(a): Variation of % magnetocapacitance with frequency for AlFeO₃ and GaFeO₃ at a magnetic field of 2 T. In the inset variation of % magnetocapacitance with frequency at 1 T is shown, **(b):** Variation of % Magnetocapacitance with magnetic field for AlFeO₃ (0.5 kHz, 300 K), and GaFeO₃ (40 kHz, 300 K).

In Fig. 2.29 (b), the variations of % magnetocapacitance with magnetic field for both oxides are shown. The marked variation of magnetocapacitance in GaFeO₃ is noteworthy, the value increasing with magnetic field. Also the magnetoresistance properties of both the oxides have been examined. Since the magnetoresistance in these oxides are very low or negligible, it therefore appears that the origin of magnetodielectric effect is not entirely due to magnetoresistance. Spin-phonon coupling is expected to manifest more strongly in the presence of disorder, and hence the corresponding magneto-capacitive effects are expected to be pronounced in GaFeO₃, as found experimentally. This is attributed to greater degree of anti-site disorder present in GaFeO₃ as compared to AlFeO₃. In a solid solution of GaFeO₃ and AlFeO₃, additional disorder associated with low-spin states of Fe³⁺, Al and Ga should give even more spectacular magnetocapacitive effects. Disorder in heterovalent cations is well-known to give diffuse

dielectric response or relaxor properties in ferroelectrics [16]. In FeAO_3 ($A=\text{Al}/\text{Ga}$), while disorder occurs among ions of the same charge (Fe^{3+} and Al^{3+}), their magnetic spins (Fe being magnetic and Al being non-magnetic) which couple with structure, are distinct.

2.4.5 Effect of Cr substitution on the magnetic properties of GaFeO_3 :

GaFeO_3 crystallizes in an orthorhombic crystal structure (space group $Pna2_1$) with four different cation sites labelled Ga1, Ga2 (mostly occupied by gallium) and Fe1, Fe2 (mostly occupied by iron). GaFeO_3 exhibits a ferrimagnetic T_N of 210 K which results from unequal distribution of Fe spins of nearly equal magnitude on the sublattices. GaFeO_3 contains only trivalent metals in the structure like rare earth orthoferrites, making them attractive systems for investigations of isovalent substitutions. For example, in the lanthanum orthoferrites, partial replacement of Fe by Cr leads to a reduction in the Néel temperature from 750K in LaFeO_3 to 280K in LaCrO_3 [17]. Moreover, Cr doping is one of the most adopted strategies to tune the dielectric and piezoelectric properties of ferroelectrics for practical applications. It is well known that Cr is effective in decreasing the ageing effect and the dielectric loss; thus, the effect of doping of Cr^{3+} is that of stabilizing the piezoelectric and dielectric properties [18, 19]. In this work the effect of Cr substitution on magnetic properties of GaFeO_3 have been investigated by synthesizing $\text{GaFe}_{1-x}\text{Cr}_x\text{O}_3$ ($x = 0.05, 0.1$ and 0.2) and $\text{Ga}_{1-x}\text{Cr}_x\text{FeO}_3$ ($x = 0.05$ and 0.1) and examining there magnetic properties. All these oxides were found to crystallize in the orthorhombic structure (space group $Pna2_1$) as parent compound GaFeO_3 as evident from the XRD pattern shown in Figs. 2.30and 2.31.

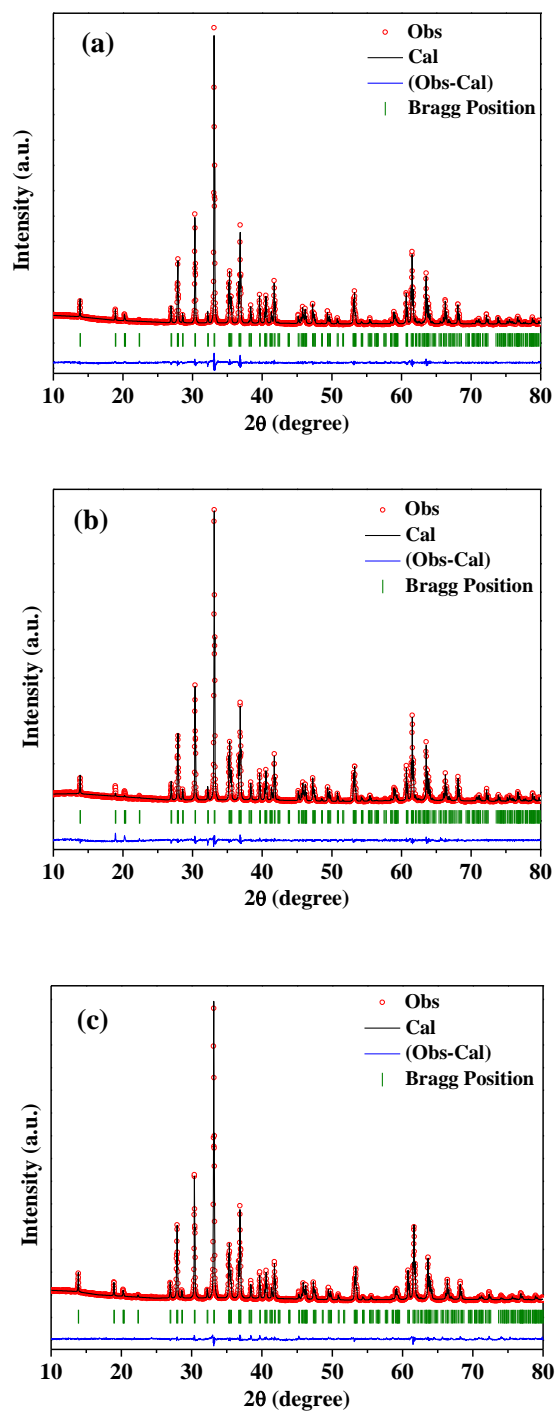


Fig. 2.30: XRD patterns of (a) $\text{GaFe}_{0.95}\text{Cr}_{0.05}\text{O}_3$, (b) $\text{GaFe}_{0.9}\text{Cr}_{0.1}\text{O}_3$ and (c) $\text{GaFe}_{0.8}\text{Cr}_{0.2}\text{O}_3$ along with profile fits, difference patterns and Bragg positions.

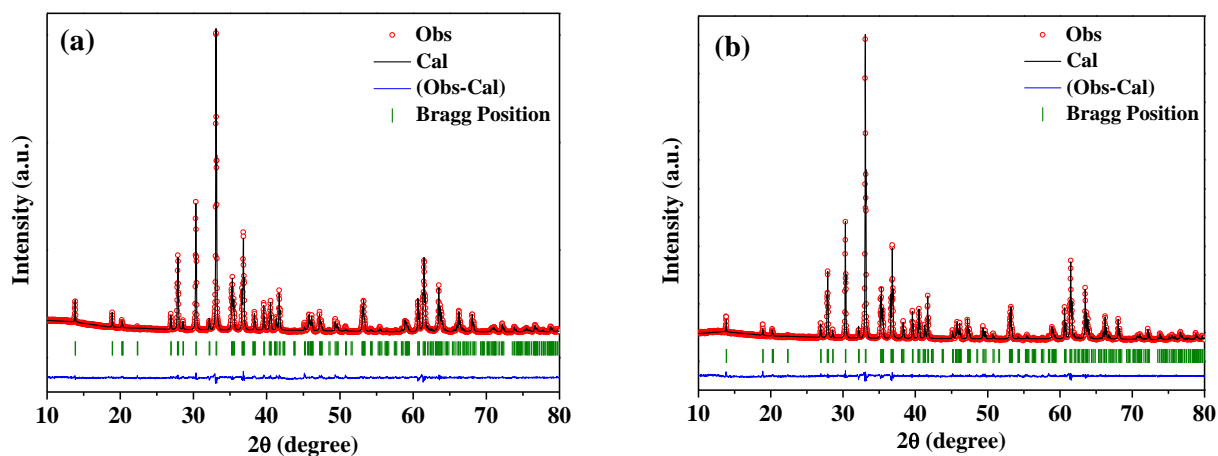


Fig. 2.31: XRD patterns of (a) $\text{Ga}_{0.95}\text{Cr}_{0.05}\text{FeO}_3$ and (b) $\text{Ga}_{0.9}\text{Cr}_{0.1}\text{FeO}_3$ along with profile fits, difference patterns and Bragg positions.

Table XII

Lattice parameters and unit cell volume of $\text{Ga}_{1-x}\text{Cr}_x\text{FeO}_3$ & $\text{GaFe}_{1-x}\text{Cr}_x\text{O}_3$

Compound formula	a (Å)	b (Å)	c (Å)	Unit cell volume (Å ³)
$\text{GaFe}_{0.8}\text{Cr}_{0.2}\text{O}_3$	5.0714(1)	8.7223(1)	9.3641(1)	414.2
$\text{GaFe}_{0.9}\text{Cr}_{0.1}\text{O}_3$	5.0762(1)	8.7307(1)	9.3763(1)	415.5
$\text{GaFe}_{0.95}\text{Cr}_{0.05}\text{O}_3$	5.0776(1)	8.7332(1)	9.3809(1)	415.9
GaFeO_3	5.0814(2)	8.7436(3)	9.3910(3)	417.2
$\text{Ga}_{0.95}\text{Cr}_{0.05}\text{FeO}_3$	5.0787(1)	8.7363(1)	9.3856(1)	416.4
$\text{Ga}_{0.9}\text{Cr}_{0.1}\text{FeO}_3$	5.0795(1)	8.7387(1)	9.3870(1)	416.7

The lattice parameters and unit cell volume has been plotted with the Cr concentration as shown in Figs. 2.32 and 2.33.

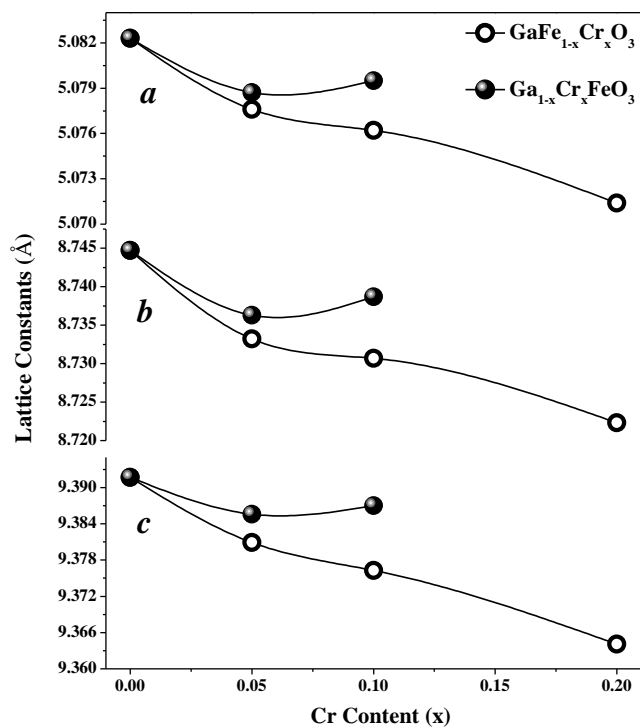


Fig. 2.32: Variation of lattice constants in $\text{GaFe}_{1-x}\text{Cr}_x\text{O}_3$ ($x = 0.05, 0.1$ and 0.2) and $\text{Ga}_{1-x}\text{Cr}_x\text{FeO}_3$ ($x = 0.05$ and 0.1) with Cr content at 300 K obtained from XRD.

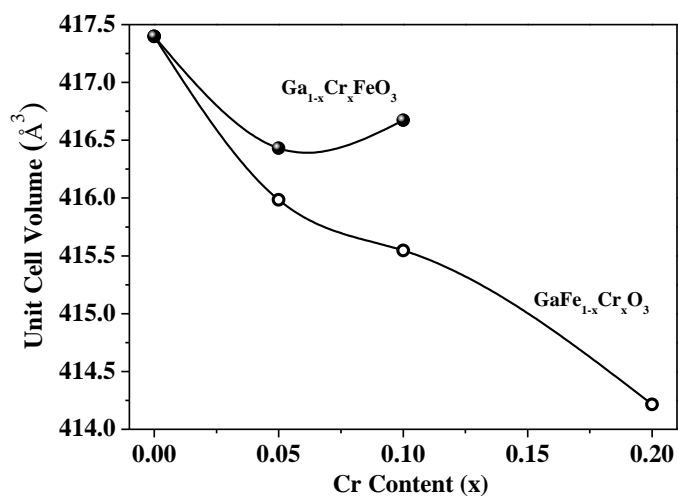
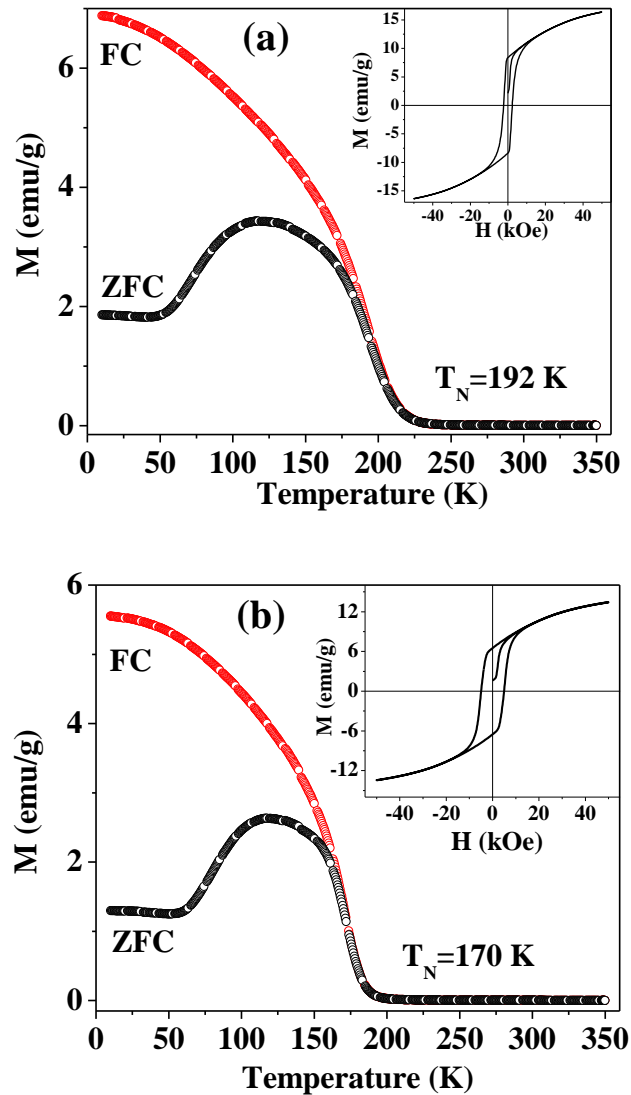


Fig. 2.33: Variation of unit cell volume in $\text{GaFe}_{1-x}\text{Cr}_x\text{O}_3$ ($x = 0.05, 0.1$ and 0.2) and $\text{Ga}_{1-x}\text{Cr}_x\text{FeO}_3$ ($x = 0.05$ and 0.1) with Cr content at 300 K obtained from XRD.

It is observed from Figs. 2.32 and 2.33 that the change in lattice constants is more marked when Cr is substituted in the Fe site of GaFeO_3 . Infact the change in lattice constants and unit cell volume is marginal when Cr is substituted in the Ga site of GaFeO_3 . The magnetic properties of $\text{GaFe}_{1-x}\text{Cr}_x\text{O}_3$ ($x = 0.05, 0.1$ and 0.2) and $\text{Ga}_{1-x}\text{Cr}_x\text{FeO}_3$ ($x = 0.05$ and 0.1) are shown in Figs. 2.34 and 2.35 respectively.

(a) Cr substitution on Fe site of GaFeO_3



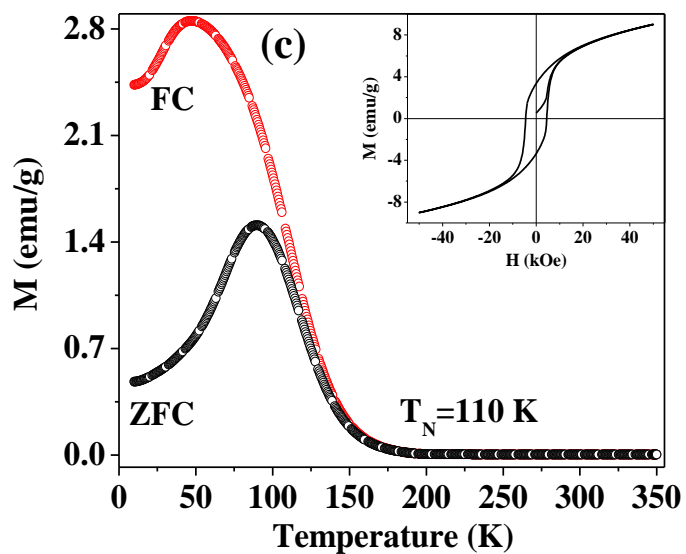
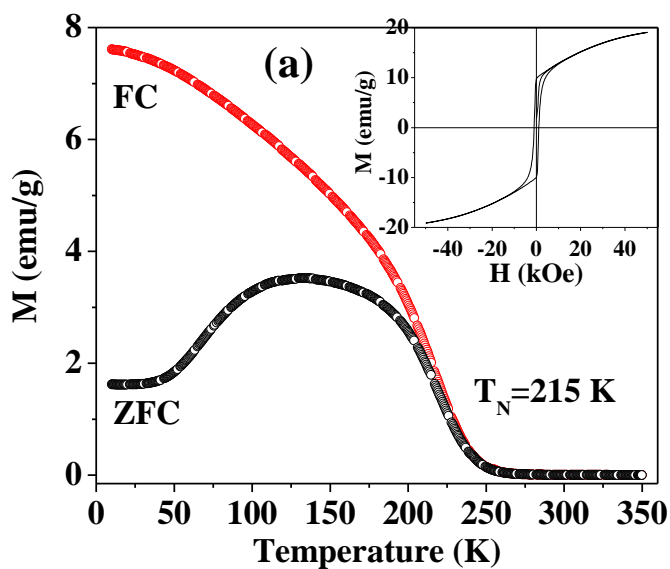


Fig. 2.34: Temperature dependent magnetization of (a) $\text{GaFe}_{0.95}\text{Cr}_{0.05}\text{O}_3$, (b) $\text{GaFe}_{0.9}\text{Cr}_{0.1}\text{O}_3$ and (c) $\text{GaFe}_{0.8}\text{Cr}_{0.2}\text{O}_3$ under field-cooled (FC) and zero-field-cooled (ZFC) conditions. Magnetic hysteresis at 5 K is shown in the inset.

(b) Cr substitution on Ga site of GaFeO_3



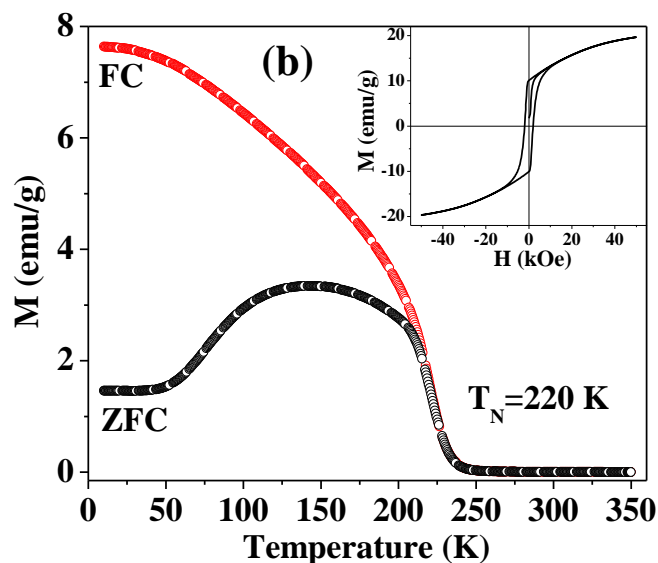


Fig. 2.35: Temperature dependent magnetization of (a) $\text{Ga}_{0.95}\text{Cr}_{0.05}\text{FeO}_3$ and (b) $\text{Ga}_{0.9}\text{Cr}_{0.1}\text{FeO}_3$ under field-cooled (FC) and zero-field-cooled (ZFC) conditions. Magnetic hysteresis at 5 K is shown in the inset.

$\text{GaFe}_{1-x}\text{Cr}_x\text{O}_3$ ($x = 0.05, 0.1$ and 0.2) and $\text{Ga}_{1-x}\text{Cr}_x\text{FeO}_3$ ($x = 0.05$ and 0.1) samples were found to be ferrimagnetic with varying T_N as shown in Figs. 2.34 and 2.35. Magnetic hysteresis was observed at low temperature (see insets of Figs. 2.34 and 2.35). The value of saturation magnetization (M_s), remanant magnetization (M_R), and coercive field (H_C) are given in Table XIII. Divergence between the field-cooled (FC) and zero-field-cooled (ZFC) magnetization data was observed just as in AlFeO_3 or GaFeO_3 . The magnetic transition temperatures (T_N) were calculated from the minimum position of the dM/dT versus temperature curve are around 192 K, 170 K and 110 K for Cr = 5%, 10% and 20% in the Fe site and 215 K, 220 K for Cr = 5%, 10% in the Ga site respectively.

Table XIII

Magnetic data from the hysteresis of $\text{GaFe}_{1-x}\text{Cr}_x\text{O}_3$ and $\text{Ga}_{1-x}\text{Cr}_x\text{FeO}_3$

Compound formula	M_S (emu/g)	M_R (emu/g)	H_C (kOe)	T_N (K)
$\text{GaFe}_{0.8}\text{Cr}_{0.2}\text{O}_3$	9.01	3.4	4.4	110
$\text{GaFe}_{0.9}\text{Cr}_{0.1}\text{O}_3$	13.5	6.5	5	170
$\text{GaFe}_{0.95}\text{Cr}_{0.05}\text{O}_3$	16.4	8.4	2.3	192
GaFeO_3	19.9	10.1	7.7	210
$\text{Ga}_{0.95}\text{Cr}_{0.05}\text{FeO}_3$	19.1	9.8	1.1	215
$\text{Ga}_{0.9}\text{Cr}_{0.1}\text{FeO}_3$	19.7	10	1.9	220

From Table XIII it can be seen that the Néel temperature (T_N) decreases with Cr substitution in the Fe site, while it increases slightly on substitution to the Ga site as compared with the parent compound (GaFeO_3) where the magnetic transition temperature is 210 K. Variation of magnetic transition temperature (T_N) with Cr concentration is shown in Fig. 2.36.

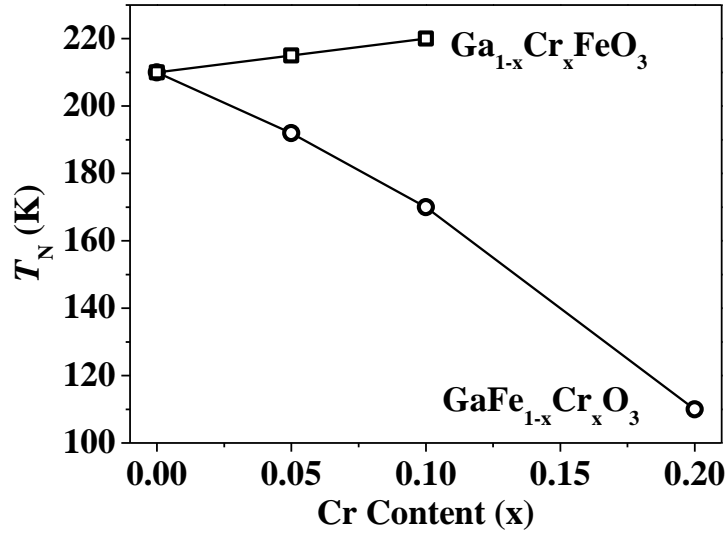


Fig. 2.36: Variation of Néel temperature (T_N) with Cr concentration for $\text{GaFe}_{1-x}\text{Cr}_x\text{O}_3$ ($x = 0.05, 0.1$ and 0.2) and $\text{Ga}_{1-x}\text{Cr}_x\text{FeO}_3$ ($x = 0.05$ and 0.1).

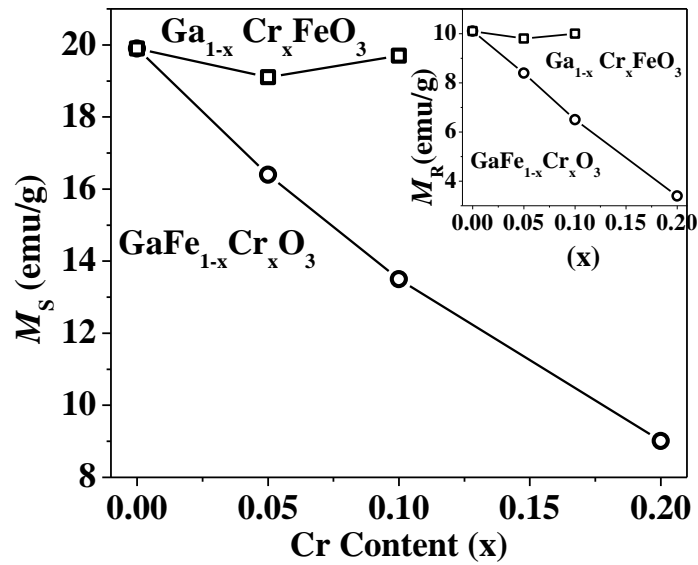


Fig. 2.37: Variation of M_S (in the inset M_R) with Cr concentration for $\text{GaFe}_{1-x}\text{Cr}_x\text{O}_3$ ($x = 0.05, 0.1$ and 0.2) and $\text{Ga}_{1-x}\text{Cr}_x\text{FeO}_3$ ($x = 0.05$ and 0.1).

It is interesting to note that M_S and M_R show decreasing trends with increasing Cr concentration in the Fe site, but there is negligible change in M_S and M_R when Cr is substituted in the Ga site of GaFeO₃ (Fig. 2.37). The marked change in magnetic properties brought about by Cr substitution in the Fe site of GaFeO₃ is clearly related to structural parameters as shown in Figs. 2.32 & 2.33. Also Cr substitution in the Fe site brings about significant change in the unit cell volume. The weak interaction between Cr³⁺ ($3\mu_B$)–O–Cr³⁺ ($3\mu_B$) [20] and Fe³⁺ ($5\mu_B$)–O–Cr³⁺ ($3\mu_B$) [21] as compared with Fe³⁺ ($5\mu_B$)–O–Fe³⁺ ($5\mu_B$) interaction may be related to the lowering of T_N . If the spin of the substituting Cr³⁺ ion aligns with the Fe³⁺ ion, the spin magnetic moment (SMM) of Cr³⁺(d^3) ion is $3\mu_B$; thus, the net SMM is expected to be reduced by $2\mu_B$ per formula unit [22].

2.5 Conclusions:

From X-ray and neutron diffraction studies of the $\text{Al}_{1-x}\text{Ga}_x\text{FeO}_3$ family of oxides, it is observed that they all crystallize in an orthorhombic structure with the space group, $Pna2_1$. The unit cell parameters and volume increase with the Ga content and show a marked increase around the 200 K region. The distortion parameters of the various octahedra do not show significant temperature dependence. The chemical and magnetic unit cells of these oxides are the same and all three oxides are ferrimagnetic. Mössbauer spectroscopy gives useful information on site occupancies and the hyperfine field decreases with increasing Ga content. First-principles calculations show (i) greater anti-site disorder in GaFeO_3 than in AlFeO_3 due to better matching of ionic radii of Fe and Ga, (ii) weak magnetic moment arising from the difference in effective magnetic moments of Fe^{3+} at Fe1, Fe2 and Al2 sites, and (iii) the presence of strong spin-phonon coupling arising from a large difference in ionic radii of Fe^{3+} in high and low spin states (0.645 and 0.55 Å respectively). Both disorder and magnetic properties are intimately related to the local structure that can be explained in terms of ionic sizes.

It is significant that simple iron oxides of the type AFeO_3 ($\text{A}=\text{Al},\text{Ga}$) are both multiferroic and magnetodielectric. The large magnetodielectric effect exhibited by GaFeO_3 demonstrates the importance of the A-site cations. Displacements of the A cations and the disorder associated with their occupancies markedly affect the dielectric and magnetodielectric properties in a significant manner. Introduction of disorder and its intimate coupling to the structure (spin-phonon) may give rise to a characteristic frequency-dependent magnetocapacitive response.

Cr substituted GaFeO_3 shows interesting magnetic properties. It is found that on substitution of Cr in Fe site leads to reduction in magnetic transition temperature (T_N), while T_N value slightly increases when Cr is substituted in the Ga site as compared with parent GaFeO_3 .

REFERENCES:

1. N. A. Hill, *J. Phys. Chem. B*, 2000, **104**, 6694.
2. R. Ramesh, N. A. Spaldin, *Nature Mater.*, 2007, **6**, 21.
3. C. N. R. Rao and C. R. Serrao, *J. Mater. Chem.*, 2007, **17**, 4931.
4. K. Kelm and W. Mader, *Z. Anorg. Allg. Chem.*, 2005, **631**, 2383.
5. F. Bouree, J. L. Baudour, E. Elbadraoui, J. Musso, C. Laurent and A. Rousset, *Acta Cryst.*, 1996, **B52**, 217.
6. L. F. Cotica, S. N. De Medeiros, I. A. Santos, A. Paesano JR., E. J. Kinast, J. B. M. Da Cunha, M. Venet, D. Garcia and J. A. Eiras, *Ferroelectrics*, 2006, **338**, 241.
7. L. F. Cotica, I. A. Santos, M. Venet, D. Garcia, J. A. Eiras and A. A. Coelho, *Solid State Commun.*, 2008, **147**, 123.
8. K. Sharma, V. R. Reddy, D. Kothari, A. Gupta, A. Banerjee and V.G. Sathe, *J. Phys. Condens. Matter.*, 2010, **22**, 146005.
9. R. B. Frankel, N.A. Blum, S. Foner, A. J. Freeman, and M. Schieber, *Phys. Rev. Lett.*, 1965, **15**, 958.
10. M.E. Villafuerte-Castrejón, E. Castillo-Pereyra, J. Tartaj, L. Fuentes, D. Bueno-Baqués, G. González, J.A. Matutes-Aquino, *J. Magn. Magn. Mater.*, 2004, **272**, 837.
11. S. C. Abrahams, J. M. Reddy and J. L. Bernstein, *J. Chem. Phys.*, 1965, **42**, 3957.

12. K.U. Kang, S.B. Kim, S.Y. An, S-W. Cheong and C.S. Kim, *J. Magn. Magn. Mater.*, 2006, **304**, e769.
13. W. Kim, J. H. We, S. J. Kim, and C. S. Kim, *J. Appl. Phys.*, 2007, **101**, 09M515.
14. J. H. We, S. J. Kim, and C. S. Kim, *IEEE. Trans. Mag.*, 2006, **42**, 2876.
15. G. Amthauer, H. Annersten, and S.S. Hafner, *Z. Kristallogr.*, 1976, **143**, 14.
16. V. V. Bhat, A. M. Umarji, V. B. Shenoy and U. V. Waghmare, *Phys. Rev. B.*, 2005, **72**, 14104.
17. M Bakr Mohamed, H Wang and H Fuess, *J. Phys. D: Appl. Phys.*, 2010, **43**, 455409.
18. Li J H and Sun Q C, *Rare Met.*, 2008, **27**, 362.
19. Yang Z P, Zhang R, Yang L L and Chang Y F, *Mater. Res. Bull.*, 2007, **42**, 2156.
20. Fang H C, Yang Z, Ong C K, Li Y and Wang C S, *J. Appl. Phys.*, 1998, **187**, 12.
21. Sung Yong An, Geun Ahn and Chul Sung Kim, *J. Appl. Phys.*, 2000, **87**, 6238.
22. Kwang Joo Kim, Hee Jung Lee, Jung Han Lee, Seungho Lee and Chul Sung Kim, *J. Appl. Phys.*, 2008, **104**, 083912.

Phase transformations of AlFeO_3 and GaFeO_3 induced by ball-milling

Summary

Both AlFeO_3 and GaFeO_3 undergo transformations from the chiral orthorhombic structure ($Pna2_1$) to the other structure when subjected to ball-milling. While GaFeO_3 transforms to a rhombohedral structure ($R\bar{3}c$) similar to that of $\alpha\text{-Fe}_2\text{O}_3$; AlFeO_3 transforms to an orthorhombic structure ($P222$) similar to that of $\delta\text{-Al}_2\text{O}_3$.

3.1 Introduction:

In order to see the effect of particle size on the properties of AlFeO_3 and GaFeO_3 , bulk samples of these oxides were subjected to ball milling at a speed of 400 rpm for 12 h using a planetary monomill (Fritsch Pulverisette-6, Germany). The resulting samples were investigated by employing X-ray diffraction, Raman spectroscopy and magnetic measurements. To our surprise it was found that AlFeO_3 and GaFeO_3 had transformed from the orthorhombic chiral structure ($Pna2_1$) to an orthorhombic ($P222$) structure and a rhombohedral ($R\bar{3}c$) structure respectively. The results of these experiments are summarized below.

3.2 Results and Discussion:

3.2.1 GaFeO_3

X-ray diffraction patterns of bulk GaFeO_3 , ball-milled GaFeO_3 were recorded with a Bruker D8 Advance X-ray diffractometer using $\text{Cu K}\alpha$ radiation ($\lambda = 1.54056 \text{ \AA}$) and those results are shown in Fig. 3.1 along with the XRD pattern of GaFeO_3 nanoparticles prepared by the sol-gel route. The XRD pattern of the nanoparticles prepared by the sol-gel route is the same as that of bulk GaFeO_3 (Figs. 3.1a & b) except for line broadening due to particle size effect.

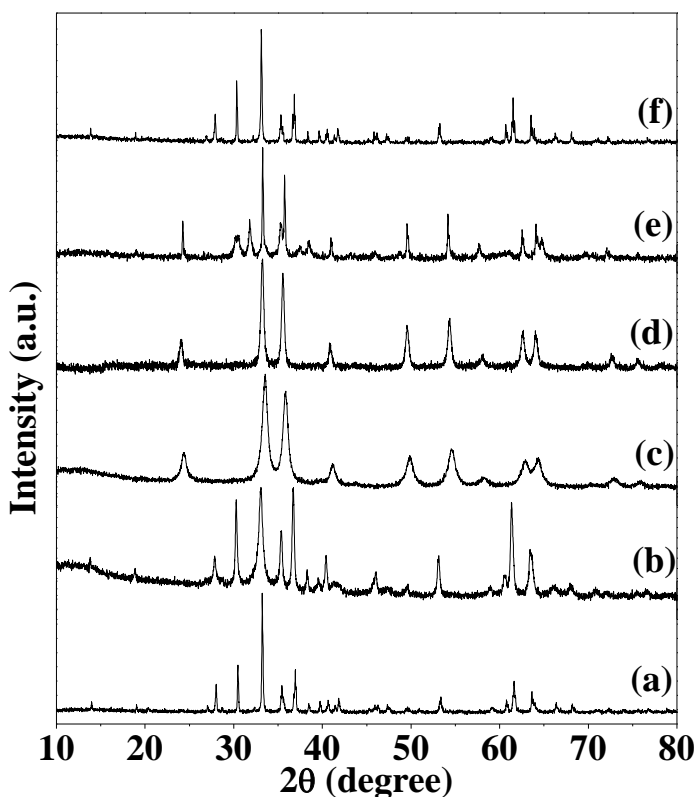


Fig. 3.1: X-ray diffraction pattern of (a) GaFeO_3 bulk sample; (b) GaFeO_3 nanoparticles by sol-gel route; (c) ball-milled GaFeO_3 ; (d) ball-milled GaFeO_3 annealed at 700°C ; (e) mixture of $\text{Fe}_2\text{O}_3 + \text{Ga}_2\text{O}_3$ (1:1) and (f) ball-milled GaFeO_3 annealed at 1000°C .

The observed line broadening was used to calculate the crystallite size of the nanoparticles using the Debye-Scherrer formula and it was found to be 25 nm. The XRD pattern of ball-milled GaFeO₃ (Fig. 3.1c) is quite different from that of the bulk sample (Fig. 3.1a) and it looks similar to the XRD pattern of ball-milled α -Fe₂O₃ which crystallize in the rhombohedral structure ($R\bar{3}c$). Both ball-milled GaFeO₃ and α -Fe₂O₃ shows line broadening and the crystallite size calculated from line broadening were 20 nm and 30 nm respectively. On annealing the ball-milled GaFeO₃ at 700 °C the XRD pattern (Fig. 3.1d) remained same, but with smaller line due to which there is increase in crystallite size of 40 nm. The lattice parameters of ball-milled GaFeO₃ was found to be, $a = 5.022(2)$ Å and $c = 13.606(5)$ Å while the lattice parameters of ball-milled α -Fe₂O₃ and rhombohedral Ga₂O₃ are $a = 5.037(2)$ Å, $c = 13.755(8)$ Å and $a = 4.979$ Å, $c = 13.429$ Å (JCPDS) respectively. Furthermore, the XRD pattern of a 1:1 mixture of Fe₂O₃ and Ga₂O₃ (Fig. 3.1e) is completely different from that of ball-milled GaFeO₃. On heating the ball-milled GaFeO₃ sample to 1000 °C, it transformed back to the orthorhombic chiral ($Pna2_1$) structure as can be seen from Fig. 3.1(f).

In Fig. 3.2, X-ray diffraction pattern of ball-milled GaFeO₃ has been shown along with profile fits and difference patterns. The lattice parameters of ball-milled GaFeO₃ obtained from this profile fit are, $a = 5.022(2)$ Å and $c = 13.606(5)$ Å.

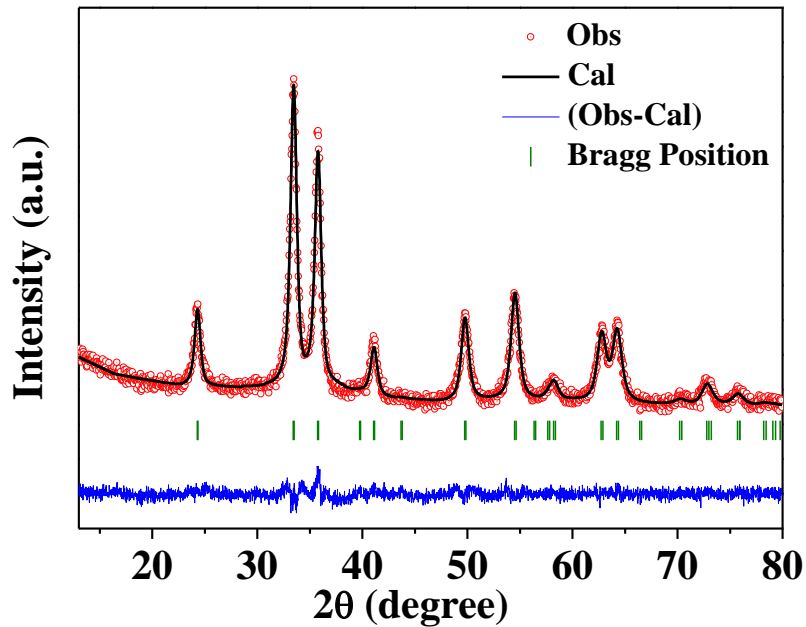


Fig. 3.2: XRD patterns of ball-milled GaFeO₃ along with profile fits, difference patterns and Bragg positions.

Raman spectra of powdered samples were recorded with a LabRAM HR 800 high-resolution Raman spectrometer (HORIBA-Jobin Yvon) using a He-Ne laser ($\lambda = 632.8$ nm). In Fig. 3.3 Raman spectra of ball-milled GaFeO₃ is compared with that of bulk and nanoparticles of GaFeO₃ synthesized by sol-gel route. Although the Raman spectra of bulk GaFeO₃ (Fig. 3.3a) is similar to that of the nanoparticles of GaFeO₃ (Fig. 3.3b), we see distinct differences in the spectra of ball-milled GaFeO₃ (Fig. 3.3c). After annealing the ball-milled GaFeO₃ at 700 °C, the spectra remained the same (Fig. 3.3d) except for sharpening of the bands. Raman spectra of a 1:1 mixture of Fe₂O₃ and Ga₂O₃ (Fig. 3.3e) shows some difference and it is comparable because of

rhombohedral nature of parent α - Fe_2O_3 . The Raman spectra recorded after annealing the sample at 1000 °C (Fig. 3.3f) looks similar to that of bulk GaFeO_3 (Fig. 3.3a).

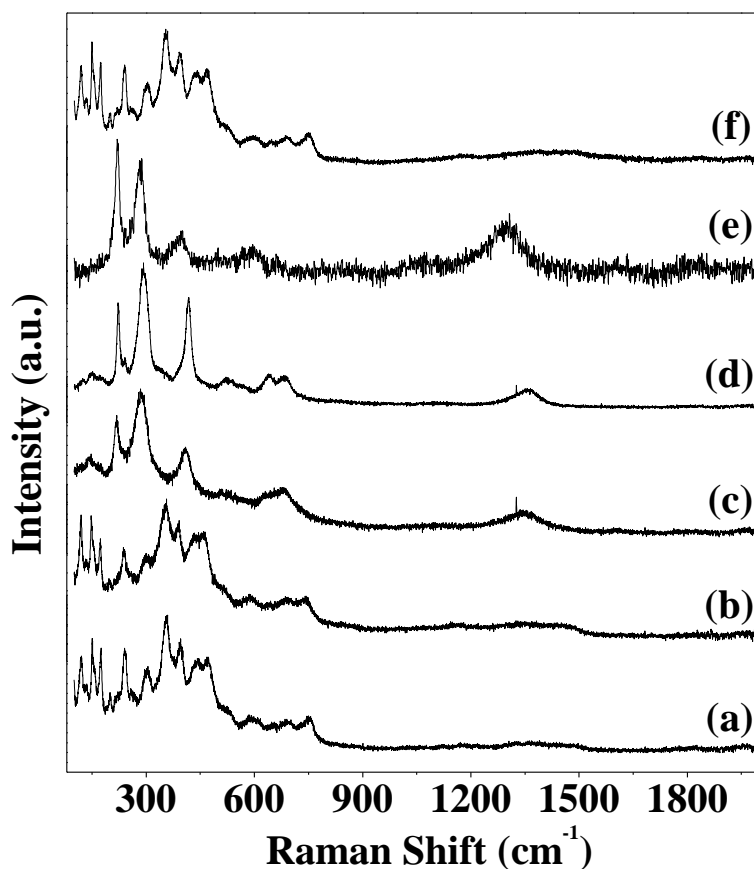


Fig. 3.3: Raman spectra of (a) GaFeO_3 bulk sample; (b) GaFeO_3 nanoparticles by sol-gel route; (c) ball-milled GaFeO_3 ; (d) ball-milled GaFeO_3 annealed at 700 °C; (e) mixture of Fe_2O_3 + Ga_2O_3 (1:1) and (f) ball-milled GaFeO_3 annealed at 1000 °C.

. DC magnetization measurements were carried out using a vibrating sample magnetometer in Physical Property Measurement System (PPMS) under zero-field-cooled (ZFC) and field-cooled (FC) condition in the temperature range of 5 to 390 K under a magnetic field of 100 Oe. Magnetic hysteresis curves were recorded at 5 K and 300 K in magnetic fields going up

to 60 kOe. In Fig. 3.4 (a) we show the temperature dependence of magnetisation of ball-milled GaFeO_3 under FC (field-cooled) and ZFC (zero-field cooled) conditions. The temperature dependent magnetisation data of ball-milled GaFeO_3 annealed at 700°C are shown in Fig. 3.4 (b).

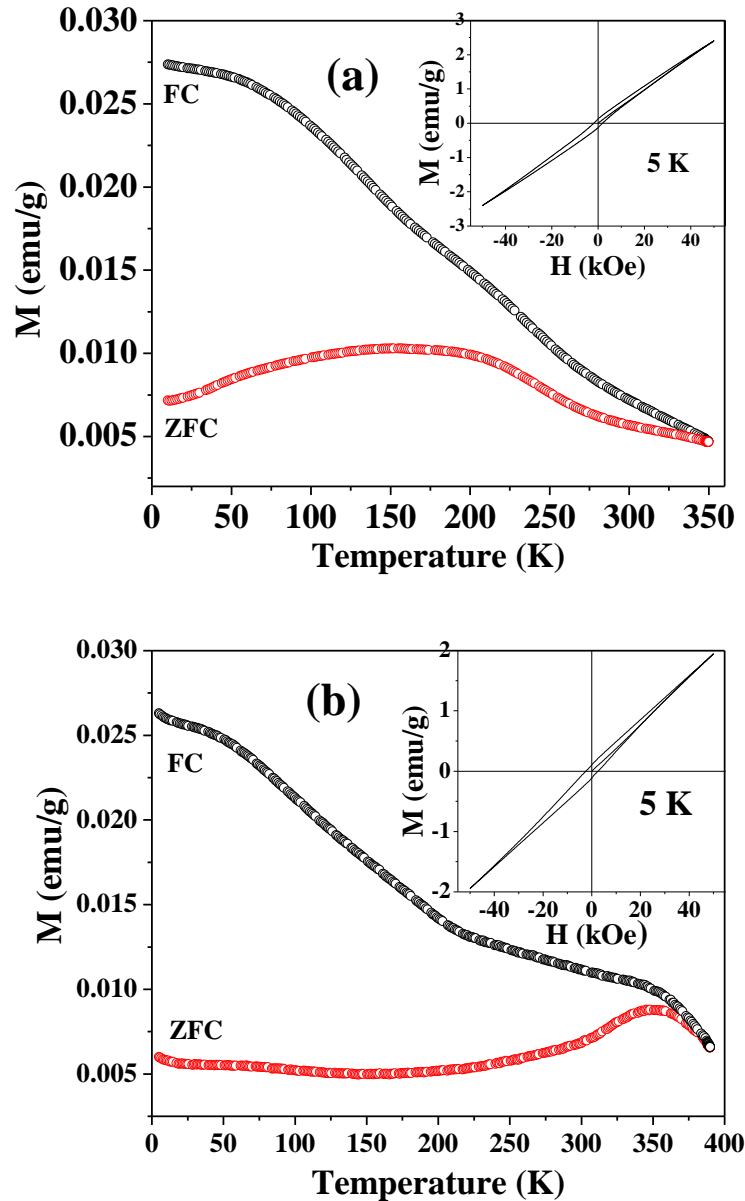


Fig. 3.4: Temperature dependent magnetization of (a) ball-milled GaFeO_3 and (b) ball-milled GaFeO_3 annealed at 700°C under field-cooled (FC) and zero-field-cooled (ZFC) conditions. Magnetic hysteresis at 5 K is shown in the inset.

Fig. 3.4(a) and (b) shows divergence between FC and ZFC data below 350 K. Furthermore, the overall temperature dependent magnetisation curves are quite different from that of bulk GaFeO_3 , which shows sharp ferrimagnetic transition of $T_N = 210$ K. (Details about the magnetic property of bulk GaFeO_3 is given in **Part 2** of the thesis) The ball-milled sample showed some hysteresis at 5 K but no saturation. Ball-milled $\alpha\text{-Fe}_2\text{O}_3$ shows a magnetic behaviour quite different from that of ball-milled GaFeO_3 (Fig. 3.5).

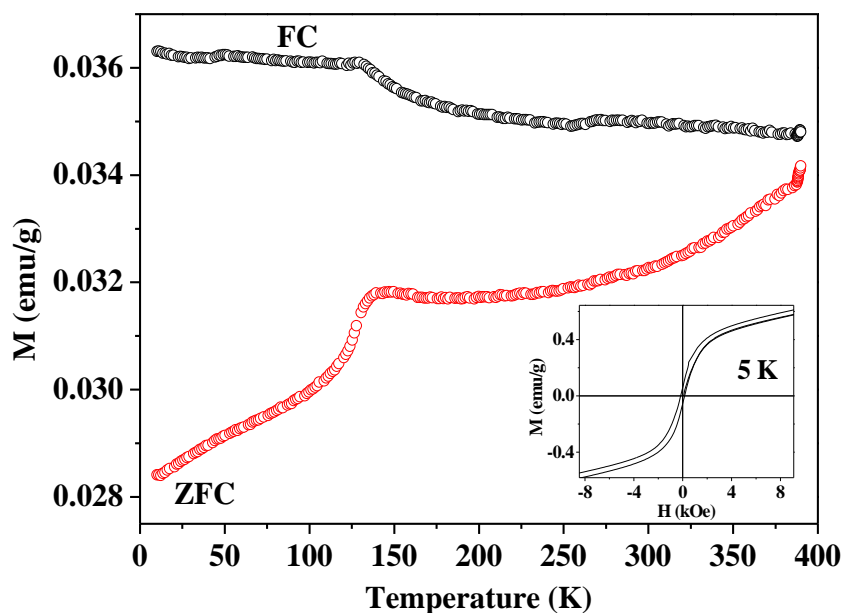


Fig. 3.5: Temperature dependent magnetization of ball-milled $\alpha\text{-Fe}_2\text{O}_3$ under field-cooled (FC) and zero-field-cooled (ZFC) conditions. Magnetic hysteresis at 5 K is shown in the inset.

Nanoparticles of GaFeO₃ made by sol-gel route also showed divergence between FC (field-cooled) and ZFC (zero-field cooled) data and hysteresis was observed at 5 K (see insets of Fig. 3.6). The value of saturation magnetization, remanant magnetization, and coercive field in the case of nanoparticles of GaFeO₃ was observed to be 31 emu/g, 16.6 emu/g and 5.1 kOe respectively. Except coercive field, other two values are significantly larger than that of bulk sample. (In bulk sample, $M_S = 19.9$ emu/g, $M_R = 10.1$ emu/g and $H_C = 7.7$ kOe). Most interestingly, it was found that in nanoparticles magnetic transition temperature (T_N) has been increased to 283 K as compared to the bulk sample which shows a ferrimagnetic T_N of 210 K.

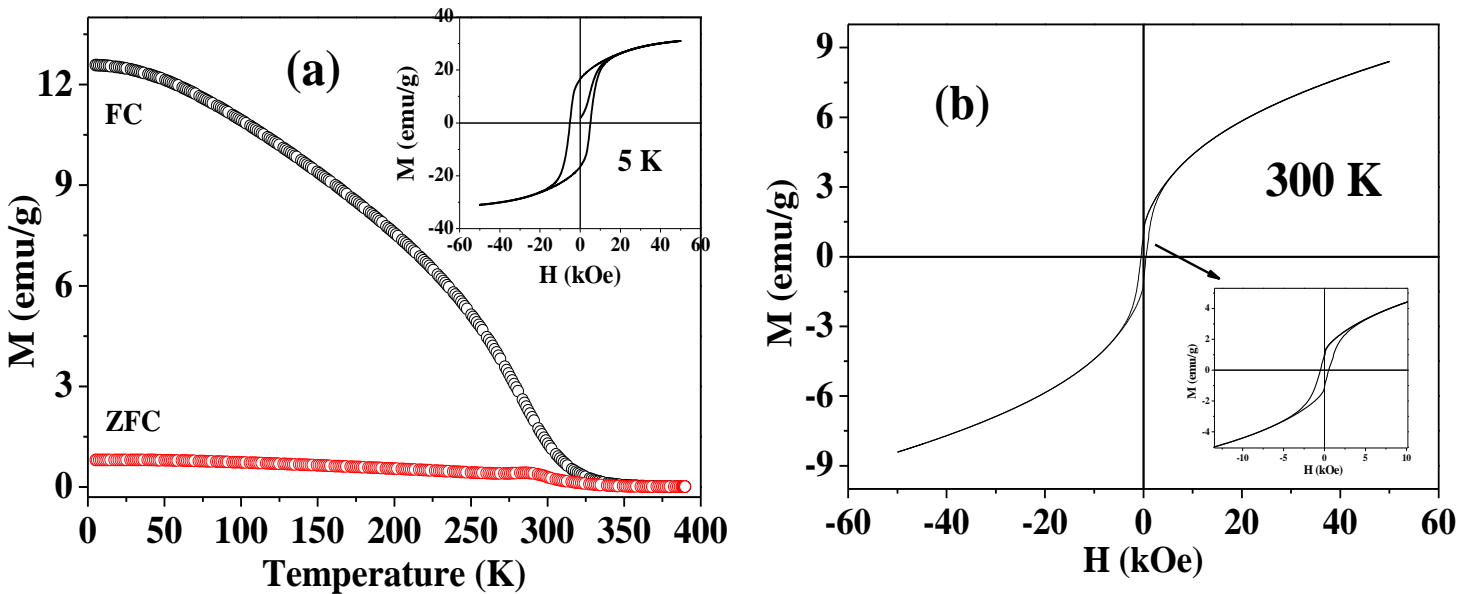


Fig. 3.6: (a) Temperature dependent magnetization of GaFeO₃ nanoparticles by sol-gel route under field cooled (FC) and zero field cooled (ZFC) conditions. Magnetic hysteresis at 5 K is shown in the inset and (b) Magnetic hysteresis of GaFeO₃ nanoparticles by sol-gel route, observed at 300 K.

At room temperature, ferromagnetic hysteresis has been observed in GaFeO₃ nanoparticles made by sol-gel route as shown in Fig. 3.6 (b). From the plot of temperature dependent magnetization curve it is clear that nanoparticles are much more ferromagnetic than bulk material [1, 2]. So this enhanced magnetic property arises from the reduction of particle size.

3.2.2 AlFeO₃

A similar investigation has been carried out on the AlFeO₃ sample prepared by ball-milling of the bulk material. To characterize the structure of ball-milled sample X-ray diffraction patterns of ball-milled AlFeO₃ and bulk sample were recorded with a Bruker D8 Advance X-ray diffractometer using Cu K_α radiation ($\lambda = 1.54056 \text{ \AA}$) and those data were plotted to compare the XRD pattern of ball-milled AlFeO₃ with that of bulk sample (Details of XRD pattern and structure of AlFeO₃ has been discussed in the second part of the thesis) as shown in Fig. 3.7. It was found that XRD pattern of bulk sample is completely different from that of ball-milled AlFeO₃ as shown in Figs. 3.6 (a) and (b) respectively. The ball-milled sample shows line broadening and the crystallite size calculated from line broadening was found to be 20 nm. The XRD pattern, obtained from the diffraction experiment of ball-milled AlFeO₃ does not match with that of ball-milled α -Fe₂O₃. To find out the crystal structure of the ball-milled AlFeO₃ profile fitting was done using a software package Fullprof and the fitted pattern is shown in Fig. 3.8. For this fitting lattice parameters of δ -Al₂O₃ was taken as initials and the data was refined and it was found that the ball-milled sample matches with the XRD pattern of δ -Al₂O₃ which crystallize in orthorhombic structure with *P222* space group.

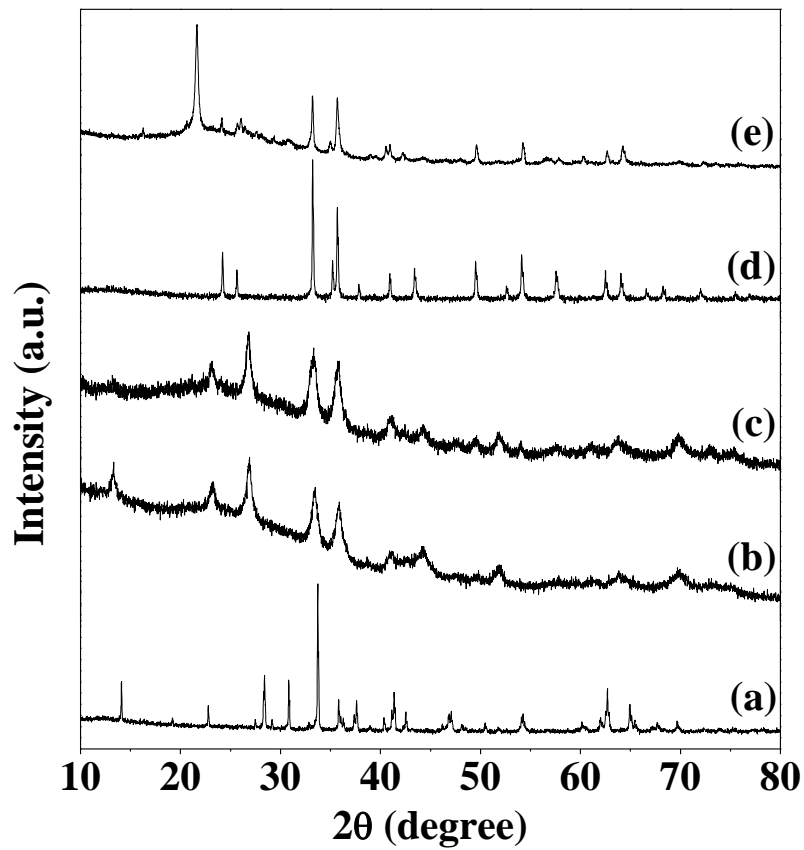


Fig. 3.7: X-ray diffraction pattern of (a) AlFeO₃ bulk sample; (b) ball-milled AlFeO₃; (c) ball-milled AlFeO₃ annealed at 700 °C; (d) mixture of α-Fe₂O₃+α-Al₂O₃ (1:1) and (e) ball-milled AlFeO₃ annealed at 1200 °C.

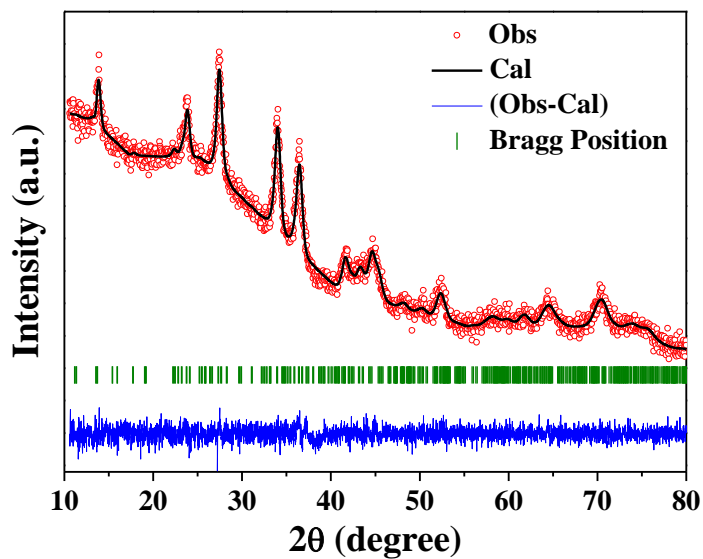


Fig. 3.8: XRD patterns of ball-milled AlFeO₃ along with profile fits, difference patterns and Bragg positions.

Although the XRD pattern of ball-milled AlFeO_3 looks similar to that of $\delta\text{-Al}_2\text{O}_3$ the lattice parameters of the two are different. X-ray diffraction measurements on ball-milled AlFeO_3 carried out by us gave the following lattice parameters $a = 7.798(4) \text{ \AA}$, $b = 7.928(4) \text{ \AA}$ and $c = 11.508(9) \text{ \AA}$, while the lattice parameters for $\delta\text{-Al}_2\text{O}_3$ are $a = 7.934 \text{ \AA}$, $b = 7.956 \text{ \AA}$ and $c = 11.711 \text{ \AA}$ (JCPDS). On annealing the ball-milled sample at $700 \text{ }^\circ\text{C}$ the XRD pattern as shown in Fig. 3.7 (c) remained same and the crystallite size calculated from line broadening was found to be 20 nm . Furthermore, XRD pattern of a 1:1 mixture of $\alpha\text{-Fe}_2\text{O}_3$ and $\alpha\text{-Al}_2\text{O}_3$ (Fig. 3.7d) is completely different from that of ball-milled AlFeO_3 sample. On heating ball-milled AlFeO_3 sample to $1200 \text{ }^\circ\text{C}$ it did not revert to the orthorhombic chiral ($Pna2_1$) structure as found in the case of ball-milled GaFeO_3 (Fig. 3.7e).

Raman spectra were recorded on powdered sample with a LabRAM HR 800 high-resolution Raman spectrometer (HORIBA-Jobin Yvon) using a He-Ne laser ($\lambda = 632.8 \text{ nm}$). In Fig. 3.9. Raman spectra of ball-milled AlFeO_3 has been compared with that of bulk sample. Raman spectra of bulk AlFeO_3 (Fig. 3.9a) is distinctly different from that of ball-milled AlFeO_3 which is shown in Fig. 3.9 (b). After annealing the ball-milled AlFeO_3 at $700 \text{ }^\circ\text{C}$, Raman spectra was recorded (Fig. 3.9c) and it was found to be same as that of ball-milled GaFeO_3 , except sharpening of the bands. Raman spectra of a 1:1 mixture of $\alpha\text{-Fe}_2\text{O}_3$ and $\alpha\text{-Al}_2\text{O}_3$ (Fig. 3.9d) also show some difference. On annealing the sample at $1200 \text{ }^\circ\text{C}$, the Raman spectra (Fig. 3.9e) did not revert to the bulk pattern of AlFeO_3 as it was observed in case of GaFeO_3 .

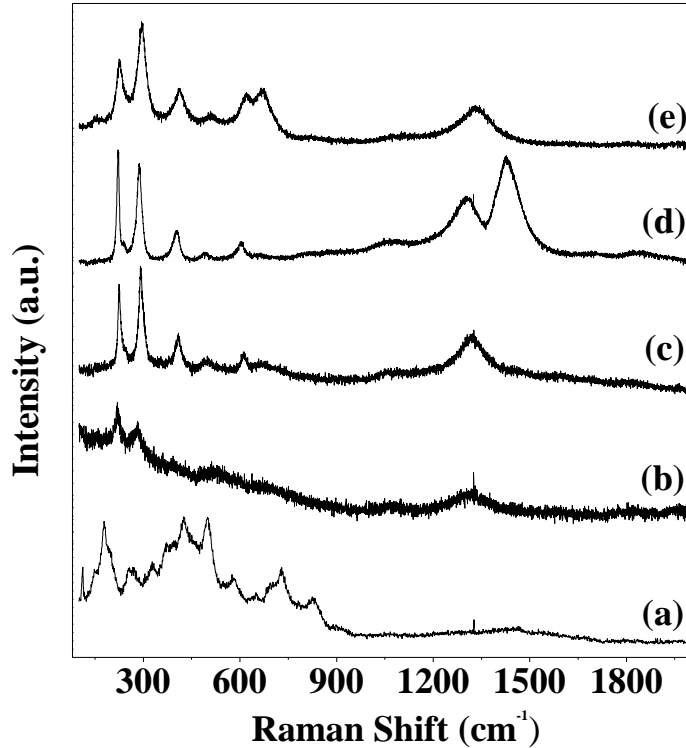


Fig. 3.9: Raman spectra of (a) AlFeO₃ bulk sample; (b) ball-milled AlFeO₃; (c) ball-milled AlFeO₃ annealed at 700 °C; (d) mixture of α-Fe₂O₃ + α-Al₂O₃ (1:1) and (e) ball-milled AlFeO₃ annealed at 1200 °C.

DC magnetization measurements were carried out using a vibrating sample magnetometer in Physical Property Measurement System (PPMS) under zero-field-cooled (ZFC) and field-cooled (FC) condition in the temperature range of 5 to 390 K under a magnetic field of 100 Oe. Magnetic hysteresis curves were recorded at 5 K and 300 K in magnetic fields going up to 60 kOe. Magnetic property of ball-milled AlFeO₃ was compared to that of bulk AlFeO₃ prepared at high temperature and also to that of ball-milled α-Fe₂O₃ (Fig. 3.5). In Fig. 3.10 (a) temperature dependent magnetisation data of FC (field-cooled) and ZFC (zero-field-cooled) for ball-milled AlFeO₃ is shown.

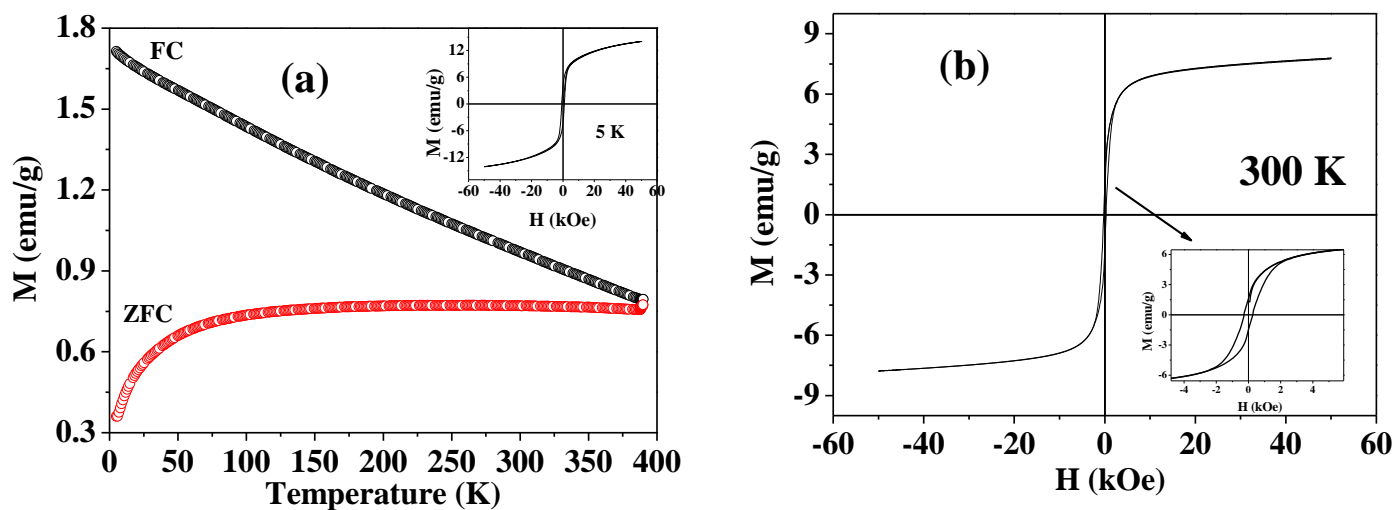


Fig. 3.10: (a) Temperature dependent magnetization of ball-milled AlFeO_3 under field-cooled (FC) and zero-field cooled (ZFC) conditions. Magnetic hysteresis at 5 K is shown in the inset and (b) Magnetic hysteresis of ball-milled AlFeO_3 , observed at 300 K.

Divergence between FC (field-cooled) and ZFC (zero-field-cooled) data was observed in the ball-milled sample. Furthermore, the overall temperature dependent magnetisation curve is quite different from that of bulk AlFeO_3 , which shows sharp ferrimagnetic transition of $T_N = 250$ K. (Details about the magnetic property of bulk AlFeO_3 has been given in **Part 2** of the thesis) The ball-milled sample showed some hysteresis at 5 K as shown in the inset of Fig. 3.10 (a). On the other side ball-milled $\alpha\text{-Fe}_2\text{O}_3$ shows magnetic behaviour quite different from that of ball-milled AlFeO_3 as shown in Fig. 3.5. A magnetic hysteresis (Fig. 3.10b) has been observed at room temperature for this ball-milled sample.

3.3 Conclusions:

Phase transformations of GaFeO₃ and AlFeO₃ are brought about by ball-milling. The transformations are brought about by the pressure and probably the high local temperature during ball-milling.

REFERENCES:

1. A. Sundaresan, R. Bhargavi, N. Rangarajan, U. Siddesh and C. N. R. Rao, *Phys. Rev. B*, 2006, **74**, 161306(R).
2. A. Sundaresan and C. N. R. Rao, *Nano Today*, 2008, **4**, 96.